Topological Design of Lattice Metamaterials with Unusual Mechanical Properties

by Zuyu Li

Thesis submitted in fulfilment of the requirements for
the degree of

Doctor of Philosophy

under the supervision of A/Prof. Zhen Luo and A/Prof. Dongbin Wei

University of Technology Sydney
Faculty of Engineering and Information Technology

September 2023

CERTIFICATE OF ORIGINAL AUTHORSHIP

I, Zuyu Li, declare that this thesis is submitted in fulfilment of the requirements for the award of Doctor of Philosophy in the School of Mechanical and Mechatronic Engineering at the University of Technology Sydney.

This thesis is wholly my own work unless otherwise referenced or acknowledged. In addition, I certify that all information sources and literature used are indicated in the thesis.

This document has not been submitted for qualifications at any other academic institution.

This research is supported by the Australian Government Research Training Program.

Signature: Production Note:
Signature removed prior to publication.

Date: 05 September 2023

Acknowledgements

I am sincerely grateful to all those who gave a ray of sunshine to my life.

First and foremost, I would like to express my sincere gratitude to my principal supervisor, A/Prof. Zhen Luo, for all the opportunities, suggestions, and supports throughout my candidature. His outstanding knowledge and meticulous attitude towards research have a profound influence on me. I would also like to convey my gratitude to my co-supervisor, A/Prof. Dongbin Wei, for his support and guidance.

I would like to thank my colleagues, Dr. Huipeng Xue, Dr. Quantian Luo, Mr. Rowell San Gabriel, and Mr. Hantao Pan, for their supports. I also value the online company of my friend Mr. Yuanmao Li throughout the PhD journey.

Finally, I would like to express my deepest gratitude to my family for their love. This work would not have been possible without their encouragements.

Zuyu Li

Sydney, September 2023

List of Publications

[1] **Z. Li**, W. Gao, N. Kessissoglou, S. Oberst, M.Y. Wang, Z. Luo, Multifunctional mechanical metamaterials with tunable double-negative isotropic properties, Mater. Des. 232 (2023) 112146. https://doi.org/10.1016/j.matdes.2023.112146. (JCR Q1, IF = 8.4)

[2] **Z. Li**, W. Gao, M.Y. Wang, C.H. Wang, Z. Luo, Three-dimensional metamaterials exhibiting extreme isotropy and negative Poisson’s ratio, Int. J. Mech. Sci. 259 (2023) 108617. https://doi.org/10.1016/j.ijmecsci.2023.108617. (JCR Q1, IF = 7.3)

[3] **Z. Li**, W. Gao, M.Y. Wang, Z. Luo, Design of multi-material isotropic auxetic microstructures with zero thermal expansion, Mater. Des. 222 (2022) 111051. https://doi.org/10.1016/j.matdes.2022.111051. (JCR Q1, IF = 8.4)

[4] **Z. Li**, Z. Luo, L.C. Zhang, C.H. Wang, Topological design of pentamode lattice metamaterials using a ground structure method, Mater. Des. 202 (2021) 109523. https://doi.org/10.1016/j.matdes.2021.109523. (JCR Q1, IF = 8.4, Cover paper)

[5] S. Wu, Z. Luo, **Z. Li**, S. Liu, L.C. Zhang, Topological design of pentamode metamaterials with additive manufacturing, Comput. Methods Appl. Mech. Eng. 377 (2021) 113708. https://doi.org/10.1016/j.cma.2021.113708. (JCR Q1, IF = 7.2)

[6] **Z. Li**, H. Xue, Z. Luo, Design of pentamode lattice metamaterials by topology optimization, The 5th Australasian Conference on Computational Mechanics, Sydney, Australia, Dec 2021. (Best paper award)

List of Figures

List of Tables

Abbreviations

SIMP	Solid Isotropic Material with Penalization
BESO	Bidirectional Evolutionary Structural Optimization
2D	Two-dimensional
3D	Three-dimensional
NPR	Negative Poisson's Ratio
ZTE	Zero Thermal Expansion
NTE	Negative Thermal Expansion
CTE	Coefficient of Thermal Expansion
PTE	Positive Thermal Expansion
DOF	Degrees of Freedom
N-I	Nickel-Invar
A-T	Al 6061-Ti6Al4V
C-M	CuCrZr-M300

Abstract

Lattice metamaterials are artificially engineered materials that are composed of periodic cellular microstructures. They possess unusual physical properties that are not commonly observable in nature. Lattice metamaterials with exceptional mechanical properties have a variety of applications in aerospace, mechanical, vehicle, civil, and biomedical engineering. However, the current trial-and-error design method based on the intuition and experience cannot explore their full potential. New systematic design methods and novel metamaterials with unprecedented properties are in great demand.

Therefore, this research focuses on developing new systematic and rational design methods for finding lattice metamaterials with unusual mechanical properties. Novel microstructures that are found by the developed design methods would be studied and introduced in this research.

Firstly, this research developed a discrete topology optimization method for designing pentamode metamaterials with at least elastic orthotropic symmetry. Since a large ratio of bulk modulus to shear modulus is no more a sufficient condition for non-isotropic pentamode metamaterials, a new mathematical optimization formulation for finding such a material is established. Novel isotropic, transverse isotropic, and orthotropic pentamode microstructures have been found by the proposed design method.

Secondly, this research proposed a discrete topology optimization method for designing three-dimensional metamaterials with ideal elastic isotropy and extreme negative

Poisson's ratio, which are a type of unimode metamaterials. Novel three-dimensional strut-based isotropic unimode microstructures have been found, which are also capable of exhibiting tunable negative Poisson's ratios by only altering their volume fractions.

Thirdly, this research developed a multi-material continuum topology optimization method for designing isotropic auxetic metamaterials with zero thermal expansion. The density clustering is used to guarantee that all intermediate designs during the optimization iterations have at least elastic cubic symmetry. A novel composite microstructure is numerically studied through finite element analyses to demonstrate its elastic isotropy, auxeticity, and thermal dimensional stability.

Finally, this research developed a multi-material discrete topology optimization method for designing isotropic lattice metamaterials with tunable thermal expansion and tunable auxeticity. Effective thermoelastic properties of potential designs described by a bi-material ground structure are calculated by using the computational homogenization method with beam elements. Novel strut-based composite microstructures are found and studied. By tailoring either the cross-sectional radii or the constituent material combination of struts, these microstructures can simultaneously exhibit elastic isotropy, tunable thermal expansion, and tunable auxeticity.

Keywords: Topology optimization; Pentamode metamaterials; Auxetic metamaterials; Unimode metamaterials; Thermal expansion; Tunable properties; Elastic isotropy

Table of Contents

Chapter 1 Introduction

1.1. Background

Lattice metamaterials are artificially engineered materials with unusual properties that are not typically observable in nature, which usually consist of periodic arrangements of architected microstructures. They open the door to lightweight, smart, tunable, and multi-functional materials that can realize a variety of unprecedented engineering applications. Advanced additive manufacturing techniques further facilitate developments of lattice metamaterials that usually have complicated microstructural geometries.

Mechanical metamaterials have sparked a rising interest owning to their potential applications in aerospace, vehicle, civil, and biomedical engineering. By tailoring constituent materials and microstructural geometries, diverse lattice metamaterials with superior mechanical properties have been reported in recent years. However, most of these metamaterials are found by the trial-and-error method based on empirical design motifs. Such a conventional design methodology has limited the rapid development of mechanical metamaterials and cannot reach their full potential. Therefore, new design methods, novel microstructures, and unprecedented functionalities of lattice metamaterials are in demand.

Topology optimization is a numerical technique that optimizes the material distributions within a prescribed geometric domain to find structural designs with the best performance under specific constraints. Topology optimization has been broadly adopted in practice as a rational design tool for macroscopic engineering structures. Its further application in designing microstructures of lattice metamaterials with unusual mechanical properties would represent a preferred alternative to conventional trial-and-error design methods and have considerable promise for finding novel mechanical metamaterials.

1.2. Literature review

1.2.1. Metamaterials

Metamaterials are a class of man-made materials with properties that are uncommonly present in naturally occurring materials and go beyond those of their constituents. These artificially engineered materials provide the capability to enlarge the material property space and influence various aspects of our life. Metamaterials have received an increasing attention due to their unprecedented properties, novel functionalities, and superior performance that are attractive for many applications. Their rapid development has been further facilitated by advances in additive manufacturing techniques and computational analysis methods.

Metamaterials initially emerged in the context of electromagnetism as materials capable of manipulating electromagnetic waves. In 1968, Veselago [1] predicted materials featuring negative values of both permittivity and permeability, which are different from conventional materials with both positive values. Such electromagnetic metamaterials were experimentally verified by using periodic arrays of metal rods [2] and split-ring resonators [3]. Since then, the field of metamaterials has grown rapidly and entered various aspects of solid physics, including electromagnetic, acoustic, thermal, and mechanical metamaterials. A few examples are given in Figure 1.1.

Photonic crystals are a kind of electromagnetic metamaterials that can forbid the transmission of light within specific frequency ranges. This concept was first proposed in 1987 by John [4] and Yablonovitch [5]. Photonic crystals are usually composed of periodic arrays of multiple dielectric materials with high contrast dielectric indices. Due to their ability of manipulating electromagnetic waves, photonic crystals have been applied in various optical devices.

Acoustic metamaterials are materials with engineered internal microstructures that can manipulate sound waves in fluids and solids. The first acoustic metamaterial was constructed as localized resonant lead spheres coated with rubber, which possess effective negative elastic constants [6]. Photonic crystals are a class of acoustic metamaterials exhibiting phononic band gaps. Due to their promising capabilities of preventing mechanical waves within certain frequency ranges from propagating, phononic crystals can be used for sound insulation, frequency filters of acoustic waves, and high-resolution acoustic imaging [7].

Thermal metamaterials are man-made materials that can control the flow of heat to make many fascinating thermal phenomena become possible, which were first predicted in 2008 by Fan et al. [8] and Chen et al. [9]. Currently, the notion of thermal metamaterial has been widened to cover metamaterials for manipulating not only conduction but also convection and radiation in heat transfer. They have an increasing number of potential applications such as thermal cloaking [10] and thermal illusion [11].

In this research, we focus on lattice mechanical metamaterials, which are a class of materials with unusual mechanical properties and are composed of periodic architected microstructures. Materials' mechanical properties include elasticity moduli, Poisson's ratio, yield strength, fatigue limit, and fracture toughness, etc., which define the behavior of materials under the action of forces. Taking cues from natural cellular materials like wood and trabecular bone, a variety of lattice mechanical materials have been proposed, fabricated, and utilized for diverse applications. For example, using the octet-truss unit cell [12] as a fundamental building block, Zheng et al. [13] presented a group of ultralight and ultrastiff metamaterials that possess an almost linear correlation between stiffness and density for a variety of constituent materials. Later, Berger et al. [14] proposed a closed-cell foam with theoretical upper limit of isotropic stiffness. Such metamaterials are desirable for designing lightweight structures in aerospace, vehicle, and biomedical engineering. Mechanical metamaterials have also demonstrated great promise for other numerous applications, including soft robotics, wearable electronics, and biomedical devices, etc.

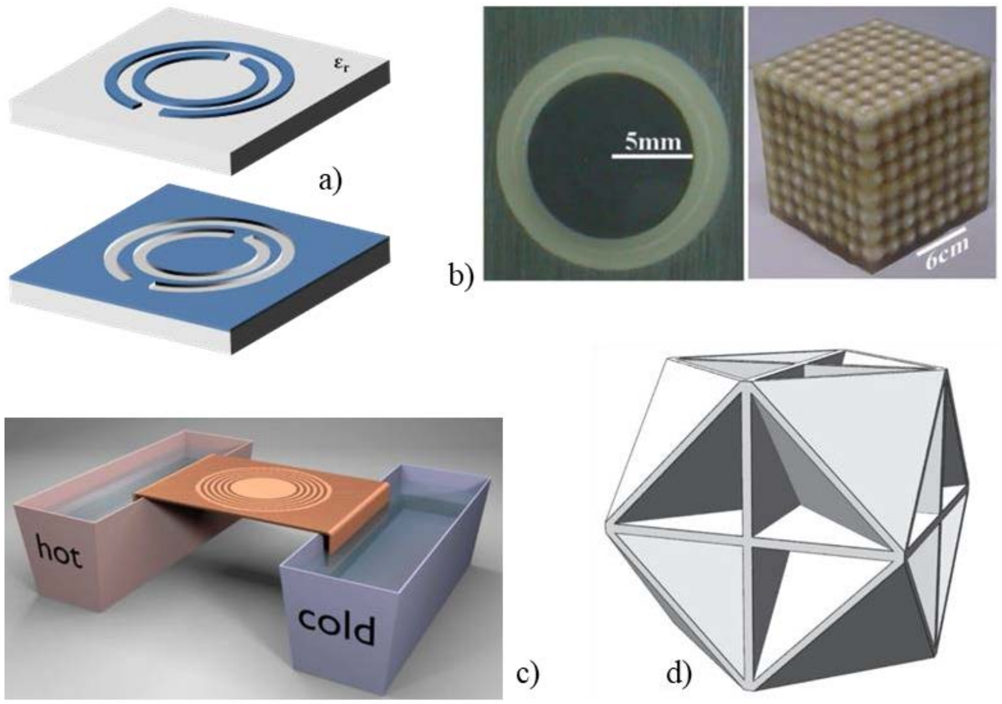

Figure 1.1. Metamaterials: a) Split-ring resonators [15]; b) Localized resonant rubber-coated spheres [6]; c) Thermal cloaking [10]; d) Ultrastiff foam[14]

In recent years, state-of-the-art additive manufacturing techniques have realized the production of mechanical metamaterials with complicated microstructures across different length scales, which facilitate the developments in practical engineering applications of mechanical metamaterials. Hence, there is an increasing interest in finding novel mechanical metamaterials with unique superior properties and new functionalities to broaden their application potentials.

Lattice metamaterials possess flexibility in customizing physical properties by altering their architected microstructures, and the manipulation of constituent distribution within a repeating unit cell is a primary approach to find novel lattice metamaterials. At an early stage, inspiration for mechanical metamaterials often came from biological materials, crystalline structures, and artistic fields such as origami and kirigami, etc. Later, theorists and experimentalists have turned from observers of nature into creative designers of metamaterials [16]. Conventionally, many mechanical metamaterials were found by the trial-and-error method based on their intuition, experience, and parameter studies. However, in specific circumstances, especially when the structure-property relations are vague, such a method is inefficient and may result in a design far away from requirements. Moreover, it is usually difficult for the trial-and-error method to find metamaterials with multifunctional capabilities that simultaneously possess multiple combinations of mechanical, thermal, acoustic, and electromagnetic properties.

In recent years, the materials-by-design paradigm is rapidly evolving from the trial-and-error method, which leads to a variety of rational design methods. It depends on improvements in efficiency and accuracy of numerical methods and advances in linkages of computational design results to fabrication techniques. Rational design methods will make it possible to find lattice metamaterials with mechanical properties that are not only beyond their constituents but also unprecedented or previously considered to be impossible [16]. Such metamaterials will be creatively predicted without using laborious trial-and-error procedures and an excess of experimentation. Therefore, developing systematic and rational methods for materials by design are in high demand. Topology optimization is such a mathematically driven framework that can navigate this challenge by exploring potentials for virtually unlimited structural complexity.

1.2.2. Topology optimization methods

Topology optimization is essentially a numerical process that automatically and iteratively distributes materials within a given geometry domain to find a structural topology with optimized objective performance when subjected to a set of prescribed design constraints. It is therefore an effective design tool for systematically generating innovative structures. For continuum structures, topology optimization methods mainly include density-based methods [17-19], evolutionary methods [20-22], level set methods [23-25], and the feature-mapping methods [26-28], etc. For discrete structures, the most popular topology optimization method is the ground structure method [29, 30]. After developments over thirty-five years, nowadays topology optimization has been successfully accepted as a rational design tool of macroscopic engineering structures, such as aircraft wings [31] and bridge girders [32] in Figure 1.2.

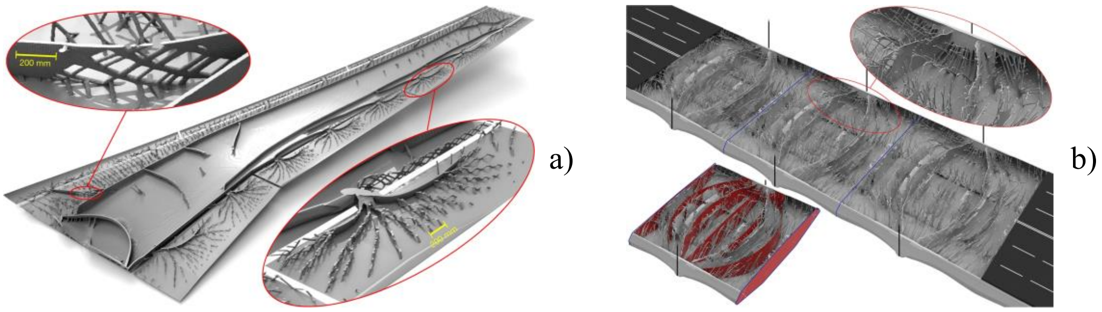

Figure 1.2. Topology optimization design of engineering structures: a) aircraft wing [31]; b) bridge girder [32]

Density-based methods

In 1988, Bendsøe and Kikuchi [33] firstly developed a topology optimization method based on the computational homogenization. It converts the topology optimization problem of a macroscopic continuum into the size optimization problem of microstructures. Later, in 1989, Bendsøe [17] proposed a topology optimization method based on a material interpolation model called SIMP (Solid Isotropic Material with Penalization). In this method, the geometry of design domain is discretized into a fixed finite element mesh, and each element is assigned with an artificial density value. The density value one means that the element is full filled with the solid material, while the density value zero means that the element contains no solid material at all and is filled with an artificial void material. For elements with intermediate density values between zero and one, their material properties are interpolated by those of the solid and void materials. Besides the SIMP model, Stople and Svanberg [34] proposed an alternative material interpolation model in 2001, which is usually used for dynamic problems due to its nonzero gradient for zero density value.

The sensitivity filtering [35] and the density filtering [36] are first introduced into the density-based methods to avoid impractical designs with the checkerboard patterns and reduce mesh dependence of optimized results. Later, projection schemes are adopted to impose constrains on minimum and maximum length scales [37, 38], and these schemes can also eliminate grey transition regions [19, 39]. In recent years, as the most commonly employed topology optimization method, the density-based method has been used in combination of advanced machine learning techniques to discover the next-generation design framework [40-43].

Evolutionary methods

In 1993, Xie and Steven [20] developed the evolutionary structural optimization method based on a heuristic criterion. In this method, elements with low strain energy or low stress would be gradually removed during the optimization iterations. Later, a bidirectional evolutionary structural optimization (BESO) method was proposed by Querin et al. [44], which can readd those deleted elements to the neighborhood of heavily over-stressed elements. To overcome the checkerboard problem that also exists in evolutionary methods, Li et al. [45] proposed a smoothing technique in terms of reference factors of filtered elements. Besides minimization compliance and minimization stress problems, the hard-kill evolutionary methods have also been applied for the thermoelastic [46, 47] and heat conduction [21, 48] problems. One advantage of such hard-kill evolutionary methods is the simplicity to be implemented with commercial finite element analysis software. In 2009, Huang and Xie [22] proposed a new soft-kill BESO method that also utilizes the material interpolation model with penalization.

Level set methods

In 2003, Wang et al. [23] used the shape derivatives to the objective function as evolution velocities of the level set function to design structures with minimum mean compliance. Allaire [24] also proposed a level set-based topology optimization method based on the Hamilton-Jacobi equation. In such type of methods, contour lines or surfaces with zero level set functional value implicitly represent structural interfaces, and then the evolution of level set function under given velocities based on the Hamilton-Jacobi equation can realize changes of structural interfaces and topologies.

Later, the concept of topological derivative is incorporated into level set methods to allow creating new holes inside regions filled with solid materials [49, 50]. However, evolutions based on the Hamilton-Jacobi equation are subject to the Courant–Friedrichs–Lewy condition that usually brings slow convergency speed and more optimization iterations. Moreover, it is challenging to combine multiple design constraints with numerical solutions of the Hamilton-Jacobi equation. Therefore, Wang et al. [51] converted the Hamilton-Jacobi equation into a set of ordinary equations by using the radial basis function to parameterize the level set function for topology optimization. Later, Luo et al. [25] proposed a parametric level set-based topology optimization method using the compactly supported radial basis function. This method supports using the optimality criteria method or mathematical programming methods to update design variables.

In 2010, Takezawa et al. [52] developed a phase field method for shape and topology optimization, which relies on a reaction-diffusion equation with double-well potential function. Inspired by this method, Yamada et al. [53] proposed a level set-based topology optimization method using the reaction-diffusion equation. In this method, an artificial interface energy is adopted as the diffusion term in the evolution equation to avoid reinitialization of signed distance function that is usually required for conventional level set methods based on the Hamilton-Jacobi equation. Moreover, topological derivatives function as the reaction term to drive the evolution of level set function to avoid many numerical problems induced by the conventional convective term.

Feature-mapping methods

A new category of topology optimization methods was identified by Wein et al. [54] as feature-mapping methods, of which the major features are parameterizing the structural design by a high-level geometric description and then mapping it onto a fixed mesh.

In 2014, Guo et al. [26] proposed a topology optimization framework based on moving morphable components. In this method, structural topologies are described by combinations of solid components that can move and morph during optimization iterations. A solid component is described by a level set function, or the so-called topological description function, which can be calculated explicitly using a superellipse equation for two-dimensional (2D) problems. For such a superellipse-type component, design variables include the component's central coordinates, length, thickness, and inclined angle's sine. Later, this method is modified by using components with variable thickness to improve its topology description ability [55] and then extended for three-dimensional (3D) problems by using superellipsoid-type components as design primitives [56].

In 2015, Norato et al. [27] proposed a topology optimization method that projects geometries of solid components into density fields. In this method, the 2D solid component is a rectangular bar with two semicircular ends, of which design variables include the coordinates of two ends and the out-of-plane thickness. Zhang et al. [57] extended this geometry projection method to use plates with uniform thicknesses as solid components for 3D problems. Later, Norato [58] proposed a general geometry projection method that uses supershapes as solid components with higher topology description ability. Supershapes are a generalization of superellipses and can be parameterized by a single equation [59]. In this geometry projection method, the geometries of supershapes are differentially mapped into continuous density fields.

In 2016, Zhou et al. [28] proposed a feature-driven topology optimization method that uses geometrical parameters of engineering features as design variables. The engineering features are described by explicit level set functions, and the Kreisselmeier-Steinhauser function is used for Boolean operations of components. Later, Zhang et al. [60] proposed a more general feature-driven topology optimization method simultaneously using solid features and void features. Recently, Zhou et al. [61] proposed a topology optimization method using worm-inspired geometric features. In this method, B-splines with outward and inward offsets of variable thickness are used to model 2D complex structural topologies.

Ground structure methods

Different from the above continuum topology optimization methods, the ground structure method [29] is a discrete topology optimization method for designing truss and frame structures. In this method, the geometry of design domain is discretized into a mesh using truss or beam elements, which is called the ground structure. Then, the topology optimization problem is usually tackled as a sizing optimization problem for this intricately interlinked ground structure. During optimization iterations, a part of elements become thicker, while other elements become slenderer and may even disappear. Finally, a variety of structures can be described by using the same ground structure. It is obvious that the generation of appropriate ground structures is very essential for this discrete topology optimization method.

A full-level ground structure means that all nodes inside the design domain are linked to each other, which has the highest topology description ability. However, it also leads to a dense total structural stiffness matrix, a high computational cost, and a large number of design variable. In 2014, Zegard and Paulino [30] provided a computational implementation of generating the ground structure with different connectivity levels for irregular regions, and later they extended it into the 3D case [62].

1.2.3. Topology optimization design of metamaterials

Topology optimization has been utilized as an efficient method for circumventing the trial-and-error approach and expediting the process of designing microstructures of metamaterials to achieve desired properties. Sigmund first proposed that inverse problems of finding materials with prescribed elastic properties can be formulated as topology optimization problems [63, 64]. Since then, topology optimization design of metamaterials has attracted an increasing interest in various physics fields [65, 66].

Electromagnetic metamaterials

Topology optimization was first employed for the design of photonic band-gap materials by Cox and Dobson [67], which maximized band gaps between two specific nearby bands of 2D photonic crystals. The level set method [68, 69], the BESO method [70, 71], and the phase field method [72] were also adopted to solve this design problem. These optimized photonic crystals are composed of two high-contrast dielectric materials. Sigmund and Hougaard [73] extended the density-based topology optimization method to design multi-material porous photonic crystals with voids filled with air, and they obtained optimized designs with simple geometric schemes. Besides the gradient-based methods, a derivative-free topology optimization method was proposed to design 2D photonic crystals for different electromagnetic wave polarization modes [74]. Few 3D photonic crystals were designed by topology optimization, although they hold greater practical potential than 2D designs owing to their ability of manipulating electromagnetic waves in all directions [66]. Men et al. [75] proposed a robust topology optimization method for finding 3D photonic crystals with optimal omnidirectional band gaps for different symmetry groups, while Meng et al. [76] only considers an asymmetric simple cubic case. Swartz et al. [77] developed a topology optimization method that uses nested mesh refinement for designing 3D photonic crystals with complete band gaps.

Besides photonic crystals, topology optimization has been employed for designing other types of electromagnetic metamaterials. For instance, Diaz and Sigmund [78] proposed a density-based topology optimization method to design metamaterials with negative magnetic permeability, which is based on distributing a copper film that is attached to a dielectric plate. Later, the level set methods were also used to design such type of metamaterials [79, 80]. Topology optimization methods can also discover electromagnetic metamaterials with both negative permittivity and permeability [81, 82], or both maximal permittivity and permeability [83, 84].

In recent years, advanced analysis methods facilitate topology optimization of electromagnetic metamaterials. For example, Nishi et al. [85] employed the isogeometric analysis for the high-frequency homogenization method to design electromagnetic metamaterials with hyperbolic and bidirectional dispersion properties. Murai et al. [86] incorporated a high-contrast homogenization method into the level set-based topology optimization for designing electromagnetic metamaterials, which can express electromagnetic wave propagation at various frequencies and capture atypical phenomena induced by local resonances.

Acoustic metamaterials

Since the applications of phononic crystals highly depend on their band gap widths, topology optimization methods can be utilized to engineer phononic crystals' band gaps as broad as possible. Sigmund and Jensen [87] first developed a topology optimization method to design 2D phononic crystals with the maximized relative band-gap size respectively for in-plane and out-of-plane waves, where volume constraints are not necessary for this optimization problem. Later, the density-based topology optimization method was extended to maximize the band gap size for bending waves in a plate composed of periodic unit cells [88]. The BESO method has also been applied to create phononic crystals to achieve maximized band gap size [89] and maximized spatial decay of evanescent waves at various frequencies [90]. Topology optimization methods using the genetic algorithm have been commonly used for maximizing phononic crystals' band gap size, respectively considering the constraint on the average density [91], the simultaneous minimization of the mass [92], the tunability of band gaps [93], and the reducing symmetry [94, 95]. Dong et al. [96] employed the multi-objective genetic algorithm into topology optimization to simultaneously maximize the complete photonic and phononic band gaps of 2D phoxonic crystals. Luo and Li [97] adopted a sequential Kriging-based algorithm into the gradient-free topology optimization for finding phononic crystals with tunability of band gaps.

While most of optimized phononic crystals are 2D, a few 3D designs have been reported. Lu et al. [98] first used a density-based topology optimization method for designing 3D phononic crystals that exhibit all-angle and all-mode band gaps. Later, Li et al. [99] combined the fixed-grid finite element method and the BESO method to obtain optimized designs of 3D phononic crystals with smooth boundaries. Recently, Gao et al. [100] proposed a generalized plane wave expansion method to calculate band structures, which provides high computational efficiency for topology optimization of 3D phononic crystals.

Besides phononic crystals, multiple other kinds of acoustic metamaterials have been designed by topology optimization methods. For example, the level set-based methods have been utilized to find acoustic metamaterials respectively exhibiting negative bulk modulus [101], negative mass density [102], high acoustic attenuation [103], and hyperbolic dispersion [104]. Dong et al. [105] proposed a topology optimization method using the genetic algorithm for the design of anisotropic metamaterials simultaneously exhibiting negative mass density, negative elastic modulus, and hyperbolic dispersions.

Thermal metamaterials

Applications of topology optimization on thermal metamaterials mainly focus on maximizing thermal conductivities of composites. Torquato et al. first developed a topology optimization method for maximizing the concurrent conduction of heat and electricity in 3D two-phase composites, and they obtained optimized designs with material interfaces that are like the Schwartz P and D minimal surfaces [106, 107]. Zhou et al. [108] proposed a Matlab code about a modified BESO method for designing two-phase microstructures with desirable transport performance in diverse physical contexts, which can provide optimized designs like the well-known Vigdergauz structures and Kagome lattices. Three-phase microstructures with isotropic maximized thermal conductivities were also designed by topology optimization methods [109, 110], and 2D optimized designs are different from conventional Vigdergauz structures [111].

Torquato and Donev [112] further revealed that the 3D optimized designs in [113] are also extremal for a combination of the bulk modulus and the conductivity. Kruijf et al. [114] further developed a multi-objective topology optimization method to design 2D composites with tailored bulk modulus and thermal conductivity. However, these 2D and 3D composites are not elastically isotropic. Challis et al. [115] proposed that the 3D elastically isotropic optimized designs are different from the minimal surfaces.

Mechanical Metamaterials

As mentioned before, mechanical metamaterials with exceptional elastic properties are the first type of metamaterials utilizing topology optimization as a rational design tool in the 1990s [64, 65]. Among a variety of mechanical properties, the maximization of bulk modulus or shear modulus is a very common target that has been studied by using the density-based method [116, 117], the level set method [118], the BESO method [119, 120], and the data-driven method using the topology optimization to generate datasets [121]. Besides, Guest and Prévost [122] and Wang et al. [123] studied multifunctional materials with a balance between high bulk modulus and high fluid permeability. Topology optimization methods have been also successfully applied for designing other types of lattice metamaterials with unusual mechanical properties, including non-positive compressibility in specific directions [124], perfect conversion of elastic wave modes [125], coupling effects between torsion and tension/compression [126], and multi-platform energy-absorbing stress-strain curves [127], etc.

1.3. Knowledge gaps

Although topology optimization has been successfully applied as an effective design tool of lattice metamaterials, achieving a broader variety of unusual mechanical properties within one microstructure via integrated design is still in great demand. Several knowledge gaps in topology optimization of mechanical metamaterials are identified as follows:

1) There is a lack of effective and efficient discrete topology optimization methods for designing 3D strut-based metamaterials. Conventional continuum-based topology optimization methods are not computationally efficient enough for finding ultra-light microstructures.

2) Most of recent studies about pentamode metamaterials are still based on a microstructure that was proposed over two decades ago. A rational design method that can systematically find novel pentamode microstructures over a wide scope of effective properties is still missing.

3) 3D isotropic unimode metamaterials that are constructed by single-scale and single-phase continua without any mechanism component have not yet been reported in literatures. A rational design method for the discovery of such mechanical metamaterials is in great demand.

4) Although auxetic metamaterials with zero thermal expansion (ZTE) have been successfully designed by topology optimization methods, they are not elastically isotropic. There is a strong need for a systematic design method to find 3D isotropic auxetic metamaterials with thermal dimensional stability.

5) 3D isotropic metamaterials with simultaneous tunabilities of negative Poisson’s ratio and negative thermal expansion are still missing However, microstructures designed by continuum topology optimization methods are usually difficult to automatically convert into parametric geometries and therefore lack direct tunabilities of effective properties. A rational and generic design method based on multi-material discrete topology optimization is highly desired for the discovery of such multifunctional and tunable metamaterials

Filling these knowledge gaps can not only provide multiple new rational design tools customized for lightweight microstructures, but also generate a series of novel metamaterials with potentials to realize unprecedented engineering applications.

1.4. Research contributions

The key contributions of this research can be categorized into four groups and briefly summarized as follows:

1) A discrete topology optimization method is developed by using a 3D ground structure with the geometric orthogonal symmetry. Then a mathematical optimization formulation is established for finding pentamode metamaterials with at least orthotropic symmetry. Novel pentamode microstructures have been found and studied.

2) A discrete topology optimization method is developed by using a 3D ground structure with the geometric cubic symmetry. Then a mathematical optimization formulation is

established for finding metamaterials with ideal elastic isotropy and extreme negative Poisson's ratio (NPR), which are a kind of unimode metamaterials. Novel unimode microstructures have been found and studied.

3) A bi-material continuum topology optimization method for designing 3D isotropic microstructures is developed. Then a mathematical optimization formulation is established for finding isotropic composite metamaterials with ZTE and NPR. A novel ZTE-NPR microstructure has been found and studied.

4) A bi-material discrete topology optimization method is developed by using a 3D bi-material ground structure with the geometric cubic symmetry. Then a mathematical optimization formulation is established for finding isotropic auxetic metamaterials with negative thermal expansion (NTE). Novel strut-based microstructures with tunable thermal expansion and tunable auxeticity have been found and studied.

This research has not yet prototyped the topologically optimized designs and conducted physical in-lab testing, due to the challenge in using current additive manufacturing techniques. However, this research will use industrial standard commercial software as an easy-to-use design of experiment to demonstrate the effective properties and the macroscopic behaviors of the lattice metamaterials designed by the developed methods. With advancements in simulation techniques, numerical validation using well-accepted commercial software tools has become an essential step in verifying and studying the optimized designs before they are physically prototyped and tested. This allows for the evaluation of the design's performance and necessary adjustments to be made before investing in costly physical prototyping and lab testing. Numerical validation also allows for further optimization and refinement of the designs to achieve desired properties.

1.5. Thesis outline

This research focuses on topological design of 3D lattice metamaterials with unusual mechanical properties. It consists of six chapters and is organized as follows:

Chapter 1:

This chapter introduces the background and key contributions of this research.

Chapter 2:

This chapter presents a topological design method for finding pentamode metamaterials with at least orthotropic symmetry. Novel pentamode microstructures and their effective material properties are introduced.

Chapter 3:

This chapter presents a topological design method for finding isotropic auxetic metamaterials with extreme Poisson's ratios. Novel unimode microstructures and their effective material properties are introduced.

Chapter 4:

This chapter presents a topological design method for finding isotropic auxetic metamaterials with zero thermal expansion. A novel NPR-ZTE microstructure and its effective material properties are introduced.

Chapter 5:

This chapter presents a topological design method for finding isotropic NPR-NTE metamaterials. Novel strut-based microstructures and their tunable thermoelastic properties are introduced.

Chapter 6:

This chapter summarizes the research of this thesis and introduces the prospects.

Chapter 2 Design of Pentamode Metamaterials with At Least Elastic Orthotropic Symmetry

2.1. Introduction

This chapter is a modified version of the journal paper titled “Topological design of pentamode lattice metamaterials using a ground structure method”, which was published in *Materials & Design* (Volume 202, 109523).

Pentamode metamaterials belong to a kind of 3D solid mechanical metamaterials that are artificially architected to only bear single mode of stress [128]. A pentamode metamaterial has only one non-zero eigenvalue of its sixth-order elastic stiffness matrix [128, 129]. Take an isotropic pentamode metamaterial as an example, it has a finite bulk modulus but a vanishing shear modulus, and it can only bear hydrostatic stress. In contrast, a unimode metamaterial has only one zero eigenvalue of its elastic stiffness matrix [128], which will be studied in Chapter 3. Such extreme mechanical properties of pentamode and unimode metamaterials are obtained from their microstructural geometries rather than constituent materials.

The pentamode metamaterial was first designed by Milton and Cherkaev in 1995 [128]. It consists of a diamond-type unit cell with four double-cone bars jointed at a strictly point-like tip. However, lattice structures with such point-like tips cannot be stably used in real-world applications. Therefore, the infinitely small joints were given finite cross-sections to facilitate manufacturing of the pentamode lattice structures in practice

[130]. This conventional diamond-type pentamode microstructure [130] is illustrated in Figure 2.1a, which consists of double-cone bars featuring a small diameter at the joints and a relatively large diameter at the midspan as described in Figure 2.1b. For the diamond-type pentamode microstructure, Cai et al. [131] found that using asymmetric double-cone bars can increase its ratio of bulk modulus to shear modulus. Huang et al. [132] quantitatively compared the pentamode behavior and acoustic bandgaps of the diamond-type pentamode microstructures with five different cross-sectional shapes, and they found that the triangle case performs best with the lower frequency and broader bandwidth than other four shapes.

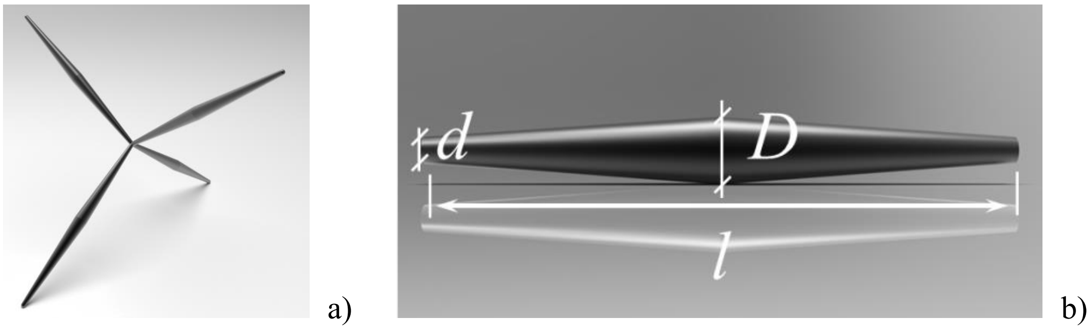

Figure 2.1. Diamond-type pentamode microstructure with double-cone bars

Isotropic pentamode metamaterials can uncouple the compression and shear waves, since ideally their bulk moduli are infinitely larger than the shear moduli [130]. In other words, isotropic pentamode metamaterials are difficult to be compressed while easily to flow away, for which they are also named as metafluids [133]. Kadic et al. [130] first fabricated the diamond-type pentamode lattice structure using the dip-in direct-laser-writing optical lithography. Testing results of additively manufactured diamond-type pentamode lattice structures revealed that the shear and Young's moduli scale approximately according to three powers of the ratio between the joint diameter and the lattice constant [134], and the elastic modulus and yield stress were decoupled from the relative density [135].

Pentamode metamaterials are promising for translating the concept of transformation optics to transformation elastostatics and transformation elastodynamics [136-142]. In 2008, Norris [136] investigated the transformation acoustic cloaks and noted that ideal acoustic cloaks can be achieved through pentamode metamaterials. Compared with conventional inertial cloaks, pentamode acoustic cloaks can avoid mass singularity and be engineered with pure solid materials, and they are theoretically broadband since they invoke only quasi-static stiffness of pentamode metamaterials [139]. Potential applications of pentamode metamaterials in other fields have also been studied recently. For instance, Bückmann et al. [143] designed an elasto-mechanical unfeelability cloak using the conventional diamond-type pentamode metamaterials to hide hard objects and make them unfeelable. Hai et al. [144] used bimodal structures to design 2D unfeelable mechanical cloaks to reduce the influence of a hole in the structure on stress concentrations and redistribute the strain. Fabbrocino et al. [145] proposed a tunable seismic base-isolation device by the combination of pentamode lattices and tensegrity structures.

It should be noted that several so-called pentamode metamaterials given in literatures [138-141] are 2D bimode metamaterials in fact. Strictly speaking, they should not be classified as pentamode metamaterials, because the sixth-order elastic stiffness matrix of a 3D material is a necessity to define the term of penta referring to five. A pentamode metamaterial can be considered as a 3D extension of a 2D bimode honeycomb metamaterial that has three linkages jointed at a point. Therefore, Milton and Cherkaev [128] noted that a natural candidate might have four linkages jointed at a point, which helped to find the diamond-type pentamode microstructure. Inspired by the concept of the Bravais lattices, Mejica and Lantada [146] presented a library of microstructures that were claimed to be pentamode in 2013, but Xu [147] stated that these microstructures are not pentamode at all, although they have large ratios of the bulk modulus to the shear modulus. This phenomenon will be explained in Section 2.2 of this thesis. In 2015, Xu [147] presented five pentamode microstructures that all have only one non-zero eigenvalue of the effective elastic stiffness matrix. In 2019, Li and Vipperman [148] and Huang et al. [149] further proposed two isotropic pentamode microstructures. From the above, we can find that only seven new pentamode microstructures have been found but through ad hoc and empirical design methods since 1995. A generative design optimization approach that can systematically find novel pentamode microstructures is still missing.

Milton and Cherkaev [128] noted that pentamode metamaterials can be anisotropic. However, this possibility was not addressed until 2013, when Kadic et al. [150] introduced intentional anisotropy into the conventional diamond-type pentamode microstructure by moving just one connection point along the space diagonal. As mentioned by Milton et al. [151], pentamode metamaterials should be able to bear any chosen stress rather than only hydrostatic stress. Anisotropic pentamode metamaterials are the prerequisite for realizing many applications including acoustic clocks based on transformation elastodynamics [150]. Hence, this chapter will focus on topology optimization of more general pentamode metamaterials that are not limited to be isotropic. An evolutionary ground structure method using the genetic algorithm is proposed to find novel pentamode microstructures with at least orthotropic symmetry.

2.2. Necessary and sufficient condition

This section will rigorously derive the necessary and sufficient condition required for elastic constants of pentamode metamaterials with at least orthotropic symmetry. It should be noted that the derivation here is valid for linear elasticity. For the 3D elasticity problem, Hooke's law is here considered in the form $\boldsymbol{\sigma} = \boldsymbol{C}\boldsymbol{\varepsilon}$, where $\boldsymbol{\sigma}$ is the vector of stress, and $\boldsymbol{\varepsilon}$ is the vector of strain. For any elastic material with the orthotropic symmetry, its elastic stiffness matrix $\boldsymbol{C}$ is defined in Equation (2.1). An elastic stiffness matrix is always positive semidefinite, i.e., $C_{ii} \geq 0\ (i = 1,2,3,4,5,6)$.

$$\boldsymbol{C} = \begin{bmatrix} C_{11} & C_{12} & C_{13} & 0 & 0 & 0 \\ C_{12} & C_{22} & C_{23} & 0 & 0 & 0 \\ C_{13} & C_{23} & C_{33} & 0 & 0 & 0 \\ 0 & 0 & 0 & C_{44} & 0 & 0 \\ 0 & 0 & 0 & 0 & C_{55} & 0 \\ 0 & 0 & 0 & 0 & 0 & C_{66} \end{bmatrix} \tag{2.1}$$

The essential definition of a pentamode metamaterial is that it has only one non-zero eigenvalue of its sixth-order elastic stiffness matrix [128]. The characteristic polynomial of $\boldsymbol{C}$ in Equation (2.1) can be defined as:

$$|\boldsymbol{C}-\lambda\boldsymbol{I}| = (C_{44}-\lambda)(C_{55}-\lambda)(C_{66}-\lambda)(A_1+(A_2+(A_3-\lambda)\lambda)\lambda) = 0 \tag{2.2}$$

where

$$\begin{cases} A_1 = C_{11}C_{22}C_{33} + 2C_{12}C_{13}C_{23} - C_{11}{C_{23}}^2 - C_{22}{C_{13}}^2 - C_{33}{C_{12}}^2 \\ A_2 = {C_{12}}^2 - C_{11}C_{22} + {C_{13}}^2 - C_{11}C_{33} + {C_{23}}^2 - C_{22}C_{33} \\ A_3 = C_{11} + C_{22} + C_{33} \end{cases} \tag{2.3}$$

To find the necessary and sufficient condition for this characteristic polynomial to have only one non-zero root, we should consider through the following two cases.

The first case is that at least one of C_{44}, C_{55} and C_{66} is positive, e.g., $C_{44} > 0$. If so, the only one non-zero eigenvalue should be $\lambda = C_{44}$, and then the following conditions must be satisfied:

$$\begin{cases} C_{55} = C_{66} = 0 \\ A_1 = A_2 = A_3 = 0 \end{cases} \tag{2.4}$$

Since the elastic stiffness matrix is positive semidefinite, the second equation in Equation (2.4) equals to the following condition:

$$C_{11} = C_{22} = C_{33} = C_{12} = C_{13} = C_{23} = 0 \tag{2.5}$$

The derivation for $C_{55} > 0$ or $C_{66} > 0$ is the same. Therefore, the general necessary and sufficient condition for this first case is that only one of C_{44}, C_{55} and C_{66} is positive while all other elastic constants are zero, which corresponds to a material that can only bear one shear stress mode, which is well in line with the definition of pentamode materials in [128].

In this work, we will only consider the second case described below for design optimization since it is more complicated and physically meaningful. The second case is that at least one of C_{11}, C_{22} and C_{33} is positive. If so, the only one non-zero eigenvalue should be $\lambda = A_3 = C_{11} + C_{22} + C_{33}$, and then the following conditions must be satisfied:

$$\begin{cases} C_{44} = C_{55} = C_{66} = 0 \\ A_1 = A_2 = 0 \end{cases} \tag{2.6}$$

For the equation $A_1 = 0$ in Equation (2.6) to have three real roots as C_{12}, C_{13} and C_{23}, the following conditions must be satisfied:

$$\begin{cases} 4{C_{13}}^2{C_{23}}^2 - 4C_{33}\left(C_{11}{C_{23}}^2 + C_{22}{C_{13}}^2 - C_{11}C_{22}C_{33}\right) \geq 0 \\ 4{C_{12}}^2{C_{23}}^2 - 4C_{22}\left(C_{11}{C_{23}}^2 + C_{33}{C_{12}}^2 - C_{11}C_{22}C_{33}\right) \geq 0 \\ 4{C_{12}}^2{C_{13}}^2 - 4C_{11}\left(C_{22}{C_{13}}^2 + C_{33}{C_{12}}^2 - C_{11}C_{22}C_{33}\right) \geq 0 \end{cases} \tag{2.7}$$

which can be simplified as:

$$\begin{cases} \left({C_{13}}^2 - C_{11}C_{33}\right)\left({C_{23}}^2 - C_{22}C_{33}\right) \geq 0 \\ \left({C_{12}}^2 - C_{11}C_{22}\right)\left({C_{23}}^2 - C_{22}C_{33}\right) \geq 0 \\ \left({C_{12}}^2 - C_{11}C_{22}\right)\left({C_{13}}^2 - C_{11}C_{33}\right) \geq 0 \end{cases} \tag{2.8}$$

These inequality equations require the values of ${C_{12}}^2 - C_{11}C_{22}$, ${C_{13}}^2 - C_{11}C_{33}$ and ${C_{23}}^2 - C_{22}C_{33}$ to have no opposite signs. Combined with the equation $A_2 = 0$ in Equation (2.6), we can know that the following condition must be satisfied:

$${C_{12}}^2 - C_{11}C_{22} = {C_{13}}^2 - C_{11}C_{33} = {C_{23}}^2 - C_{22}C_{33} = 0 \tag{2.9}$$

which can be simplified to be:

$$\begin{cases} C_{12} = a\sqrt{C_{11}C_{22}} \\ C_{13} = b\sqrt{C_{11}C_{33}} \\ C_{23} = c\sqrt{C_{22}C_{33}} \end{cases} \tag{2.10}$$

where

$$a = \pm 1, \qquad b = \pm 1, \qquad c = \pm 1 \tag{2.11}$$

Moreover, from the equation $A_1 = 0$ in Equation (2.6), we can know that:

$$\begin{aligned} C_{11}C_{22}C_{33} + 2C_{12}C_{13}C_{23} &= (1 + 2abc)C_{11}C_{22}C_{33} \\ &= C_{11}{C_{23}}^2 + C_{22}{C_{13}}^2 + C_{33}{C_{12}}^2 \geq 0 \end{aligned} \tag{2.12}$$

This inequality equation additionally requires that:

$$abc \neq -1 \tag{2.13}$$

Equation (2.11) and (2.13) can be combined to meet the following four cases:

$$\begin{cases} a = b = c = 1 & \text{or} \\ a = 1, b = c = -1 & \text{or} \\ b = 1, a = c = -1 & \text{or} \\ c = 1, a = b = -1 \end{cases} \tag{2.14}$$

It should be noted that the condition above also contains the case that only one or two of C_{11}, C_{22} and C_{33} is positive while all other elastic constants are zero. Therefore, the necessary and sufficient condition required for elastic materials with at least orthotropic symmetry to be pentamode for the second case is the combination of Equation (2.10), (2.14) and the equation $C_{44} = C_{55} = C_{66} = 0$ in Equation (2.6). When satisfying this necessary and sufficient condition, the elastic stiffness matrix can be simplified as:

$$\boldsymbol{C} = \begin{bmatrix} C_{11} & a\sqrt{C_{11}C_{22}} & b\sqrt{C_{11}C_{33}} & 0 & 0 & 0 \\ a\sqrt{C_{11}C_{22}} & C_{22} & c\sqrt{C_{22}C_{33}} & 0 & 0 & 0 \\ b\sqrt{C_{11}C_{33}} & c\sqrt{C_{22}C_{33}} & C_{33} & 0 & 0 & 0 \\ 0 & 0 & 0 & 0 & 0 & 0 \\ 0 & 0 & 0 & 0 & 0 & 0 \\ 0 & 0 & 0 & 0 & 0 & 0 \end{bmatrix} \tag{2.15}$$

The eigenvector of the only one non-zero eigenvalue $\lambda = C_{11} + C_{22} + C_{33}$ is:

$$\boldsymbol{x} = \begin{bmatrix} ab\sqrt{C_{11}} & ac\sqrt{C_{22}} & bc\sqrt{C_{33}} & 0 & 0 & 0 \end{bmatrix}^{\mathrm{T}} \tag{2.16}$$

As mentioned above, a pentamode metamaterial has only one non-zero eigenvalue of its sixth-order elastic stiffness matrix [128]. It indicates that there are five independent strain cases that each strain case or their linear combinations will produce zero stress and zero strain energy [133]. It also indicates that this kind of materials can only bear single mode of stress, which corresponds to the eigenvector associated with the non-zero eigenvalue [128]. As a special case, isotropic pentamode metamaterials must have the following form of elastic stiffness matrix:

$$\boldsymbol{C} = \begin{bmatrix} C_{11} & C_{11} & C_{11} & 0 & 0 & 0 \\ C_{11} & C_{11} & C_{11} & 0 & 0 & 0 \\ C_{11} & C_{11} & C_{11} & 0 & 0 & 0 \\ 0 & 0 & 0 & 0 & 0 & 0 \\ 0 & 0 & 0 & 0 & 0 & 0 \\ 0 & 0 & 0 & 0 & 0 & 0 \end{bmatrix} \tag{2.17}$$

For the above elastic stiffness matrix, there is only one non-zero eigenvalue $\lambda = 3C_{11}$, and its corresponding eigenvector is $[1 \quad 1 \quad 1 \quad 0 \quad 0 \quad 0]^{\mathrm{T}}$. We can find that this non-zero eigenvalue is exactly three times the bulk modulus $B = C_{11}$, and the eigenvector indicates that the material can only bear the hydrostatic stress. Therefore, isotropic pentamode metamaterials are equivalently identified by a finite bulk modulus and a vanishing shear modulus [130, 134]. However, it is not applicable to non-isotropic pentamode metamaterials. For pentamode metamaterials with at least orthotropic symmetry, we can find that the non-zero eigenvalue $\lambda = C_{11} + C_{22} + C_{33}$ is not always proportional to its bulk modulus in Equation (2.18), and the eigenvector in Equation (2.16) does not always represent hydrostatic stress either.

$$B = \frac{C_{11}{C_{23}}^2 + C_{22}{C_{13}}^2 + C_{33}{C_{12}}^2 - 2C_{12}C_{13}C_{23} - C_{11}C_{22}C_{33}}{{C_{12}}^2 + {C_{13}}^2 + {C_{23}}^2 + 2(C_{11}C_{23} + C_{22}C_{13} + C_{33}C_{12} - C_{12}C_{13} - C_{12}C_{23} - C_{13}C_{23}) - (C_{11}C_{22} + C_{11}C_{33} + C_{22}C_{33})} \tag{2.18}$$

Therefore, a relatively large ratio of the bulk modulus to the shear modulus is no more a sufficient condition for non-isotropic pentamode metamaterials. In other words, such a ratio cannot be used to identify whether an orthotropic or transverse isotropic material is pentamode or not. For example, although the microstructures proposed in [146] have large ratios of the bulk modulus to the shear modulus, they are not isotropic and their elastic stiffness matrices have more than one non-zero eigenvalues.

2.3. Computational design method

In this section, we propose a topology optimization method to find novel pentamode microstructures with at least elastic orthotropic symmetry. Since potential pentamode microstructures to be designed in this chapter have nearly zero effective shear moduli, it is expected that these microstructures should behave like mechanisms and consist of hinge-type joints. However, it is difficult to obtain an optimized design with hinge joints by using topology optimization methods for continuum structures with the solid finite elements. Hence, we will propose a ground structure method for design of strut-based pentamode microstructures.

2.3.1. Ground structure with geometric orthogonal symmetry

The method presented in this work is developed upon the utilization of a prescribed ground structure that includes both active and inactive bars to describe potential topologies of designs. We assume that there is a discrete structure with a fixed number of bars, which is termed as the ground structure. A portion of the bars is selected as active, while the remaining bars are considered inactive. The active bars are those that can carry loads and have significant contributions to the mechanical properties of the microstructure, while the inactive bars have ignorable influence on the effective properties. After removing all inactive bars from the ground structure, a final design comprising only active bars is constructed. The topology optimization is then a numerical iterative process to determine which bars should be active and which should be inactive with the aim of reaching targeted mechanical properties. In other words, the active statuses of bars in the ground structure are chosen as design variables.

For a given set of mesh nodes, the easiest way to generate a ground structure is just linking every two nodes. The number of bars for such a fully connected ground structure is equal to $({n_{node}}^2 - n_{node})/2$, where n_{node} is the number of nodes. Zegard and Paulino [62] proposed a method to generate ground structures in arbitrary 3D domains with control in the level of redundancy or inter-connectedness of ground structures. However, it cannot guarantee that the optimized designs must have any material property symmetry. Therefore, a new ground structure with geometric orthogonal symmetry is proposed in this chapter to ensure that the optimized designs always have at least elastic orthotropic symmetry.

We suppose there are $5 \times 5 \times 5$ Cartesian mesh nodes centered at the origin and aligned with coordinate axes as shown in Figure 2.2a, and then the corresponding ground structure with geometric orthogonal symmetry will be as shown in Figure 2.2b. Due to the geometric orthogonal symmetry, the design variables are changed from $\boldsymbol{\rho}$ to $\widetilde{\boldsymbol{\rho}}$ as defined in Equation (2.19), which is still a vector of binary design variables.

$$\widetilde{\boldsymbol{\rho}} = [\tilde{\rho}_1 \quad \tilde{\rho}_2 \quad \cdots \quad \tilde{\rho}_{n_{des}-1} \quad \tilde{\rho}_{n_{des}}] \tag{2.19}$$

where n_{des} is the number of design variables. For the ground structure in Figure 2.2b, the numbers of bars and design variables are respectively 2544 and 405. However, for a fully connected ground structure, both the bar number and design variables will be as large as 7750.

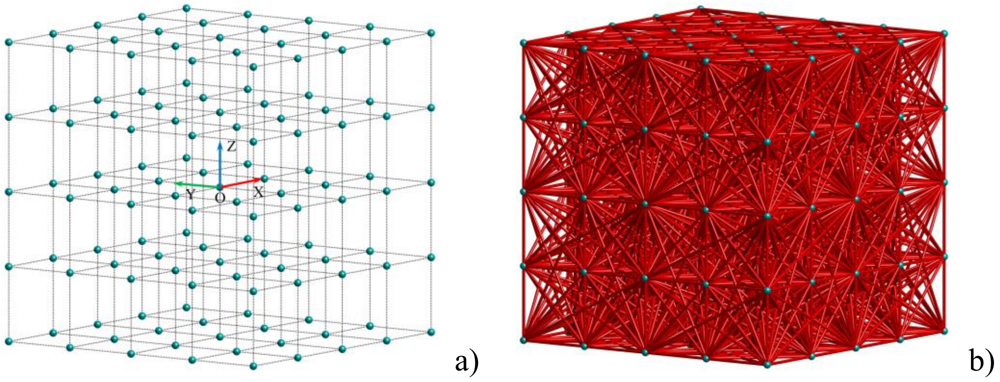

Figure 2.2. Cartesian mesh nodes and the corresponding ground structure

The bars in the ground structure are divided into five groups as shown in Figure 2.3. The bars of the first group are collinear with one coordinate axis and symmetric about one coordinate plane. Each of these bars has no mirrored copies in the ground structure as shown in Figure 2.3a. Therefore, 6 design variables of this group correspond to 6 bars. The second group consists of two types of bars. One type is collinear with one coordinate axis and on the side of one coordinate plane. The other type is coplanar with one coordinate plane, parallel but not collinear with one coordinate axis and then symmetric about another coordinate plane. Each of these bars has another mirrored copy in the ground structure as shown in Figure 2.3b. Therefore, 33 design variables of this group correspond to 66 bars. The bars of the third group are coplanar with one coordinate plane and on the side of other coordinate planes. Each of these bars has other three mirrored copies in the ground structure as shown in Figure 2.3c. Therefore, 90 design variables of this group correspond to 360 bars. The bars of the fourth group are symmetric about one coordinate plane and parallel but not coplanar with other coordinate planes. Each of these bars has other three mirrored copies in the ground structure as shown in Figure 2.3d. Therefore, 24 design variables of this group correspond to 96 bars. Finally, the fifth group is obtained by linking every two nodes in the same octant and then subtracting bars that already belong to the above four groups. Each of these bars has other seven mirrored copies in the ground structure as shown in Figure 2.3e. Therefore, 252 design variables of this group correspond to 2016 bars.

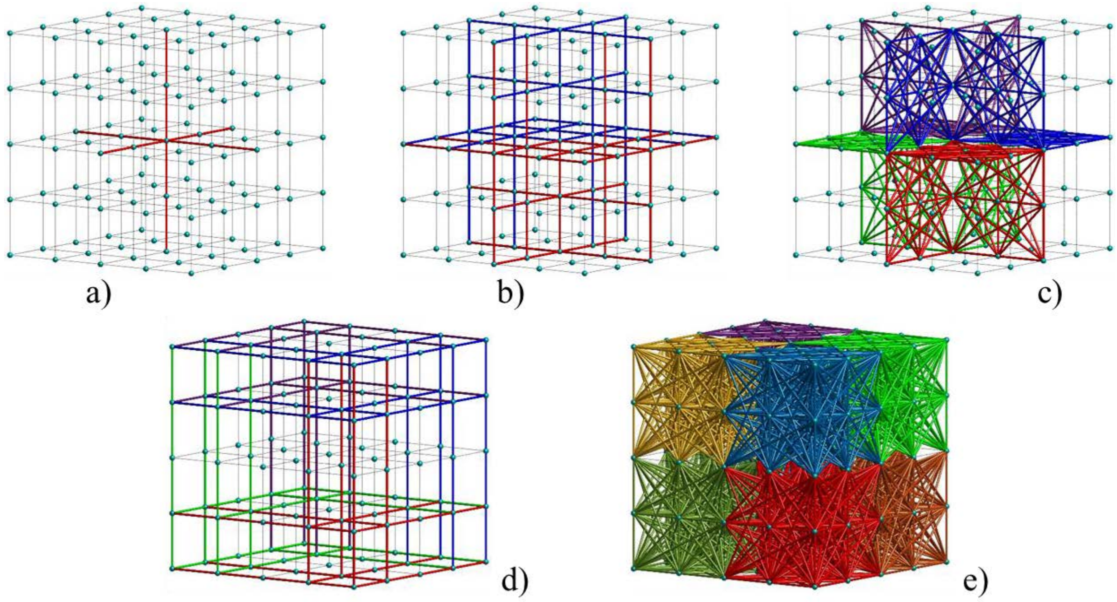

Figure 2.3. Five groups of bars in the ground structure

2.3.2 Computational homogenization method

Lattice materials are composed of replicated unit cells that are engineered to have specific properties, which can be macroscopically considered as a piece of homogeneous materials. The computational homogenization method [152] is such a numerical technique for calculating effective material properties of periodic architected unit cells. Here, we adopt the following energy-based homogenization method to evaluate effective elastic stiffness matrices of potential designs described by the ground structure:

$$C_{ij}^{H} = \frac{1}{V}\boldsymbol{U}_i{}^{T}\boldsymbol{K}\boldsymbol{U}_j \quad (i, j = 1, 2, \dots, 6) \tag{2.20}$$

where C_{ij}^{H} is one of effective elastic constants, V is the total volume of the unit cell including its voids, $\boldsymbol{K}$ is the global stiffness matrix of the unit cell and $\boldsymbol{U}_i$ is the vector of displacement fields in the i-th load case. Six load cases are needed for the homogenization of a 3D material. In different load case, nodal displacements are calculated by considering a different periodic boundary condition. For every two nodes of a unit cell that are periodically coincident, e.g., node p and node q, the following multi-point equation constraints are imposed on their translational displacements $\boldsymbol{u}$:

$$\boldsymbol{u}(\boldsymbol{x}_p) - \boldsymbol{u}(\boldsymbol{x}_q) = \bar{\boldsymbol{\varepsilon}}(\boldsymbol{x}_p - \boldsymbol{x}_q) \tag{2.21}$$

where $\boldsymbol{x}$ is the vector of nodal coordinates, and $\bar{\boldsymbol{\varepsilon}}$ is a matrix composed of macroscopic average strains:

$$\bar{\boldsymbol{\varepsilon}} = \begin{bmatrix} \bar{\varepsilon}_{11} & \bar{\gamma}_{12}/2 & \bar{\gamma}_{13}/2 \\ \bar{\gamma}_{12}/2 & \bar{\varepsilon}_{22} & \bar{\gamma}_{23}/2 \\ \bar{\gamma}_{13}/2 & \bar{\gamma}_{23}/2 & \bar{\varepsilon}_{33} \end{bmatrix} \tag{2.22}$$

where $\bar{\gamma}$ is an engineering shear strain. For each of six load cases, sequentially one of six strain components is set as one, and then the rest strain components are set as zero. For example, $\boldsymbol{U}_1$ is calculated with $\bar{\boldsymbol{\varepsilon}} = [1\ 0\ 0;\ 0\ 0\ 0;\ 0\ 0\ 0]$ in the first load case, and $\boldsymbol{U}_4$ is calculated with $\bar{\boldsymbol{\varepsilon}} = [0\ 0\ 0;\ 0\ 0\ 0.5;\ 0\ 0.5\ 0]$ in the fourth load case.

It is worthy of note that, for beam elements, the rotational displacements $\boldsymbol{\theta}$ of periodically coincident nodes p and q have the following relationship:

$$\boldsymbol{\theta}(\boldsymbol{x}_p) - \boldsymbol{\theta}(\boldsymbol{x}_q) = \boldsymbol{0} \tag{2.23}$$

Finally, no matter solid elements, truss elements, or beam elements are used for the computational homogenization, translational displacements of one arbitrary node are fixed as zero to avoid rigid body motions.

2.3.3. Mathematical optimization formulation

After obtaining the homogenized effective elastic stiffness matrix, we should establish a fitness function to justify whether it satisfies the necessary and sufficient condition derived in Section 2.2 for pentamode metamaterials with at least elastic orthotropic symmetry. Firstly, for metamaterials with at least orthotropic symmetry, it is obvious that the tension-shear coupling terms in the elastic stiffness matrix must be zero. We exclude these terms from the objective function and treat them as equality constraints in the mathematical model, because they can be strictly satisfied by guaranteeing that the ground structure has the geometric orthogonal symmetry. Secondly, we rewrite the Equation (2.10) as the following form:

$$\frac{a\sqrt{C_{11}C_{22}}}{C_{12}} - 1 = \frac{b\sqrt{C_{11}C_{33}}}{C_{13}} - 1 = \frac{c\sqrt{C_{22}C_{33}}}{C_{23}} - 1 = 0 \tag{2.24}$$

which can be further simplified as:

$$\left(\frac{a\sqrt{C_{11}C_{22}}}{C_{12}} - 1\right)^2 + \left(\frac{b\sqrt{C_{11}C_{33}}}{C_{13}} - 1\right)^2 + \left(\frac{c\sqrt{C_{22}C_{33}}}{C_{23}} - 1\right)^2 = 0 \tag{2.25}$$

Finally, since $C_{ii} \geq 0\ (i = 1,2,3,4,5,6)$, we can rewrite the equation $C_{44} = C_{55} = C_{66} = 0$ in the Equation (2.6) as the following form:

$$\frac{C_{44} + C_{55} + C_{66}}{C_{11} + C_{22} + C_{33}} = 0 \tag{2.26}$$

Therefore, the sum of left-side terms in Equation (2.25) and Equation (2.26) must also be zero. Then a general mathematical optimization formulation can be established as Equation (2.27). In this formulation, $\boldsymbol{C}^H$ is the effective elastic stiffness matrix of the ground structure calculated by the computational homogenization method considering the periodic boundary condition [152], $\boldsymbol{\rho}$ is a vector of binary variables representing whether each bar in the ground structure is active or not, n_{bar} is the number of bars in the ground structure. A choice of a, b and c that belongs to the four cases in Equation (2.14) should be determined in advance. We would emphasize that the dominator ${C_{11}}^H(\boldsymbol{\rho}) + {C_{22}}^H(\boldsymbol{\rho}) + {C_{33}}^H(\boldsymbol{\rho})$ is not necessary in the objective function, but it is used to normalize the last term to enhance the optimization performance.

Find: $\boldsymbol{\rho} = [\rho_1 \quad \rho_2 \quad \cdots \quad \rho_{n_{bar}-1} \quad \rho_{n_{bar}}]$

Min:

$$f(\boldsymbol{\rho}) = \left(\frac{a\sqrt{{C_{11}}^H(\boldsymbol{\rho}){C_{22}}^H(\boldsymbol{\rho})}}{{C_{12}}^H(\boldsymbol{\rho})} - 1\right)^2 + \left(\frac{b\sqrt{{C_{11}}^H(\boldsymbol{\rho}){C_{33}}^H(\boldsymbol{\rho})}}{{C_{13}}^H(\boldsymbol{\rho})} - 1\right)^2 + \left(\frac{c\sqrt{{C_{22}}^H(\boldsymbol{\rho}){C_{33}}^H(\boldsymbol{\rho})}}{{C_{23}}^H(\boldsymbol{\rho})} - 1\right)^2 + \frac{{C_{44}}^H(\boldsymbol{\rho}) + {C_{55}}^H(\boldsymbol{\rho}) + {C_{66}}^H(\boldsymbol{\rho})}{{C_{11}}^H(\boldsymbol{\rho}) + {C_{22}}^H(\boldsymbol{\rho}) + {C_{33}}^H(\boldsymbol{\rho})} \tag{2.27}$$

$$\text{S.t.} \begin{cases} {C_{ij}}^H(\boldsymbol{\rho}) = 0, \quad i = 1,2,3 \quad j = 4,5,6 \\ {C_{45}}^H(\boldsymbol{\rho}) = {C_{46}}^H(\boldsymbol{\rho}) = {C_{56}}^H(\boldsymbol{\rho}) = 0 \end{cases}$$

The constraints in Equation (2.27) are to ensure that the optimized designs have at least orthotropic symmetry. When the objective function value approaches to zero (globally minimum value), the necessary and sufficient condition required for elastic constants of pentamode metamaterials with at least orthotropic symmetry will be satisfied. It is noted that for such an inverse design problem, multiple solutions may exist.

As mentioned above, the design variables are 0 and 1 logical variables representing which bars are active. However, it does not mean that inactive bars are not included in finite element analyses of the computational homogenization. That is because the total stiffness matrix of a mechanism-type pentamode lattice that only consists of active bars is singular in numerical. Therefore, inactive bars are assigned with relatively small axial stiffness and then included in the computational homogenization. This can prevent the total stiffness matrix from being singular but the effect to the value of the effective elastic stiffness matrix is small and acceptable.

2.3.4. Geometric constraints

Definitions of intersection and overlap of bars are illustrated in Figure 2.4.

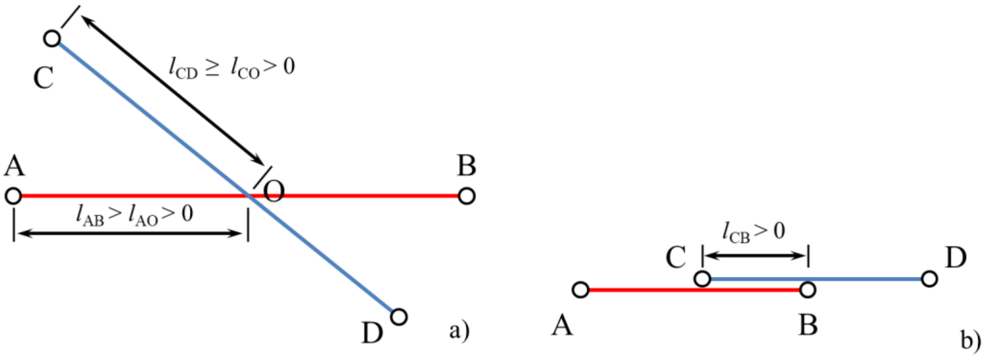

Figure 2.4. Intersection and overlap of two bars

Geometric constraints on intersection and overlap of bars in ground structure methods have already been introduced for macro-scale structures [153, 154], but not yet been introduced for microstructural designs [63, 64, 155]. In engineering, optimization solutions with existence of intersection or overlap of bars are unrealistic designs [154]. Such impractical topologies should be avoided for optimized microstructures. Therefore, constraints on intersection and overlap of bars should be imposed on optimization design of pentamode metamaterials. Cui et al. [154] provided a mathematical recognition method for intersection and overlap of bars in 3D ground structures. However, it is not computationally efficient, e.g., linear equations should be solved for each two bars. Based on calculating the shortest line between two 3D lines, we propose a new mathematical recognition method in this chapter.

As illustrated in Figure 2.5, two 3D lines AB and CD do not intersect each other at a point, and the line EF is the shortest line between them. Coordinates of the points E and

F are defined as:

$$\begin{cases} \boldsymbol{x}_{\mathrm{E}} = \boldsymbol{x}_{\mathrm{A}} + \mu_{\mathrm{E}}(\boldsymbol{x}_{\mathrm{B}} - \boldsymbol{x}_{\mathrm{A}}) \\ \boldsymbol{x}_{\mathrm{F}} = \boldsymbol{x}_{\mathrm{C}} + \mu_{\mathrm{F}}(\boldsymbol{x}_{\mathrm{D}} - \boldsymbol{x}_{\mathrm{C}}) \end{cases} \tag{2.28}$$

The values of μ_{E} and μ_{F} range from negative to positive infinity. μ_{E} can be calculated by the following formula, while μ_{F} can be calculated by substituting subscripts:

$$\mu_{\mathrm{E}} = \frac{d_{\mathrm{ACDC}} d_{\mathrm{DCBA}} - d_{\mathrm{ACBA}} d_{\mathrm{DCDC}}}{d_{\mathrm{BABA}} d_{\mathrm{DCDC}} - d_{\mathrm{DCBA}} d_{\mathrm{DCBA}}} \tag{2.29}$$

where

$$d_{\mathrm{MNOP}} = (x_{\mathrm{M}} - x_{\mathrm{N}})(x_{\mathrm{O}} - x_{\mathrm{P}}) + (y_{\mathrm{M}} - y_{\mathrm{N}})(y_{\mathrm{O}} - y_{\mathrm{P}}) + (z_{\mathrm{M}} - z_{\mathrm{N}})(z_{\mathrm{O}} - z_{\mathrm{P}}) \tag{2.30}$$

When AB and CD intersect, E and F are coincident and the values of μ_{E} and μ_{F} are between 0 and 1. When AB and CD are parallel, the dominator in Equation (2.29) is zero. Details of the related mathematical derivation can be referred to [156].

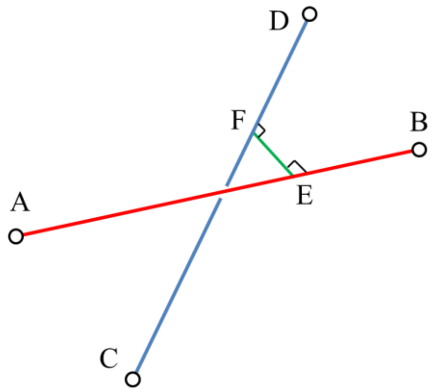

Figure 2.5. Shortest line between two 3D lines

Under the assumption that AB and CD are parallel, if points A, B and C are collinear, lines AB and CD will be collinear. For three points to be collinear, the following equation should be satisfied:

$$\begin{cases}(y_{\mathrm{B}}-y_{\mathrm{A}})(z_{\mathrm{C}}-z_{\mathrm{A}})-(y_{\mathrm{C}}-y_{\mathrm{A}})(z_{\mathrm{B}}-z_{\mathrm{A}})=0\\(x_{\mathrm{C}}-x_{\mathrm{A}})(z_{\mathrm{B}}-z_{\mathrm{A}})-(x_{\mathrm{B}}-x_{\mathrm{A}})(z_{\mathrm{C}}-z_{\mathrm{A}})=0\\(x_{\mathrm{B}}-x_{\mathrm{A}})(y_{\mathrm{C}}-y_{\mathrm{A}})-(x_{\mathrm{C}}-x_{\mathrm{A}})(y_{\mathrm{B}}-y_{\mathrm{A}})=0\end{cases} \tag{2.31}$$

For two lines to be coplanar, the following equation should be satisfied:

$$\overrightarrow{\mathrm{AC}}\cdot\left(\overrightarrow{\mathrm{AB}}\times\overrightarrow{\mathrm{CD}}\right)=0 \tag{2.32}$$

The flowchart about how to detect intersection and overlap of each two bars is given in Figure 2.6.

It should be noted that the binary genetic algorithm, which will be discussed in Section 2.3.5, cannot explicitly enforce nonlinear constraints to be satisfied like mathematical programming methods do. Therefore, geometric constraints on intersection and overlap are added as a penalty term into the original objective function in Equation (2.27). The modified objective function is now defined as:

$$\tilde{f}(\widetilde{\boldsymbol{\rho}})=f(\widetilde{\boldsymbol{\rho}})+w\frac{n_{ins}(\widetilde{\boldsymbol{\rho}})+n_{ovl}(\widetilde{\boldsymbol{\rho}})}{n_{geo}} \tag{2.33}$$

where n_{geo} is the total number of intersection and overlap of the fully active ground structure, n_{ins} is the number of intersections of the current design, n_{ovl} is the number of overlaps of the current design, and w is a weighting factor. For a design without any intersection or overlap of bars, the penalty value becomes zero, and then the modified objective function is the same as the original one. Normalized by the dominator n_{geo}, the penalty value will not be larger than w. Since the value of $f(\widetilde{\boldsymbol{\rho}})$ would approach to zero during the optimization iteration, the value of w can absolutely be a small number but still relatively large enough compared with zero. Therefore, we choose $w=0.001$

in this work.

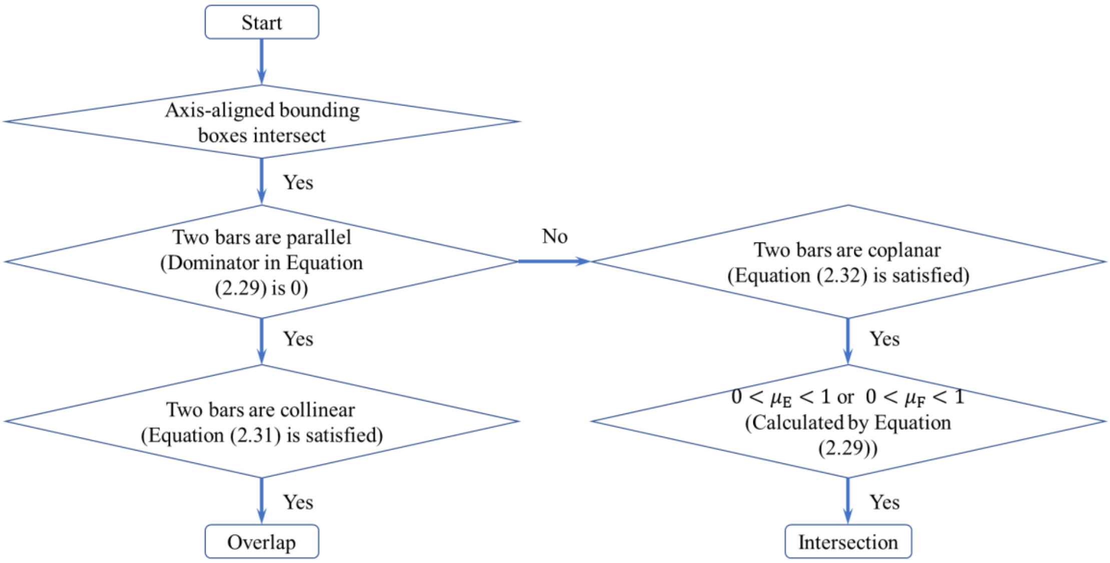

Figure 2.6. Flowchart of the detection method for intersection and overlap of bars

It should be noted that ground structures generated by the method in [62] do not have a single bar connecting the same nodes with other two bars as shown in Figure 2.7. However, these two cases of bars may have different influence on pentamode behaviors of truss-type microstructures, and we cannot determine which case should be adopted for different local locations in the ground structure in advance. Therefore, these two cases of bars both initially exist in the ground structure described in Section 2.3.1. However, we emphasize that since geometric constraints have been imposed as a penalty term in the objective function, such an overlapping case would not exist in the final optimized designs.

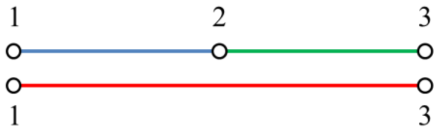

Figure 2.7. Overlapping bars in the ground structure

2.3.5. Optimization solver

Wang et al. [155] studied the design of materials with prescribed nonlinear properties using the ground structure method, which used artificial densities of each bar as continuous design variables and the mathematical programming method to solve the problem. Here, we will also use the ground structure method to design pentamode metamaterials, but the genetic algorithm is adopted to solve this discrete optimization problem with binary variables. The genetic algorithm is well-known as a global optimization method based on natural selection. It randomly generates an initial population. During the iteration, individuals with better fitness values in the current population will be selected as parents. Elite children are individuals with best fitness values, crossover children are generated by combining pairs of parents, and mutation children are generated by making random changes to individual parents [157]. A built-in Matlab function *ga* is used for the numerical implementation of the genetic algorithm.

The genetic algorithm is not often used to solve topology optimization problems for no matter continuum or discrete structures, although it is a well-known optimization method with global searching capability. The first main reason is that there are usually thousands or even millions of continuous design variables in topology optimization problems. It is difficult for genetic algorithms to find a good solution for such large-scale optimization problems with continuous variables. The second reason is that the calculation of the objective and constraint functions with large-scale finite element models is computationally expensive. Unfortunately, hundreds of thousands of candidate solution evaluations are very common for the genetic algorithm, while mathematical programming methods using sensitivity information usually need only up to hundreds of times of finite element analyses. However, the ground structure used in this chapter is a very small-scale truss model with only hundreds of binary design variables. It is also cheap in computation to run finite element analyses in parallel. Therefore, instead of using mathematical programming methods, the genetic algorithm is used as the optimization solver to find the global optimal solution, since the discrete optimization problem here is relatively small scale and cheap in computation.

In this chapter, the max number of optimization iterations is set to 200, and the population size is 1000. Calculation of the objective function runs in parallel using a 6-core Intel i7-8750H CPU. For the maximum 0.2 million times of finite element analyses and computational homogenization evaluations, it only costs around 25 minutes when using the ground structure described in Section 2.3.1. It demonstrates the high computational efficiency of the genetic algorithm as an optimization solver for the developed design method.

Since the genetic algorithm is a non-deterministic method, there will be different initial, intermediate, and final solutions, even when using the same algorithm parameters for solving the same optimization problem. This is a merit for the developed design method to automatically find more than one metamaterial microstructure exhibiting our desired mechanical properties. However, the drawback is that it is inconvenient to duplicate the process for finding a specific optimized design. That is because every time running the genetic algorithm will provides us with different optimized designs, although they may all satisfy our requirements on effective material properties. Therefore, evolution histories of objective and constraint functions are meaningless and not necessary for the developed design methods using the genetic algorithms as optimization solvers in this research. The maturity of these methods can be convincingly demonstrated by their multiple optimized designs that have never been reported in literatures, e.g., a plenty of novel pentamode microstructures in the following section.

2.4. Numerical results

Twenty-four novel pentamode microstructures without any intersection or overlap of bars will be provided here to demonstrate the effectiveness of the proposed design method, including isotropic, transverse isotropic and orthotropic ones. In this section, we will give results for numerical verification of non-isotropic pentamode lattice structures. We will further compare the static mechanical performance of two lattice structures that are respectively assembled by one novel isotropic pentamode microstructure and the conventional diamond-type pentamode microstructure. Moreover, we will study on how to further obtain pentamode microstructures with different relative densities from the optimization results.

2.4.1. Novel pentamode microstructures

As shown in Figure 2.2b, the ground structure is generated by $5 \times 5 \times 5$ mesh nodes with 2544 bars and 405 design variables. The side length of its bounding box is 1 mm. The Young's modulus is 1.138e5 MPa. Constant diameters of active and inactive bars are 0.02 mm and 2.0e-6 mm respectively. We define $\lambda_{\max\_1}$ as the maximum eigenvalue of the effective elastic stiffness matrix of a lattice, $\lambda_{\max\_2}$ as the second maximum eigenvalue, and λ_{R} as the ratio between them. For perfect pentamode metamaterials, λ_{R} should approach infinity. In the following, three tables for material properties are given in this section and note that the unit of elastic constants is MPa. A smaller scale of $2 \times 2 \times 2$ periodic array is given on the right side in a smaller scale together with the microstructure on the left side in each sub-figure.

Using the developed design method, totally twenty-four novel pentamode microstructures have been found, including isotropic, transverse isotropic, and orthotropic microstructures. These pentamode microstructures are respectively shown in Figure 2.8-Figure 2.10. The corresponding effective elastic stiffness matrices and eigenvalue ratios are respectively listed in Table 2.1-Table 2.3. From these tables, we can see that the homogenized effective elastic stiffness matrices of these twenty-four microstructures all satisfy the requirement of pentamode metamaterials.

2.4.2. Bearable stress modes of pentamode microstructures

As mentioned previously, pentamode metamaterials can bear only single mode of stress, which is proportional to the eigenvector associated with the non-zero eigenvalue of the elastic stiffness matrix [128]. Here, we name it as the bearable stress mode. For non-isotropic pentamode microstructures obtained by topology optimization in this chapter, their feature is that they can bear load cases proportional to the Equation (2.16), which is named as the bearable load case here. We will give linear static analysis results of lattice structures assembled by non-isotropic pentamode microstructures to verify that they are stiffer when subjected to their bearable load cases. Two microstructures Trans-a and Ortho-a are chosen here as examples.

Table 2.1. Effective properties of isotropic pentamode microstructures

	a	b	c	d	e	f	g	h
C_{11}	16.519	22.908	25.546	27.680	34.896	33.707	95.491	125.376
C_{22}	16.519	22.908	25.546	27.680	34.896	33.707	95.491	125.376
C_{33}	16.519	22.908	25.546	27.680	34.896	33.707	95.491	125.376
C_{12}	16.519	22.908	25.545	27.680	34.896	33.707	95.491	125.376
C_{13}	16.519	22.908	25.545	27.680	34.896	33.707	95.491	125.376
C_{23}	16.519	22.908	25.545	27.680	34.896	33.707	95.491	125.376
C_{44}	3.16e-5	3.20e-5	3.19e-5	3.03e-5	3.22e-5	3.35e-5	3.79e-5	6.10e-5
C_{55}	3.16e-5	3.24e-5	3.19e-5	3.29e-5	3.20e-5	3.35e-5	3.89e-5	5.90e-5
C_{66}	3.03e-5	3.03e-5	3.22e-5	4.27e-5	3.22e-5	3.35e-5	3.77e-5	4.19e-5
$\lambda_{\mathrm{max}\ \_1}$	49.558	68.724	76.636	83.040	104.687	101.120	286.472	376.127
$\lambda_{\mathrm{max}\ \_2}$	6.90e-5	7.19e-5	6.70e-5	8.87e-5	6.69e-5	6.61e-5	6.78e-5	8.09e-5
λ_{R}	7.18e5	9.55e5	1.14e6	9.36e5	1.56e6	1.53e6	4.22e6	4.65e6

Table 2.2. Effective properties of transverse isotropic pentamode microstructures

	a	b	c	d	e	f	g	h
C_{11}	25.582	34.109	40.349	7.323	51.163	20.417	13.287	51.102
C_{22}	25.582	8.527	40.349	29.291	12.791	45.937	53.149	22.712
C_{33}	6.395	34.109	10.087	29.291	51.163	20.417	53.149	51.102
C_{12}	25.582	17.054	40.349	14.646	25.582	30.625	26.574	34.068
C_{13}	12.791	34.109	20.174	14.646	51.163	20.417	26.574	51.102
C_{23}	12.791	17.054	20.174	29.291	25.582	30.625	53.149	34.068
C_{44}	3.29e-5	3.29e-5	3.44e-5	3.29e-5	3.37e-5	6.65e-5	3.37e-5	4.28e-5
C_{55}	3.29e-5	3.03e-5	3.27e-5	4.66e-5	3.03e-5	3.29e-5	3.59e-5	3.64e-5
C_{66}	3.03e-5	3.37e-5	3.44e-5	3.29e-5	3.37e-5	3.03e-5	3.37e-5	3.58e-5
$\lambda_{\mathrm{max}\ \_1}$	57.559	76.745	90.785	65.905	115.117	86.770	119.584	124.917
$\lambda_{\mathrm{max}\ \_2}$	7.69e-5	8.34e-5	7.31e-5	7.75e-5	9.45e-5	1.14e-4	7.34e-5	8.35e-5
λ_{R}	7.49e5	9.20e5	1.24e6	8.50e5	1.22e6	7.63e5	1.63e6	1.50e6

Table 2.3. Effective properties of orthotropic pentamode microstructures

	a	b	c	d	e	f	g	h
C_{11}	5.677	7.323	38.291	92.337	77.083	11.046	27.313	90.835
C_{22}	22.709	29.291	86.156	10.260	34.259	99.413	109.253	10.093
C_{33}	51.096	65.905	9.573	41.039	8.565	44.183	6.828	40.371
C_{12}	11.355	14.646	57.437	30.779	51.389	33.138	54.626	30.278
C_{13}	17.032	21.968	19.146	61.558	25.694	22.092	13.657	60.556
C_{23}	34.064	43.937	28.719	20.519	17.130	66.275	27.313	20.185
C_{44}	3.29e-5	3.29e-5	4.39e-5	3.37e-5	4.39e-5	3.48e-5	3.37e-5	3.44e-5
C_{55}	4.28e-5	4.66e-5	3.37e-5	3.37e-5	4.66e-5	3.61e-5	3.59e-5	3.43e-5
C_{66}	3.03e-5	3.37e-5	3.29e-5	4.39e-5	3.64e-5	4.98e-5	3.67e-5	3.20e-5
$\lambda_{\max\_1}$	79.482	102.519	134.020	143.635	119.907	154.642	143.394	141.298
$\lambda_{\max\_2}$	8.97e-5	8.13e-5	8.63e-5	8.83e-5	8.20e-5	7.80e-5	8.84e-5	8.08e-5
λ_{R}	8.86e5	1.26e6	1.55e6	1.63e6	1.46e6	1.98e6	1.62e6	1.75e6

The loads and boundary conditions are given in Figure 2.11. The blue cube represents the bounding box of the lattice structure assembled by $6 \times 6 \times 6$ periodic microstructures, measuring 6 mm on one side. For each pair of the opposite faces, the equal magnitude but opposite pressure is uniformly applied. The magnitudes of the resultant forces along each axis are F_x, F_y and F_z. Due to the symmetry, only one-eighth of the model (i.e., $3 \times 3 \times 3$ microstructures) is used in finite element analyses with symmetric boundary conditions. We name the structure assembled by transverse isotropic lattices as the lattice I and the structure assembled by orthotropic lattices as the lattice II. For all the lattice structures, the diameters of uniform cylinder bars are 0.02mm. These structures are meshed with linear solid elements, and the global element seed size is 0.004mm. The Young's modulus of the constituent material Ti6Al4V is 1.138e5 MPa, and the Poisson's ratio is 0.342.

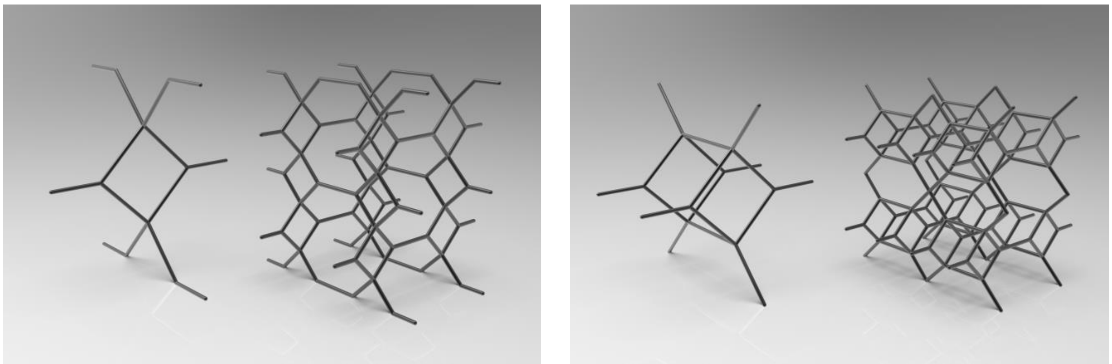

a) Iso-a b) Iso-b

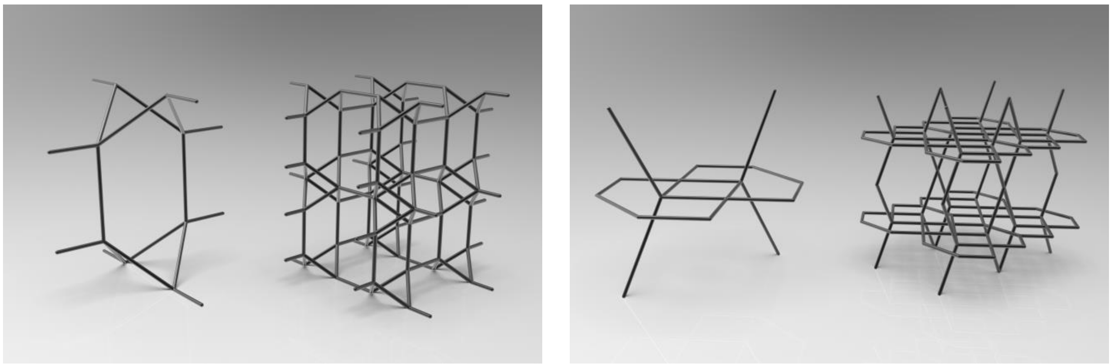

c) Iso-c d) Iso-d

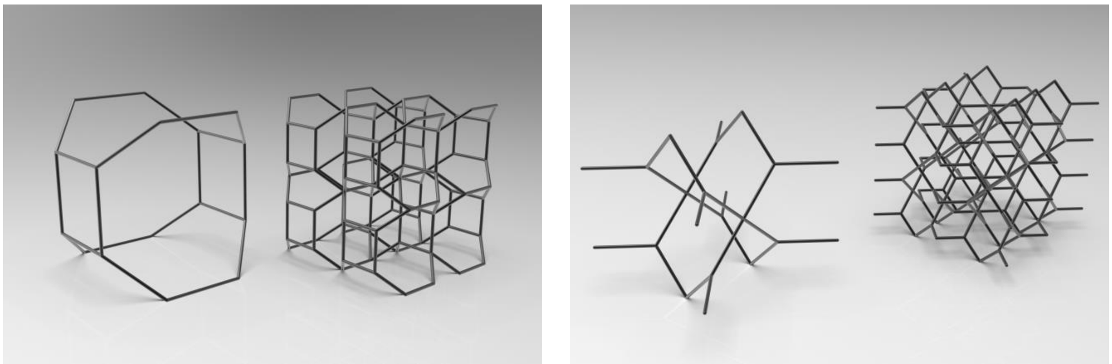

e) Iso-e f) Iso-f

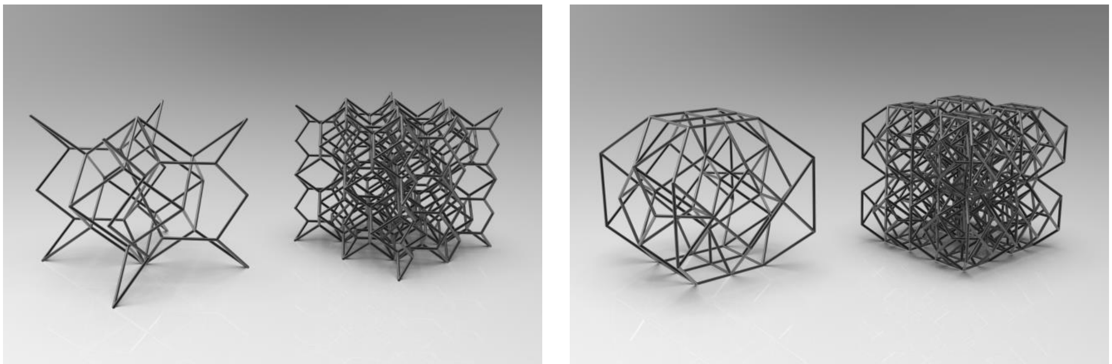

g) Iso-g h) Iso-h

Figure 2.8. Isotropic pentamode microstructures (Note: rendered effect)

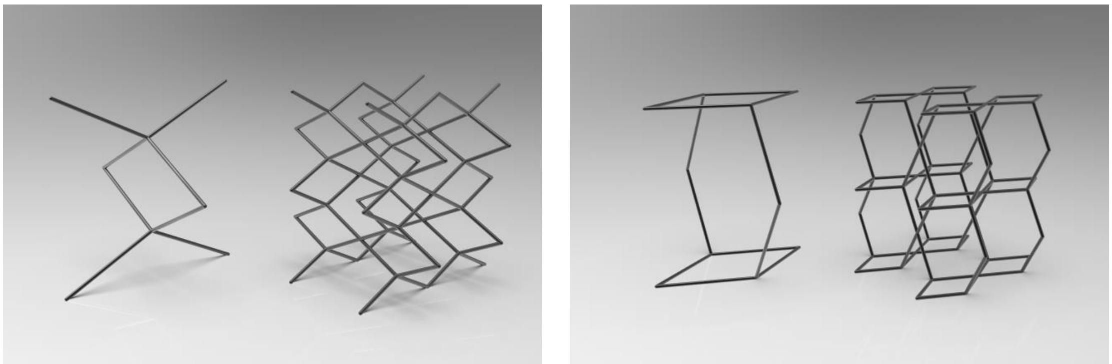

a) Trans-a

b) Trans-b

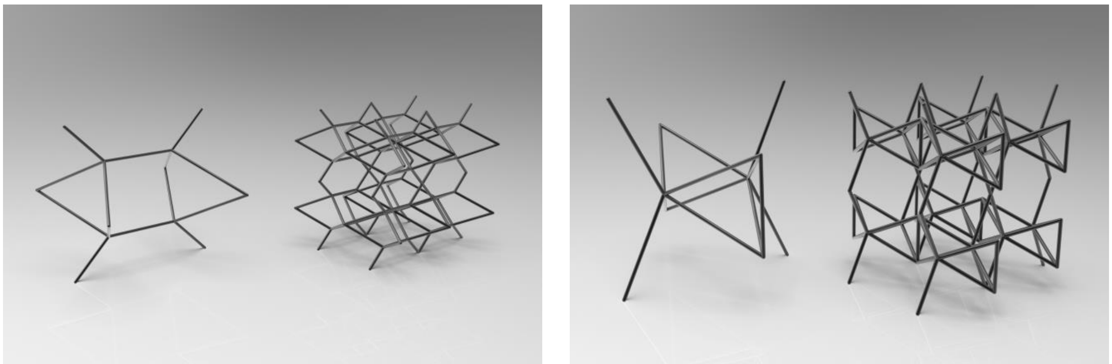

c) Trans-c

d) Trans-d

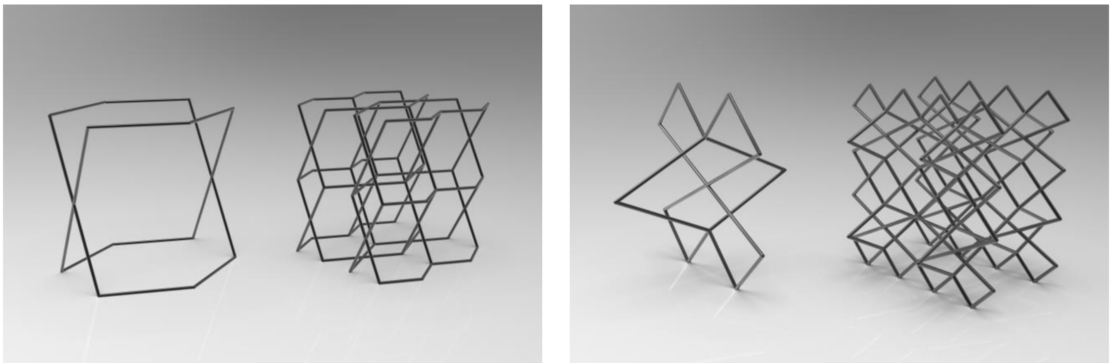

e) Trans-e

f) Trans-f

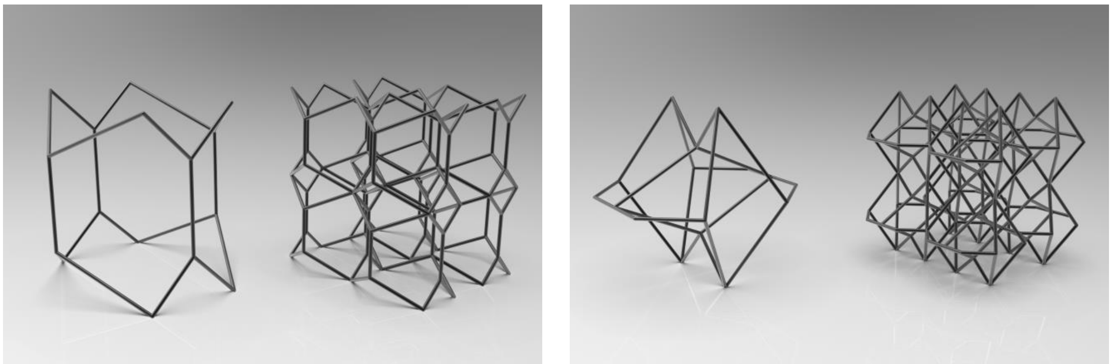

g) Trans-g

h) Trans-h

Figure 2.9. Transverse isotropic pentamode microstructures (Note: rendered effect)

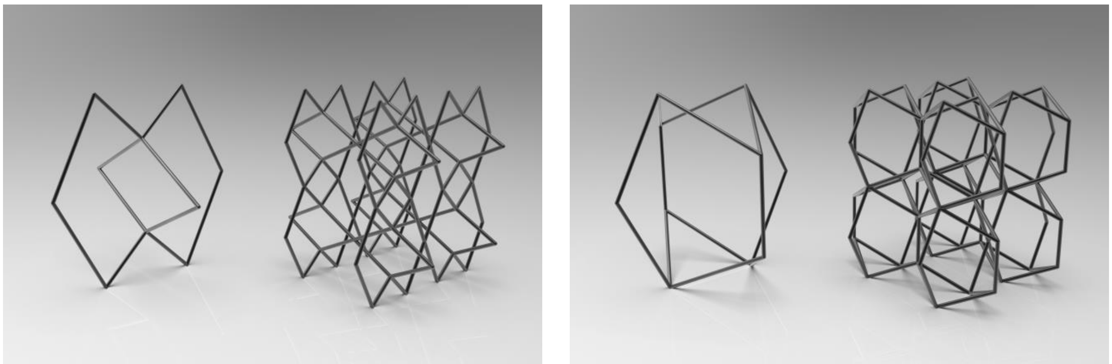

a) Ortho-a b) Ortho-b

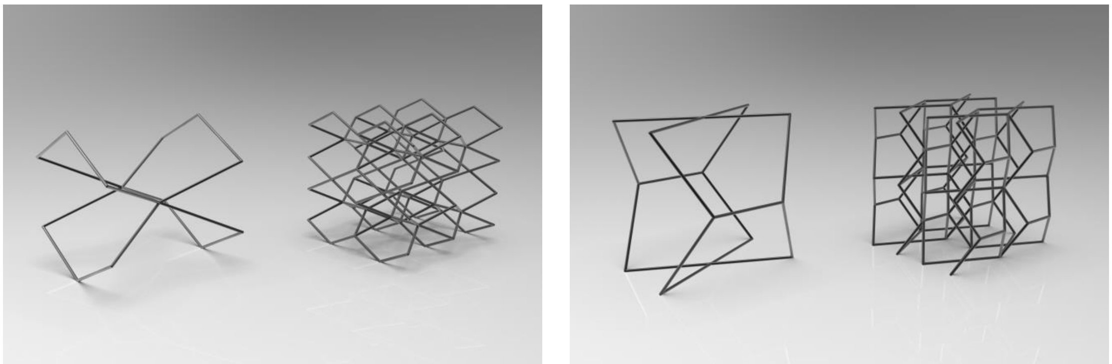

c) Ortho-c d) Ortho-d

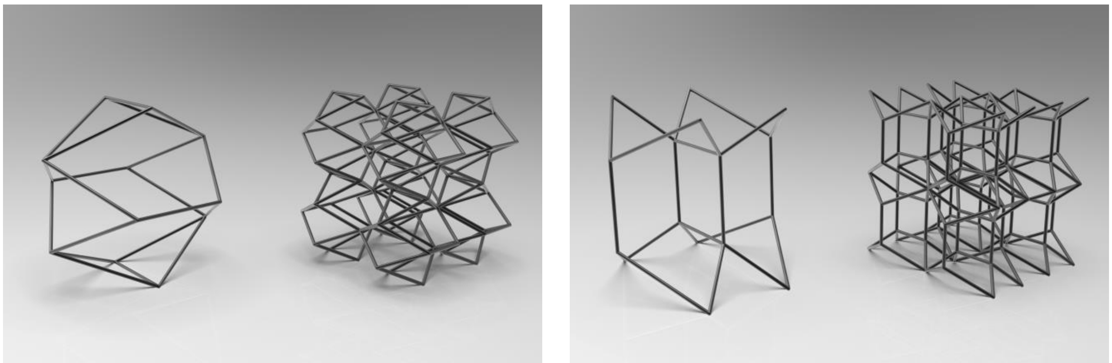

e) Ortho-e f) Ortho-f

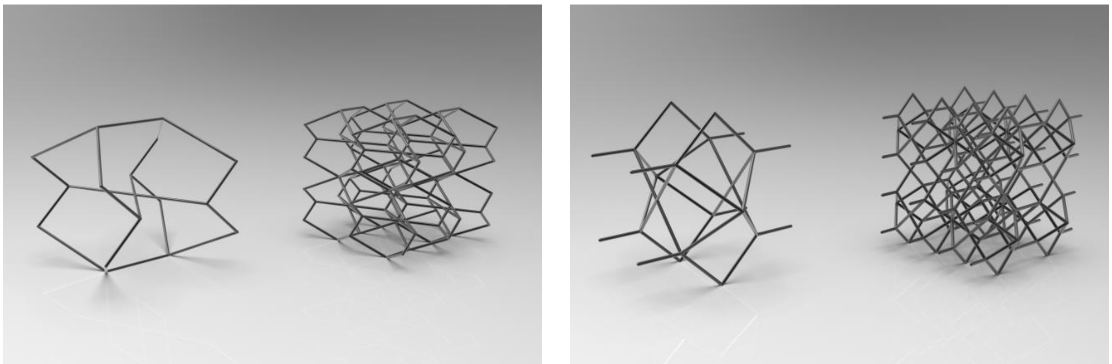

g) Ortho-g h) Ortho-h

Figure 2.10. Orthotropic pentamode microstructures (Note: rendered effect)

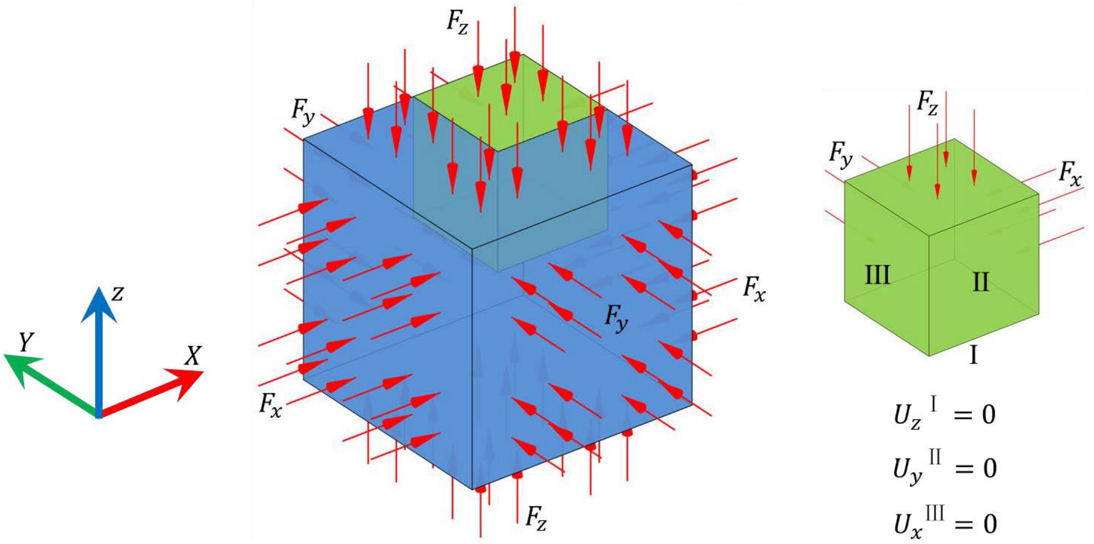

Figure 2.11. Loads and boundary conditions

Six typical load cases applied to each lattice structure are listed in Table 2.4. The fifth and sixth cases are respectively proportional to the bearable load cases of the transverse isotropic and orthotropic lattice structures. For all these load cases, the vector sum of three forces is the same as 1.73205e-2 N.

Table 2.4. Load cases for the lattices

	Case 1	Case 2	Case 3	Case 4	Case 5	Case 6
F_x / N	1.73205e-2	0	0	1.0e-2	1.15473e-2	4.62887e-3
F_y / N	0	1.73205e-2	0	1.0e-2	1.15474e-2	9.24945e-3
F_z / N	0	0	1.73205e-2	1.0e-2	5.77213e-3	1.38932e-2

The results of linear static finite element analyses using ABAQUS are given below. From Figure 2.12 and Table 2.5, we can find that for the lattice I, both the displacement magnitude and the total strain energy in the fifth load case are the smallest. From Figure 2.13 and Table 2.5, we can also find that for the lattice II, both the displacement magnitude and the total strain energy in the sixth load case are the smallest. We emphasize that the total strain energy ratios of the bearable load case to other load cases are considerably small. In one word, a lattice structure assembled by non-isotropic pentamode microstructures is much stiffer when subjected to its bearable load case.

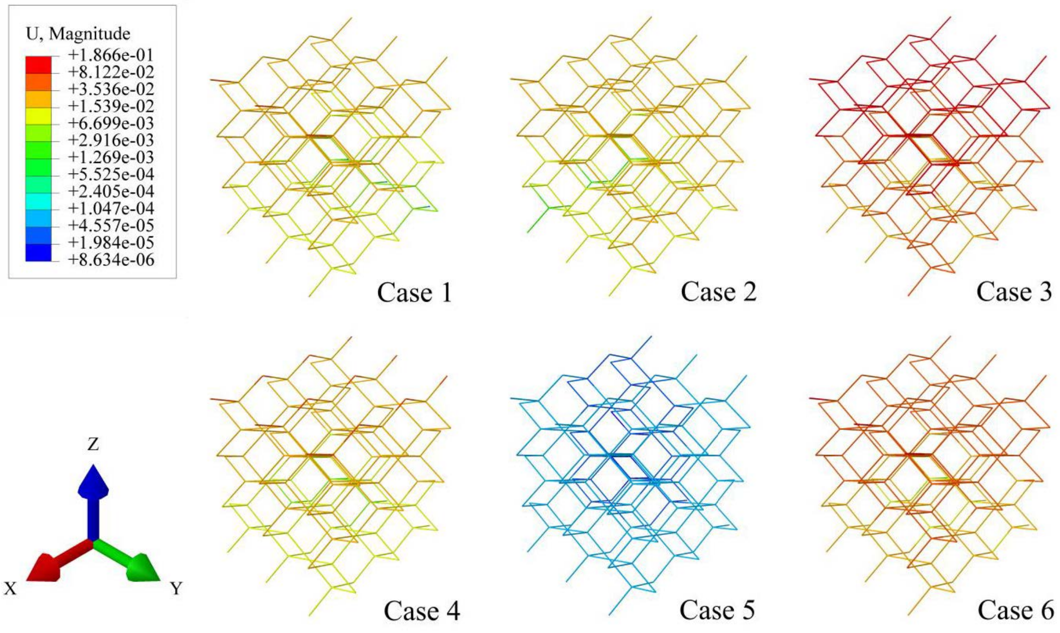

Figure 2.12. Displacement results of the lattice I (Unit: mm)

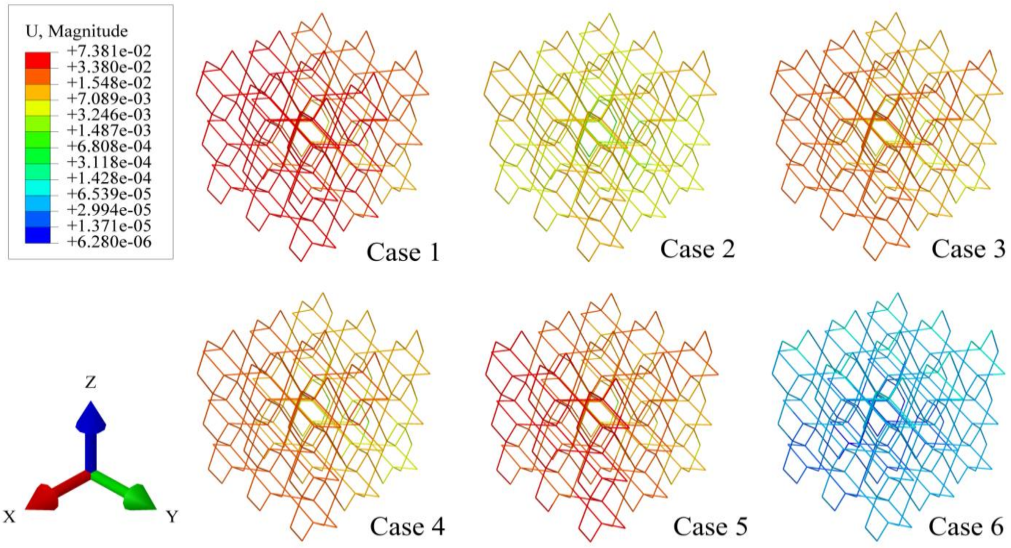

Figure 2.13. Displacement results of the lattice II (Unit: mm)

Table 2.5. Total strain energy in different load cases (Unit: mJ)

Lattice	Case 1	Case 2	Case 3	Case 4	Case 5	Case 6
I	1.51e-4	1.34e-4	1.14e-3	9.61e-5	8.77e-7	4.25e-4
II	5.82e-4	4.80e-5	1.18e-4	9.93e-5	2.25e-4	6.36e-7

2.4.3. Comparative analysis

Here, we will take the novel isotropic pentamode microstructure Iso-f as an example to compare the static mechanical performance with the conventional diamond-type isotropic pentamode microstructure. Like the models in Section 2.4.2, each lattice structure in finite element analyses consists of $3 \times 3 \times 3$ periodic microstructures, and symmetric boundary conditions are applied. The values of F_x, F_y and F_z are all set to 0.01 N. We name the lattice structure assembled by the novel isotropic pentamode microstructure as the lattice III, and the lattice structure assembled by the diamond-type microstructure as the lattice IV. For the lattice III, the diameters of uniform cylinder bars are 0.02mm. For the lattice IV, the diameters of double-cone bars are $d = 0.02\ \mathrm{mm}$ and $D = 0.0241\ \mathrm{mm}$. These two lattice structures have the same material volume (0.071 mm^3). The mesh information and constituent material properties are the same as models given in Section 2.4.2.

The linear static analysis results are given in Figure 2.14 and Figure 2.15. For the lattice III, over 90% of the von Mises stresses of Gauss integration points are between 1.2 MPa and 1.3 MPa, and the ratio of the maximum value to the minimum value is not over 4. The stress distribution in the lattice III is relatively uniform. However, the lattice IV suffers from the stress concentration. The maximum von Mises stress of the lattice IV

(146.633 MPa) is much higher than that of the lattice III (2.135 MPa).

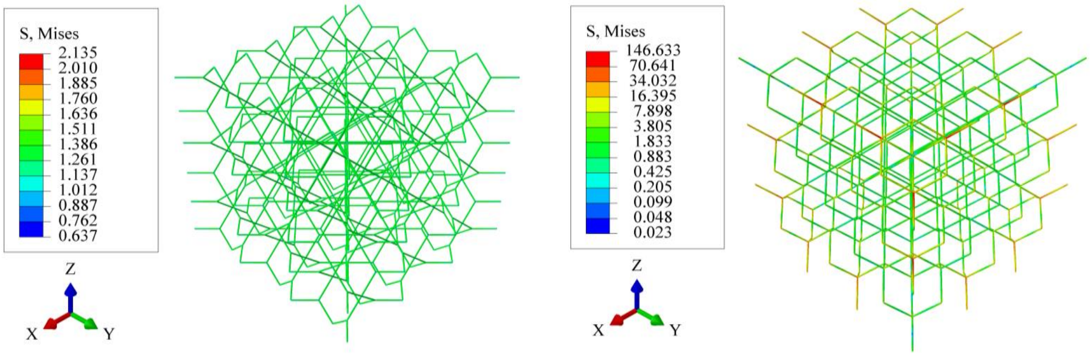

a) Lattice III b) Lattice IV

Figure 2.14. Stress results of the lattices (Unit: MPa):

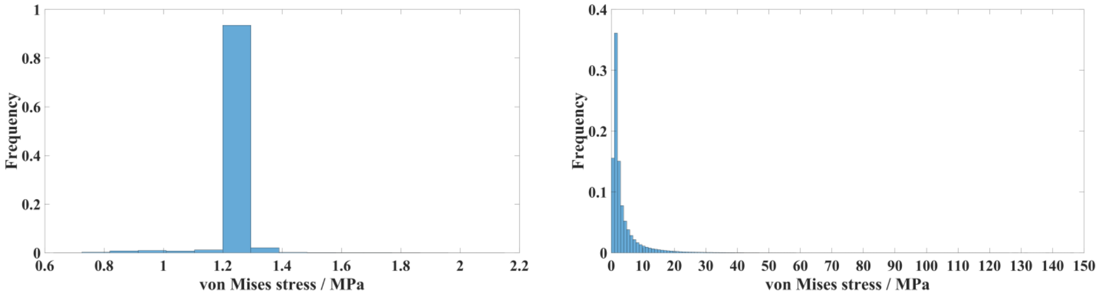

a) Lattice III b) Lattice IV

Figure 2.15. Frequency distribution histograms of stress results

The linear buckling analysis results are given in Figure 2.16. The lowest buckling load of the lattice III (F_x=F_y=F_z= 0.253 N) is slightly higher than that of the lattice IV (F_x=F_y=F_z= 0.241 N). We can see that the first buckling modes of the two lattices all show overall buckling. From the concept of linear static analysis, we can know that when the load is close to F_x=F_y=F_z= 0.253 N, the maximum von Mises stress of the lattice III is only 54 MPa. However, for the lattice IV, even when the load is two-thirds of its lowest buckling load (i.e., F_x=F_y=F_z= 0.1607 N), the maximum von Mises stress theoretically reaches about 2356 MPa and already exceeds the ultimate bearing strength

(1860 MPa) of the constituent material Ti6Al4V. Therefore, no matter the strength or buckling, the lattice III can bear much higher hydrostatic stress than the lattice IV.

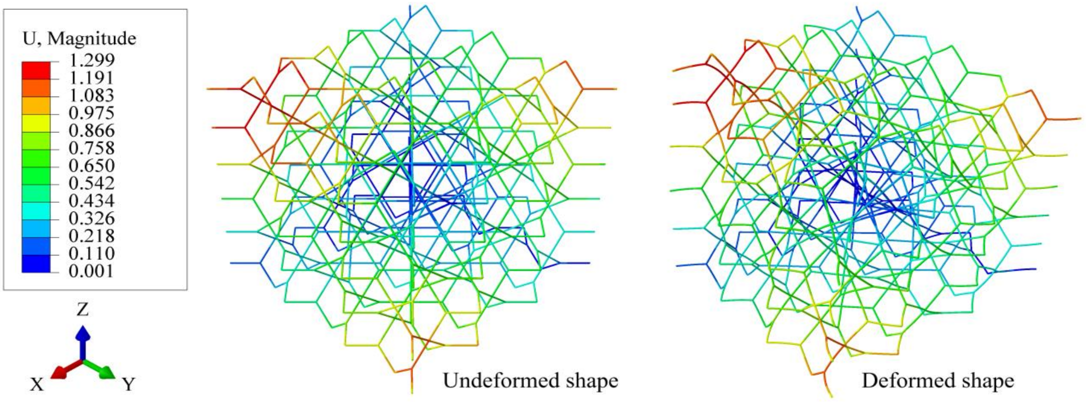

a) Lattice III

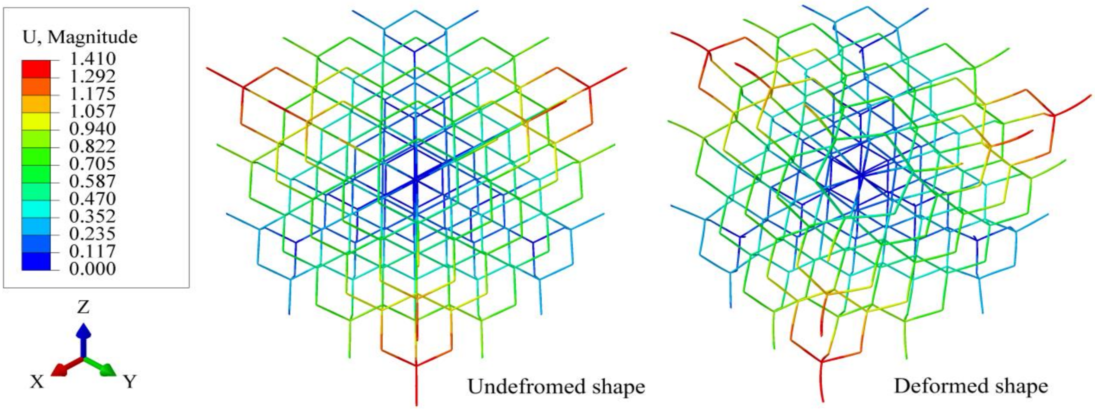

b) Lattice IV

Figure 2.16. First buckling modes of the lattices

2.4.4. Pentamode microstructures with different relative densities

The proposed design method in this work gives a topologically optimal layout of the solid bars in the space. Based on the optimized skeleton, pentamode microstructures with different relative densities can be obtained by changing the geometric dimensions and shapes of the bars. For example, we can introduce the double-cone bars in [130] to replace the uniform cross-section bars, and then change the mid-span diameters D to obtain different relative densities. We emphasize here that other types of structural members rather than double-cone bars can be used to form the pentamode microstructures based on the topologically optimized layout.

Take the optimized skeleton shown in Figure 2.8f as the example. For the microstructure in Figure 2.17a, the diameter of uniform cylinder bars is 0.02mm. Based on the same skeleton, a pentamode microstructure using double-cone bars is generated as shown in Figure 2.17b, of which the diameters are $d = 0.02\ \mathrm{mm}$ and $D = 0.06\ \mathrm{mm}$. The mesh setting and constituent material properties are the same as models in Section 2.4.2.

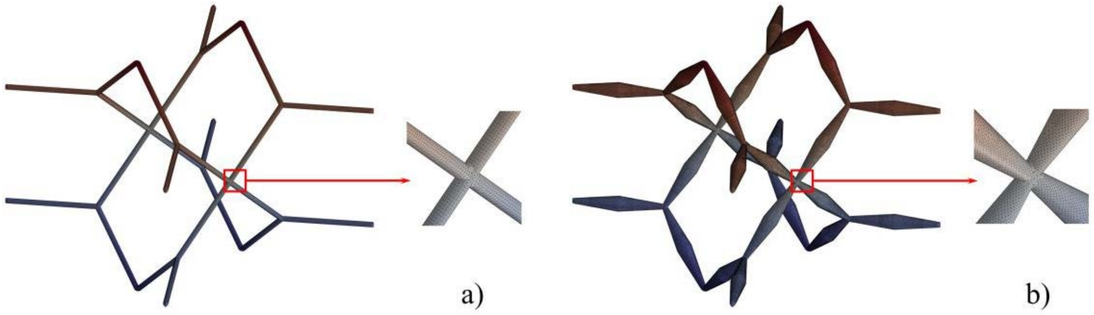

Figure 2.17. Mesh models of pentamode microstructures using solid elements: a) Lower relative density; b) Higher relative density

Their effective elastic stiffness matrices, eigenvalue ratios and relative densities ρ_{R} are listed in Table 2.6, as below. The unit of elastic constants is MPa. We can find that all eigenvalue ratios are relatively large enough to consider these two microstructures to be pentamode, while they are based on the same skeleton but have different relative densities (0.256% and 1.143%). It is noted that the homogenized shear moduli of the solid structures do not approach to zero, but they are still relatively small enough to allow reasonable pentamode properties.

A pentamode lattice (Figure 2.18) with $2 \times 2 \times 2$ microstructures as given in Figure 2.17b is prototyped using a digital light processing 3D printer (Octave Light R1) with a rubber-like material (TangoGray FLX950), as shown in Figure 2.19.

Table 2.6. Effective properties of two pentamode microstructures using solid elements

	a	b
C_{11}	33.969	108.438
C_{22}	33.970	108.453
C_{33}	33.970	108.453
C_{12}	33.795	107.649
C_{13}	33.795	107.648
C_{23}	33.796	107.656
C_{44}	0.091	0.420
C_{55}	0.091	0.420
C_{66}	0.091	0.420
$\lambda_{\max\_1}$	101.561	323.750
$\lambda_{\max\_2}$	0.175	0.797
λ_{R}	581.864	406.004
ρ_{R} (%)	0.256	1.143

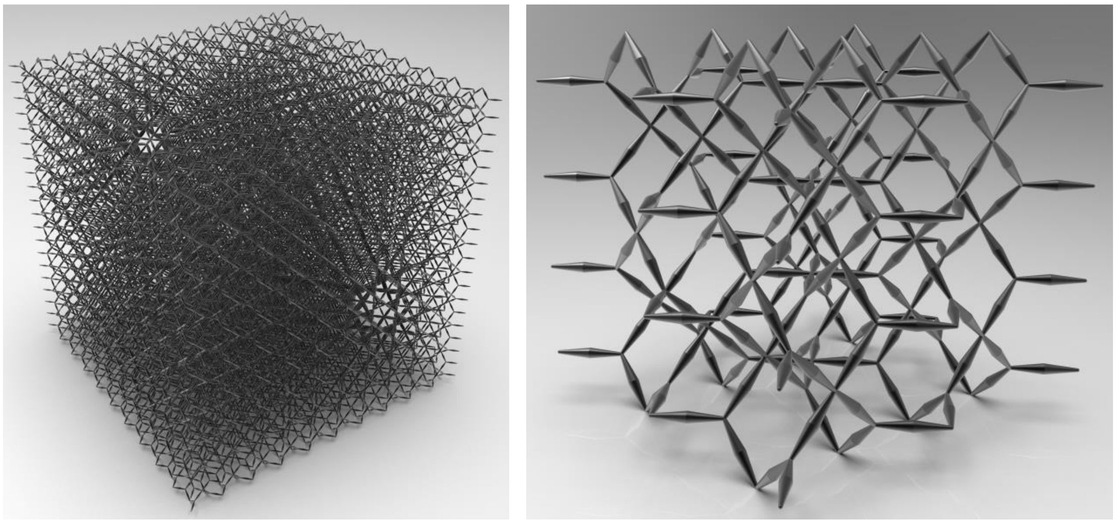

a) $10 \times 10 \times 10$ b) $2 \times 2 \times 2$

Figure 2.18. Periodic arrays of the pentamode microstructures (Note: rendered effect)

A pentamode lattice (Figure 2.18) with $2 \times 2 \times 2$ microstructures as given in Figure 2.17b is prototyped using a digital light processing 3D printer (Octave Light R1) with a rubber-like material (TangoGray FLX950), as shown in Figure 2.19.

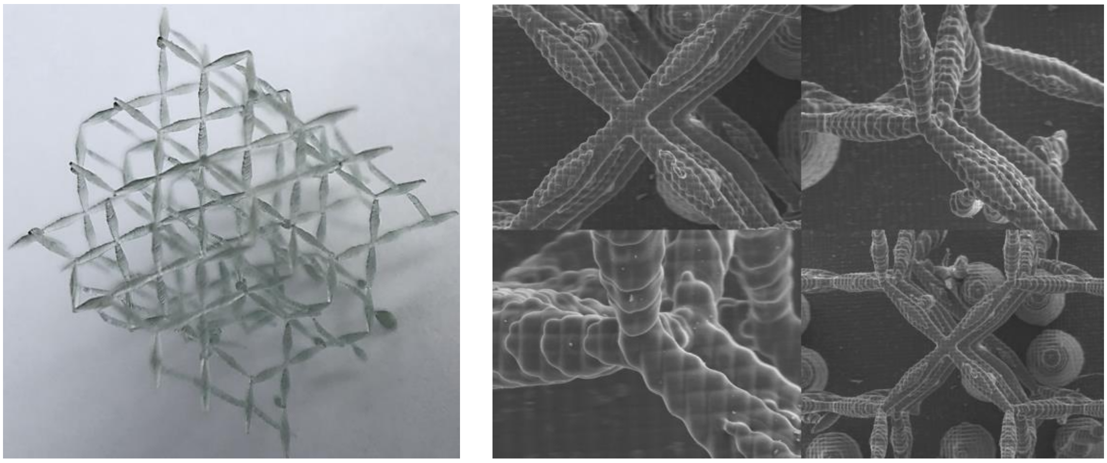
a) b)

Figure 2.19. An additively manufactured specimen with $2 \times 2 \times 2$ microstructures: a) Additively manufactured specimen; b) Microscopic photo

2.5. Conclusion

This work has derived the necessary and sufficient condition required for elastic constants of pentamode metamaterials with at least orthotropic symmetry. We found that a large ratio of the bulk modulus to the shear modulus is no more a sufficient condition for non-isotropic pentamode metamaterials. A ground structure method with the genetic algorithm is then proposed to conduct topology optimization of pentamode metamaterials with at least orthotropic symmetry. Geometric constraints on intersection and overlap of bars are considered in topology optimization with a new efficient detection method to obtain realistic designs. Twenty-four novel pentamode microstructures without intersection or overlap of bars are found, including isotropic, transverse isotropic and orthotropic ones. The optimization results have demonstrated the effectiveness and efficiency of the proposed design method. The further analyses have verified that lattice structures assembled by non-isotropic pentamode microstructures are much stiffer when subjected to their bearable load cases. From the comparative analysis results, we can see that one isotropic pentamode microstructure obtained by topology optimization can form lattice structures to bear much higher hydrostatic stress than the conventional diamond-type pentamode microstructure. Moreover, we proposed that based on the optimized strut skeleton, pentamode microstructures with different relative densities can be easily obtained just by changing the geometric dimensions and shapes of the bars.

Chapter 3 Design of Metamaterials with Ideal Elastic Isotropy and Extreme Negative Poisson's Ratio

3.1. Introduction

This chapter is a modified version of the journal paper titled "Three-dimensional metamaterials exhibiting extreme isotropy and negative Poisson's ratio", which was published in *International Journal of Mechanical Sciences* (Volume 259, 108617).

Mechanical metamaterials have recently sparked a surge of interest due to their potentials for diverse applications. However, simultaneously accomplishing multiple extreme elastic properties remains a challenge [14, 158]. Within the various kinds of mechanical metamaterials, auxetics, a class of materials with negative Poisson's ratio (NPR), have been widely studied for their enhanced mechanical properties and novel applications [159-164]. However, in accordance with the current state of the art, auxetic metamaterials with simultaneous presence of ideal isotropy [165, 166] and extreme negative Poisson's ratio can be hardly found, which are actually a special type of unimode metamaterials. Hence, the aim of this chapter is the rational design of such a metamaterial with one zero eigenvalue of its elastic stiffness matrix, which is in contrast to pentamode metamaterials studied in Chapter 2.

Isotropy in materials is a quality that defines the uniformity of its properties in all orientations. Isotropy is an important property for applications where consistent behavior of materials in different directions is required. This property ensures that the material's characteristics remain uniform regardless of the direction in which they are measured. For example, isotropic materials are often used in structures when there is a necessity to withstand forces from all directions without exhibiting preferential behavior. However, the fact that a raw material is isotropic does not imply that a resulting lattice made from this material maintain this quality, due to factors like differences in design and manufacturing of the lattice. These factors can result in variations of effective mechanical properties of lattices along different directions. Therefore, when designing metamaterials, it is essential to have control over the isotropy of the lattices to ensure even stress distribution, deformation, or failure of the lattices. For example, in mechanical and aerospace engineering, a lattice structural component needs to have uniform mechanical properties (e.g., strength, stiffness, and fatigue) in all directions to withstand the loads and stresses that they will be subjected to. Hence, how to design lattice metamaterials to gain ideal isotropy is crucial to ensure the reliability, durability, and safety of the mechanical products constructed by using lattice structures.

Poisson's ratio is defined as a negative ratio of the transverse strain to the axial strain when the material is under a uniaxial loading. It is a fundamental material property that is independent of the material's size or scale, so it can be studied and compared across different length scales. This is important for understanding the behavior of auxetic metamaterials and their potential applications in various fields. Compared to materials with positive Poisson's ratios, auxetic metamaterials exhibit a transverse expansion when stretched uniaxially while a transverse contraction when compressed uniaxially, which is illustrated in Figure 3.1. Auxetic metamaterials possess superior mechanical properties such as synclastic curvature, indentation resistance, energy dissipation, negative compressibility, vibration transmission, and acoustic absorption. These exceptional properties give auxetic metamaterials a diversity of potential applications in aerospace, automotive, biomedical, and mechanical engineering. Since the development of the first man-made auxetic foam by Lakes [167], a variety of auxetic metamaterials have been developed, including re-entrant [168-170], chiral [171, 172], rotating units [173], and perforated sheets [174]. According to the elasticity theory, the allowable range of Poisson’s ratios for 3D isotropic materials is from -1 to 0.5 [175]. For anisotropic materials, arbitrary large positive and negative Poisson’s ratios can occur along specific directions [176]. If an isotropic material has a Poisson’s ratio at its theoretical lower limit of -1, it corresponds to an isotropic unimode material with an infinite ratio of shear modulus to bulk modulus [128], meaning that it is hard to shear but easy to uniformly deform volumetrically, which makes them suitable for electronic flexible screens. This contrasts with isotropic pentamode metamaterials, which have Poisson’s ratios at the theoretical upper bound [130].

An isotropic 3D structure possessing a Poisson’s ratio -1 was firstly proposed by Almgren [177]. However, it consists of sliding collars and springs. It is more a macroscopic mechanism than a continuum microstructure. Later, Milton [178] proposed two families of 2D isotropic composite materials that exhibit Poisson’s ratios approaching -1. However, their Poisson’s ratios can be close to -1 only when their

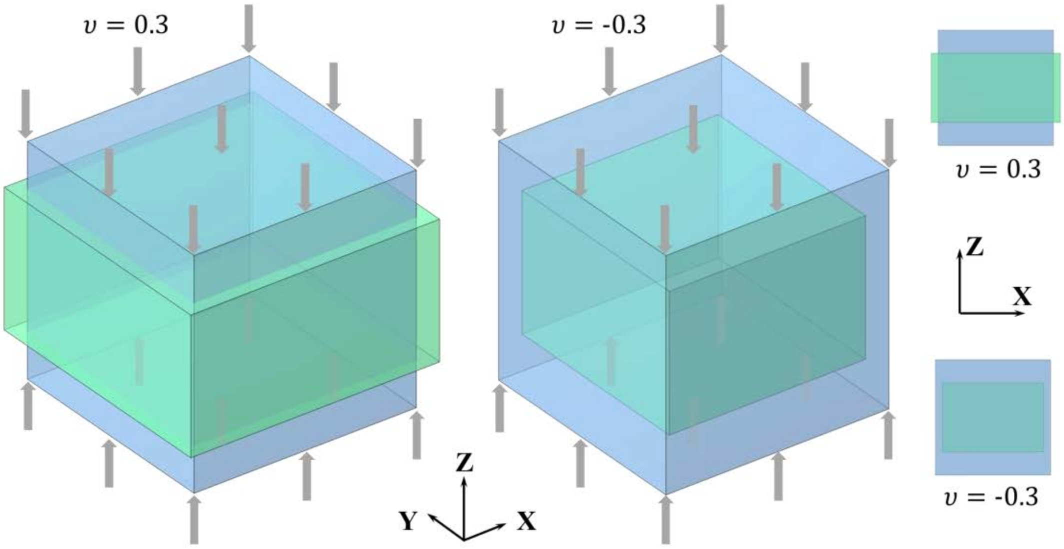

Figure 3.1. Deformation behaviors of materials with different Poisson's ratios. Grey arrows represent uniaxial compression loads. Blue cuboids represent original and undeformed structures. Green cuboids represent the deformed shapes of structures.

stiffness ratio of the compliant matrix to the stiff inclusion is nearly zero, and the second family is a laminate with three widely separated length scales [179]. A 2D honeycomb with a Poisson's ratio -1 was proposed by Prall and Lakes [171], which is directionally isotropic but has a chiral anisotropy. A 2D isotropic microstructure with a Poisson's ratio -1 was proposed by Grima and Evans [173], which contains rotating rigid units. Several non-isotropic unimode metamaterials have been proposed also based on rigid units and pivots [179, 180], and one of them exhibits only positive Poisson's ratios [180]. Bückmann et al. [181] proposed a 3D unit cell that has a Poisson's ratio -0.932 along the principal axis and a Zener ratio 1.145 when its connection size is 0.25%. A 3D auxetic cellular structure proposed in 2017 claims a Poisson's ratio approaching -1 [182], but it is not isotropic and exhibits Poisson's ratios -1 only in three principal directions, which was later demonstrated by Wang et al [183]. As mentioned above, a directional Poisson’s ratio -1 is not a limit or special value for non-isotropic materials. A 2D structure with random networks was claimed to possess ideal isotropy and a Poisson’s ratio -0.98, but its Poisson’s ratio along the principal axis is only -0.88 [184].

While empirical design motifs have been successful in creating several 3D auxetic metamaterials, they may not necessarily lead to optimal or multifunctional properties. Numerical design optimization methods can help to explore a larger design space and identify previously unknown metamaterial architectures with desirable properties, allowing for tailored and optimized metamaterials with specific multifunctionalities. Topology optimization has been applied successfully in designing auxetic metamaterials [185-195], allowing for the creation of new material architectures, while most of the designs have either 2D microstructures [186-192] or 3D non-isotropic microstructures [193-195]. For these non-isotropic microstructures [188-195], their negative Poisson’s ratios are only exhibited in specific orientations, limiting their potential for applications requiring isotropic behavior.

In this work, a new design method based on topology optimization is developed for finding 3D novel microstructures that can simultaneously achieve ideal elastic isotropy and extreme negative Poisson’s ratio. The proposed approach is intended to be more generic and generative, allowing for the discovery of new metamaterial architectures with customized multifunctional properties.

3.2. Computational design method

In this section, we firstly introduce our proposed method for topology optimization, which involves using a 3D strut-based ground structure with geometric cubic symmetry. Then we discuss the mechanical characteristics of isotropic materials with extreme negative Poisson’s ratios. This is important because the optimization process is to find a microstructure that meets certain design criteria for desired mechanical properties. Finally, we establish a mathematical optimization formulation for designing microstructures with ideal isotropy and specific Poisson's ratio.

3.2.1 Ground structure with geometric cubic symmetry

The design method developed in this work is based on the ground structure method for discrete topology optimization. In the case of discrete topology optimization methods, the optimized designs directly consist of struts, which allow for easier manufacturing and can generate ultralight structures with less computational cost. Moreover, strut-based microstructures with cross-sectional parameters obtained by using discrete topology optimization methods can be easily tuned to achieve a range of different effective material properties.

This method involves the use of a prescribed ground structure that includes both active and inactive bars to describe potential topologies of designs. The active bars are those that compose the optimized structure, while the inactive bars would be removed from the final design. The optimization is then a numerical iterative process to determine which bars should be active and which should be inactive to achieve the desired mechanical properties. Here, we defined a strut-based ground structure with the geometric cubic symmetry. First, a number of grid points are uniformly distributed within a cubic design domain, which have equal distances and are aligned with three coordinate axes. It is worthy of note that the number of points along each axis is an odd number. An increasing number of grid points would lead to not only better ability in topological description potentially for creating more different designs, but also an increased number of design variables and therefore higher computational cost. In this chapter, we use a 5×5×5 grid of points as given in Figure 3.2a for the numerical examples.

The cubic design domain is split into 48 subdomains with the same geometry using nine symmetric planes, and one of them is selected and considered to be the primary one, which is illustrated in Figure 3.2b. Connecting every two points in the primary subdomain by a strut would generate a fully connected ground structure, as displayed in Figure 3.2c. However, overlapping bars will exist in such a ground structure, which will not enhance its topological description ability but increase the number of its design variables. Hence, an iterative process will be used to detect and remove these overlapping bars. The iterative process ensures that the ground structure is free of overlapping bars while still preserving its topological description ability. By removing overlapping bars, we can also simplify the ground structure to have less design variables, making the optimization more efficient.

Based on such a ground structure free of overlapping bars (Figure 3.2d), we can then assemble a whole ground structure for the cubic design domain using mirror operations, as shown in Figure 3.2f. Duplicated bars on shared faces between subdomains should be merged. It should be noted that the bars of the primary subdomain are classified into five groups as given in Figure 3.2d. As presented in Figure 3.2e, for each bar in different groups, it has different number of mapping bars in the whole design domain.

In the proposed design method, active and inactive bars are distinguished to represent different designs using the same ground structure. Active bars are bars that can significantly carry loads, while inactive bars have ignorable influence on the overall structural stiffness and can be removed from the final design. Additionally, active bars can have different cross-sectional shapes and sizes, which allows for more flexibility in designing microstructures. In this chapter, we define all bars in the ground structure with circular sections, and all inactive bars have the same cross-sectional radius 1e-5 when the cubic design domain's length is 1. If their radii are set to be exactly zero, the total structural stiffness matrix would have singularity problems. Inactive bars can be considered as void space, and their presence has a negligible effect on the homogenized material properties.

Although we can use radii of all bars in the primary subdomain as design variables, a new strategy is proposed here. Assuming that there are m bars in the primary subdomain and what we expect as a final optimized design has at most n bars in the primary subdomain, it is obvious that $n \ll m$. Moreover, we usually expect to find novel microstructures without too much complicated geometries. If $n = 10$, there may be over three hundred bars in the whole design. Therefore, n should be a small integer, e.g., 3, 4, and 5. Therefore, design variables are defined as: n integer variables indicate which bars in the primary subdomain are active, and other n continuous variables are radii of these active bars. Such definitions can give the following advantages: First, compared with conventional ground structure methods using radii of all bars as design variables [30], the proposed method has a much smaller number of design variables. Second, compared with the ground structure method that only define active and inactive bars in Chapter 2, the proposed method can describe a design that consists of active bars with a range of cross-sections, which enhances its structural description for geometries and tunability for properties. However, the gradient-based optimization solvers cannot be adopted since there are both integer and continuous variables in the design.

Moreover, we usually expect to find novel microstructures without too much complicated geometries. If $n = 10$, there may be over three hundred bars in the whole design. Therefore, n should be a small integer, e.g., 3, 4, and 5. Therefore, design variables are defined as: n integer variables indicate which bars in the primary subdomain are active, and other n continuous variables are radii of these active bars. Using such definitions, the number of variables is greatly decreased, and there would no longer be many bars with intermediate radii in final optimized designs.

3.2.2 Extreme Negative Poisson's ratios

Any design described by the proposed ground structure, which has geometric cubic symmetry, will be at least elastically cubic symmetric, meaning that its elastic properties will be identical in three orthogonal principal directions. Then the elastic stiffness matrix must have the following form:

$$\boldsymbol{C}=\begin{bmatrix} C_{11} & C_{12} & C_{12} & 0 & 0 & 0 \\ C_{12} & C_{11} & C_{12} & 0 & 0 & 0 \\ C_{12} & C_{12} & C_{11} & 0 & 0 & 0 \\ 0 & 0 & 0 & C_{44} & 0 & 0 \\ 0 & 0 & 0 & 0 & C_{44} & 0 \\ 0 & 0 & 0 & 0 & 0 & C_{44} \end{bmatrix} \tag{3.1}$$

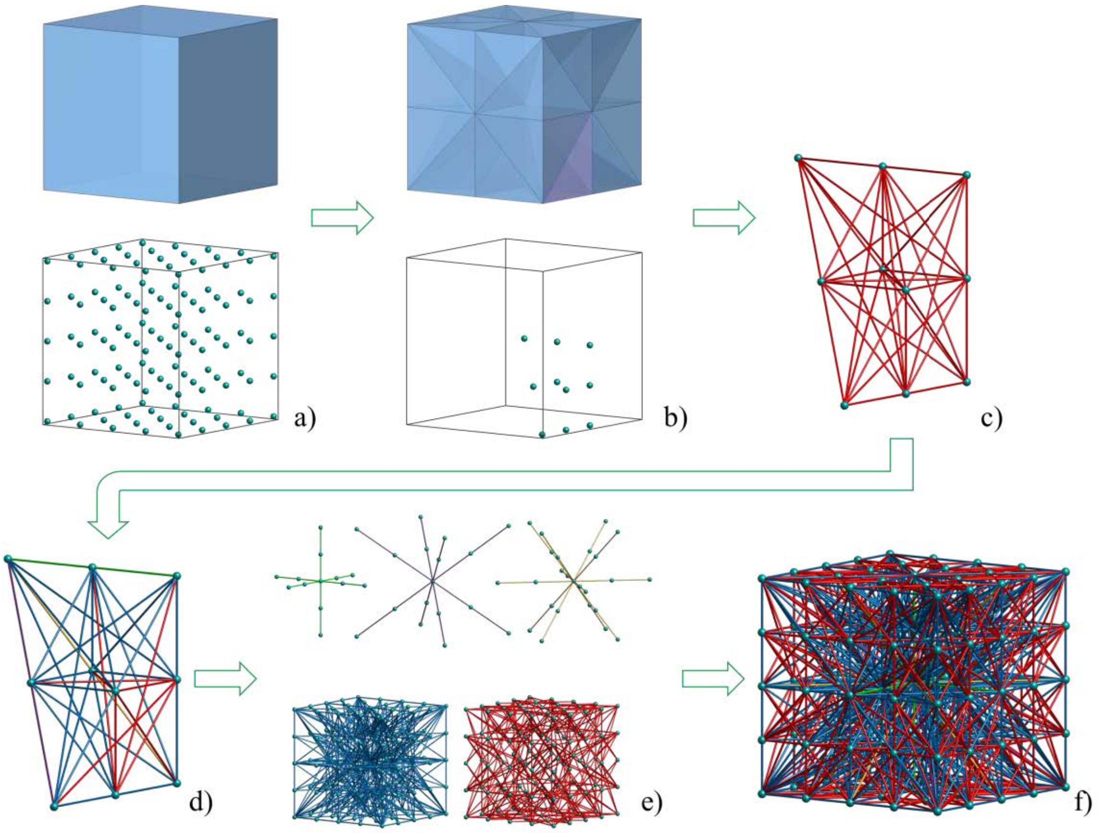

Figure 3.2. Generation of a 3D ground structure with the geometric cubic symmetry. a) Points in the whole design domain; b) Points in the primary subdomain (purple region); c) A fully connected ground structure in the primary subdomain; d) A ground structure in the primary subdomain without overlapping bars and consisting of five groups of bars; e) Five ground structures in the whole design domain respectively assembled by different groups of bars; f) The final ground structure.

The condition required for elastic isotropy of a material is that the elastic constants must satisfy the following equation:

$$\frac{(C_{11} - C_{12})}{2C_{44}} = 1 \tag{3.2}$$

Once this condition is satisfied, the isotropic Poisson's ratio is calculated by:

$$\nu = \frac{C_{12}}{C_{11} + C_{12}} \tag{3.3}$$

Besides, the isotropic Young's modulus (E), bulk modulus (K), and shear modulus (G) are defined using the same two elastic constants as follows:

$$\begin{cases} E = \dfrac{(C_{11} - C_{12})(C_{11} + 2C_{12})}{C_{11} + C_{12}} \\ K = \dfrac{(C_{11} + 2C_{12})}{3} \\ G = \dfrac{(C_{11} - C_{12})}{2} \end{cases} \tag{3.4}$$

When the Poisson's ratio is 0.5, the following elastic properties can be derived from Equation (3.3) and (3.4):

$$\begin{cases} C_{11} = C_{12} > 0 \\ E = 0 \\ K = C_{11} \\ G = 0 \end{cases} \tag{3.5}$$

Such a solid material belongs to pentamode metamaterials, and its stiffness characteristic is an infinite ratio of bulk modulus to shear modulus.

When the Poisson's ratio approaches -1, the following material properties can be derived from Equation (3.3) and (3.4):

$$\begin{cases} C_{11} = -2C_{12} > 0 \\ E = 0 \\ K = 0 \\ G = \dfrac{3}{4}C_{11} \end{cases} \tag{3.6}$$

Such a material belongs to unimode metamaterials, and its stiffness characteristic is an infinite ratio of shear modulus to bulk modulus. Its corresponding elastic stiffness matrix is given in Equation (3.7).

This elastic stiffness matrix has only one zero eigenvalue, and the corresponding eigenvector indicates a hydrostatic stress state. We can find that for any non-zero strain vector applied to this matrix, the corresponding first stress invariant is always zero. It indicates that such a material cannot resist non-zero first stress invariant, which corresponds to the volume change. Therefore, for an ideal isotropic unimode metamaterial, its volume can be easily changed, but its shape can be relatively hard to be changed. It is exactly opposite of isotropic pentamode metamaterials.

$$\boldsymbol{C} = \begin{bmatrix} C_{11} & -\frac{1}{2}C_{11} & -\frac{1}{2}C_{11} & 0 & 0 & 0 \\ -\frac{1}{2}C_{11} & C_{11} & -\frac{1}{2}C_{11} & 0 & 0 & 0 \\ -\frac{1}{2}C_{11} & -\frac{1}{2}C_{11} & C_{11} & 0 & 0 & 0 \\ 0 & 0 & 0 & \frac{3}{4}C_{11} & 0 & 0 \\ 0 & 0 & 0 & 0 & \frac{3}{4}C_{11} & 0 \\ 0 & 0 & 0 & 0 & 0 & \frac{3}{4}C_{11} \end{bmatrix} \tag{3.7}$$

3.2.3 Mathematical optimization formulation

Based on Equation (3.2) and (3.3), for an optimized design to achieve both ideal elastic isotropy and a specific Poisson's ratio ν_{obj}, a necessary and sufficient condition is given by

$$\left(\frac{(C_{11} - C_{12})}{2C_{44}} - 1\right)^2 + \left(\frac{C_{12}}{C_{11} + C_{12}} - \nu_{\mathrm{obj}}\right)^2 = 0 \tag{3.8}$$

Based on this condition, the following optimization formulation is established:

$$\begin{aligned} &\text{Find: } \boldsymbol{\rho} = [\rho_1 \quad \cdots \quad \rho_n \quad \rho_{n+1} \quad \cdots \quad \rho_{2n}] \\ &\text{Min: } f(\boldsymbol{\rho}) = \omega_{iso}\left(\frac{\left({C_{11}}^H(\boldsymbol{\rho}) - {C_{12}}^H(\boldsymbol{\rho})\right)}{2{C_{44}}^H(\boldsymbol{\rho})} - 1\right)^2 + \omega_{pr}\left(\frac{{C_{12}}^H(\boldsymbol{\rho})}{{C_{11}}^H(\boldsymbol{\rho}) + {C_{12}}^H(\boldsymbol{\rho})} - \nu_{\mathrm{obj}}\right)^2 \\ &\qquad + \omega_{geo}\left(N_{ins}(\boldsymbol{\rho}) + N_{isol}(\boldsymbol{\rho})\right) \end{aligned} \tag{3.9}$$

where $\boldsymbol{\rho}$ represents design variables, $\boldsymbol{C}^H$ is the effective elastic stiffness matrix of a candidate design that is calculated by using the computational homogenization method introduced in Section 2.3.2, and ω represents weight factors for each penalty term. The last penalty term functions as geometric constraints on bars. Here, N_{ins} is the quantity of intersecting bar pairs within the ground structure, and N_{isol} is the quantity of isolated geometric parts within the ground structure, which are illustrated in Figure 3.3. Discrete structures with intersecting bars are impractical and unrealistic [154], which should be avoided in the final optimized designs. Besides, a design with isolated geometric parts is not what we expected for lattice structures. For the three weight factors, we use 1, 40, and 0.1 as their values, respectively, based on our numerical experience. We use the genetic algorithm to solve this mixed integer programming problem. In numerical implementations, a built-in function *ga* from the commercial software MATLAB [157] is used as a black-box solver. It should be noted that nonlinear equality constraints cannot be explicitly imposed by the genetic algorithm for optimization problems with integer variables. Therefore, the geometric constraints are added as a penalty term into the objective function.

Here, we emphasize that the developed design approach is generic to be utilized for the discovery of microstructures with wide-ranging Poisson's ratios, including zero and 0.5, in addition to negative values. It can be achieved by assigning different values of ν_{obj} in the objective function. In this chapter, we only focused on optimization design using $\nu_{\text{obj}} = -1$ for finding novel isotropic unimode microstructures. Optimization designs using other ν_{obj} values are beyond the scope of this chapter. Moreover, the proposed design method has no requirement for specific constituent materials. Using the same design method, we can obtain corresponding optimized designs for different constituent materials.

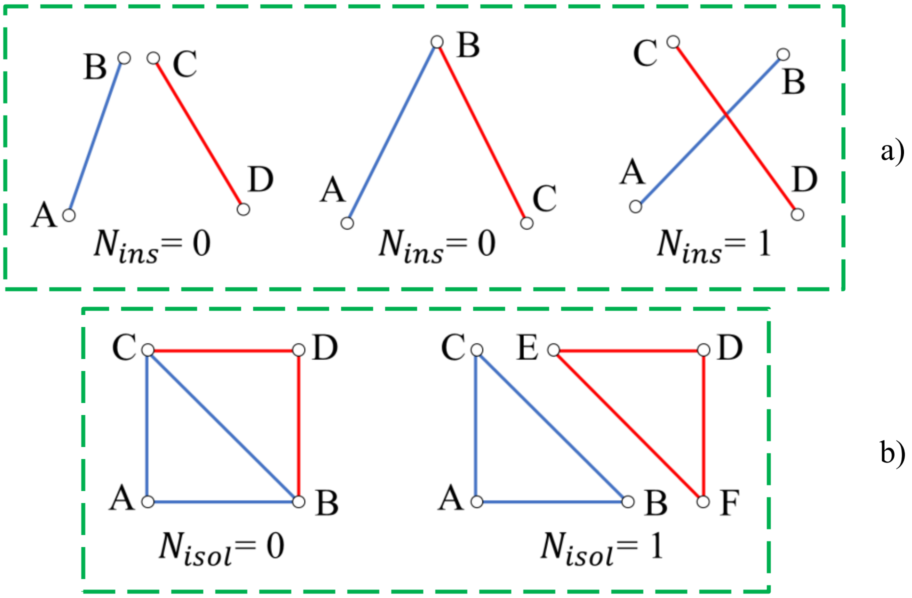

Figure 3.3. Geometric constraints: a) Intersecting bars; b) Isolated geometric parts

3.3. Numerical results

Using the proposed systematic design method, four novel strut-based microstructures have been found, which are three-dimensional, elastically isotropic, and auxetic with Poisson's ratios approaching the theoretical lower limit. As mentioned before, existing 3D isotropic unimode microstructures designed by conventional intuition-based methods, are either constructed with mechanism components [177] or not ideally isotropic [181]. However, the four microstructures proposed below possess ideal isotropy and totally novel geometries without mechanism components, which substantially show the maturity of the developed topology optimization method.

In this section, these microstructures have been introduced in detail by describing their geometries, analyzing their effective material properties, and validating their macroscopic mechanical behaviors.

3.3.1 Novel isotropic auxetic microstructures

Here, we choose a widely used titanium alloy, Ti6Al4V, as an isotropic linear elastic constituent material to be used in topology optimization. As shown in Figure 3.4, four novel auxetic microstructures have been found. These microstructures all have the geometric cubic symmetry and consist of cylindrical struts with different cross-sectional areas. The microstructure I has 50 vertices and 72 struts with three types of radii. The microstructure II has 43 vertices and 84 struts with three types of radii. The microstructure III has 60 vertices and 108 struts with four types of radii. The microstructure IV has 49 vertices and 138 struts with five types of radii.

From the geometric aspect, the microstructure I has the simplest geometry, while the microstructure IV has the most complicated geometry. While for the auxetic mechanism, all these microstructures belong to the re-entrant type. We emphasize that these 3D isotropic unimode microstructures are single-scale, single-phase, and constructed by elastic continua without using sliding collars, springs, rotating frames, or rigid units.

3.3.2 Effective material properties

For these auxetic microstructures, we know their information about coordinates of each vertex, connected vertices of each strut, and ratios between cross-sectional radii of struts. Keeping the ratios between radii unchanged, we can easily customize a series of microstructures across a spectrum of relative densities based on the same strut skeletons. Here, we will numerically investigate about tuning their effective material properties by changing their volume fractions. For microstructures with moderate volume fractions, solid elements are used in finite element analyses to provide more accurate results, because their struts are not slender anymore. Therefore, we use solid elements to conduct the computational homogenization for the series of microstructures with a range of volume fractions. In this work, the commercial software COMSOL Multiphysics was used for conducting numerical analyses for the microstructures with varying volume fractions and the macroscopic lattice structures. For the constituent material Ti6Al4V, its Young's modulus is 113.8 GPa, and its Poisson's ratio is 0.342. The mesh models using solid elements all have over millions of degrees of freedom. For the computational homogenization of microstructures in COMSOL Multiphysics, periodic boundary conditions are imposed by node-to-node constraints.

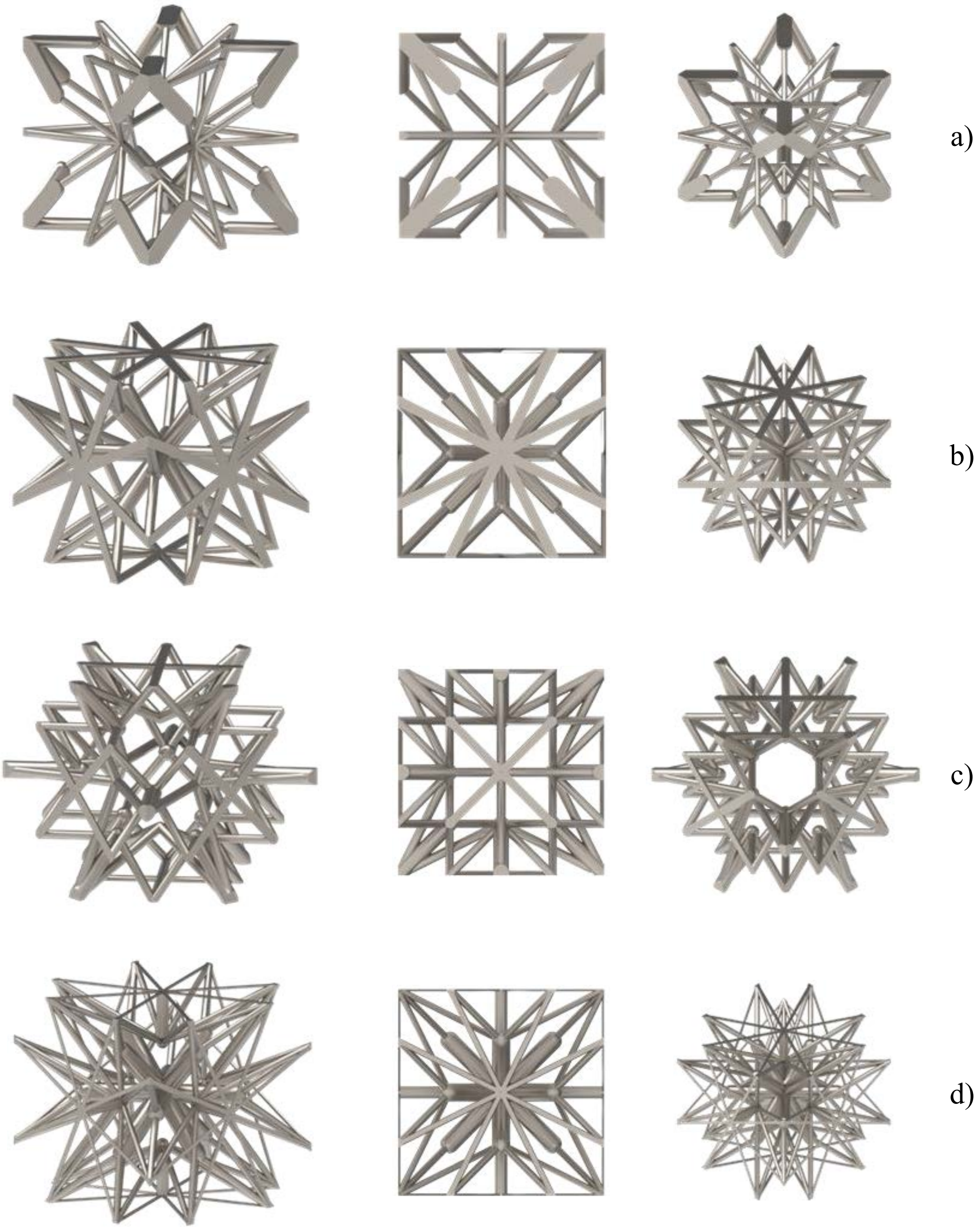

Figure 3.4. Novel isotropic unimode microstructures viewed from different angles (Note: rendered effect): a) Microstructure I; b) Microstructure II; c) Microstructure III; d) Microstructure IV

Based on calculated effective elastic stiffness matrices, we investigated how effective Poisson's ratios are tunable with volume fractions for the four auxetic microstructures. For each curve in Figure 3.5, the horizontal axis describes different volume fractions, and the vertical axis represents corresponding effective Poisson's ratios. Based on tensor analyses of anisotropic materials, we can calculate the maximum and minimum directional Poisson's ratios from an elastic stiffness matrix. Therefore, for a given volume fraction in the horizontal axis, there would be a range of Poisson's ratios along the vertical axis, leading to a curve with a varying width. A wider width of the curve denotes a worse isotropy of the microstructure, although the isotropy of a microstructure depends on a variety of factors. In Figure 3.5, each curve starts from the 0.1% volume fraction and ends at a volume fraction when the absolute value of the minimum Poisson's ratio is 1.1 times bigger than that of the maximum Poisson's ratio. For the microstructure I, its effective Poisson's ratio is about -0.2451 when the volume fraction is about 19.00%. For the microstructure II, its effective Poisson's ratio is about -0.3683 when the volume fraction is about 9.53%. For the microstructure III, its effective Poisson's ratio is about -0.5071 when the volume fraction is about 7.94%. For the microstructure IV, its effective Poisson's ratio is about -0.4371 when the volume fraction is about 18.02%. For all these auxetic microstructures over the variation of the volume fraction, the effective Poisson's ratio approaches -1 when the volume fraction is getting small enough.

Following the visualization scheme described in [196, 197], surfaces of directional

Poisson's ratios for four auxetic microstructures with 0.1% volume fractions are given in Figure 3.6. For each point on the surface, there is a 3D vector from the origin point to it. The direction of this vector represents the loading direction, and the norm of this vector represents the absolute value of corresponding physical property. However, since directional Poisson's ratios depend on both the loading direction and the measurement direction, they cannot be simply represented by only using single surface, due to infinite measurement directions perpendicular to a certain loading direction. Therefore, for each loading direction, maximum and minimum values among all the measurement directions are calculated and used to create two surfaces. Details about tensor analysis and graphical visualizations of elastic stiffness matrix can refer to [196].

It is obvious that all those surfaces of directional Poisson's ratios are almost spheres, and relative errors between maximum and minimum values are all below 0.006%, which demonstrate that all these microstructures are elastically isotropic. Besides, we can clearly see in Figure 3.6 that their effective Poisson's ratios approach -1, and the relative errors are all below 1%.

From Figure 3.5 and Figure 3.6, we can conclude that the four novel microstructures are able to achieve ideal elastic isotropy and extreme negative Poisson's ratios when having low volume fractions. As a lateral comparison, we can find that the microstructures I and IV can maintain the elastic isotropy over a wider range of volume fractions, and the microstructure IV has the smallest relative error.

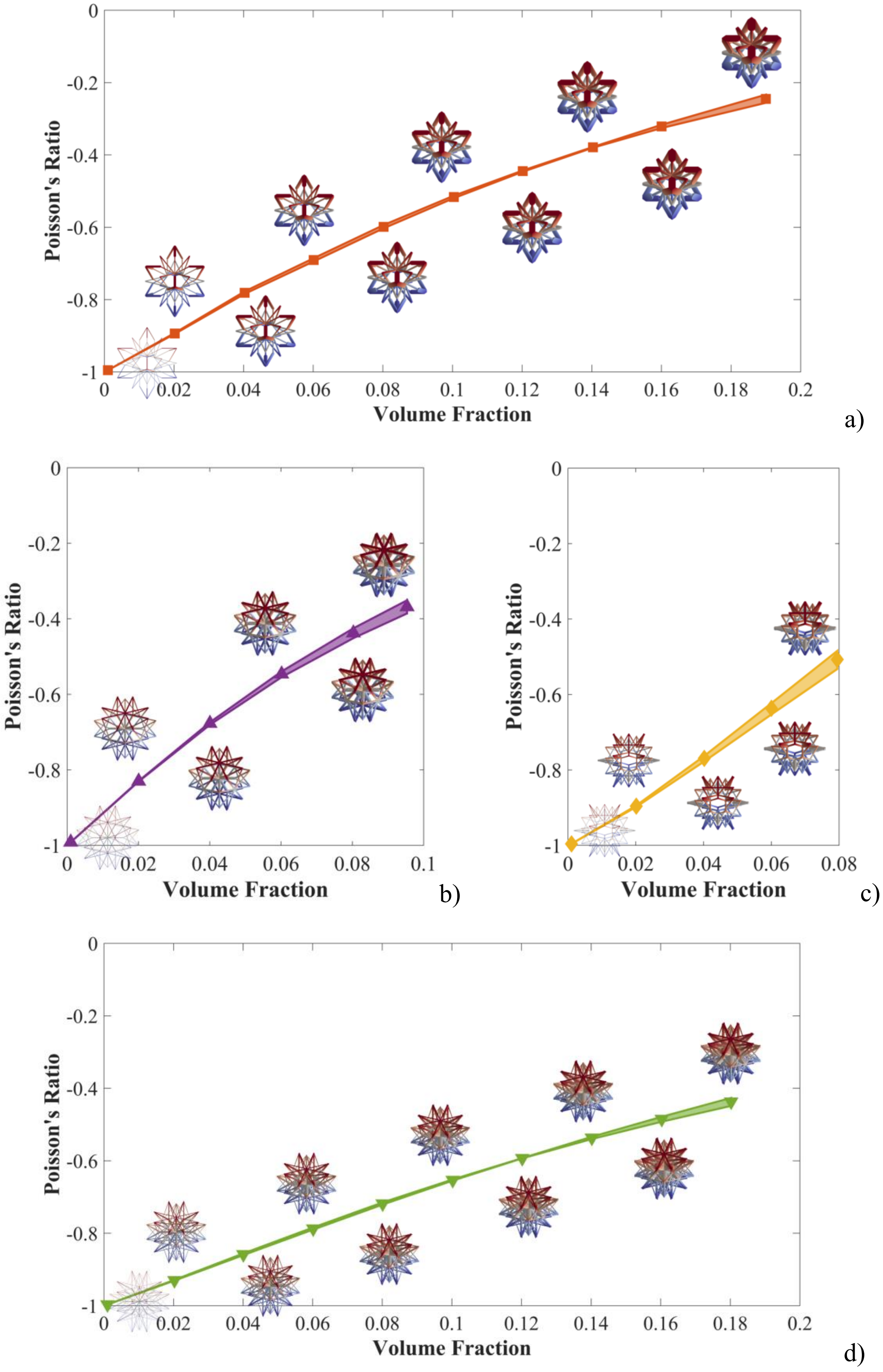

Figure 3.5. Tunable Poisson's ratios over different volume fractions. a) Microstructure I; b) Microstructure II; c) Microstructure III; d) Microstructure IV

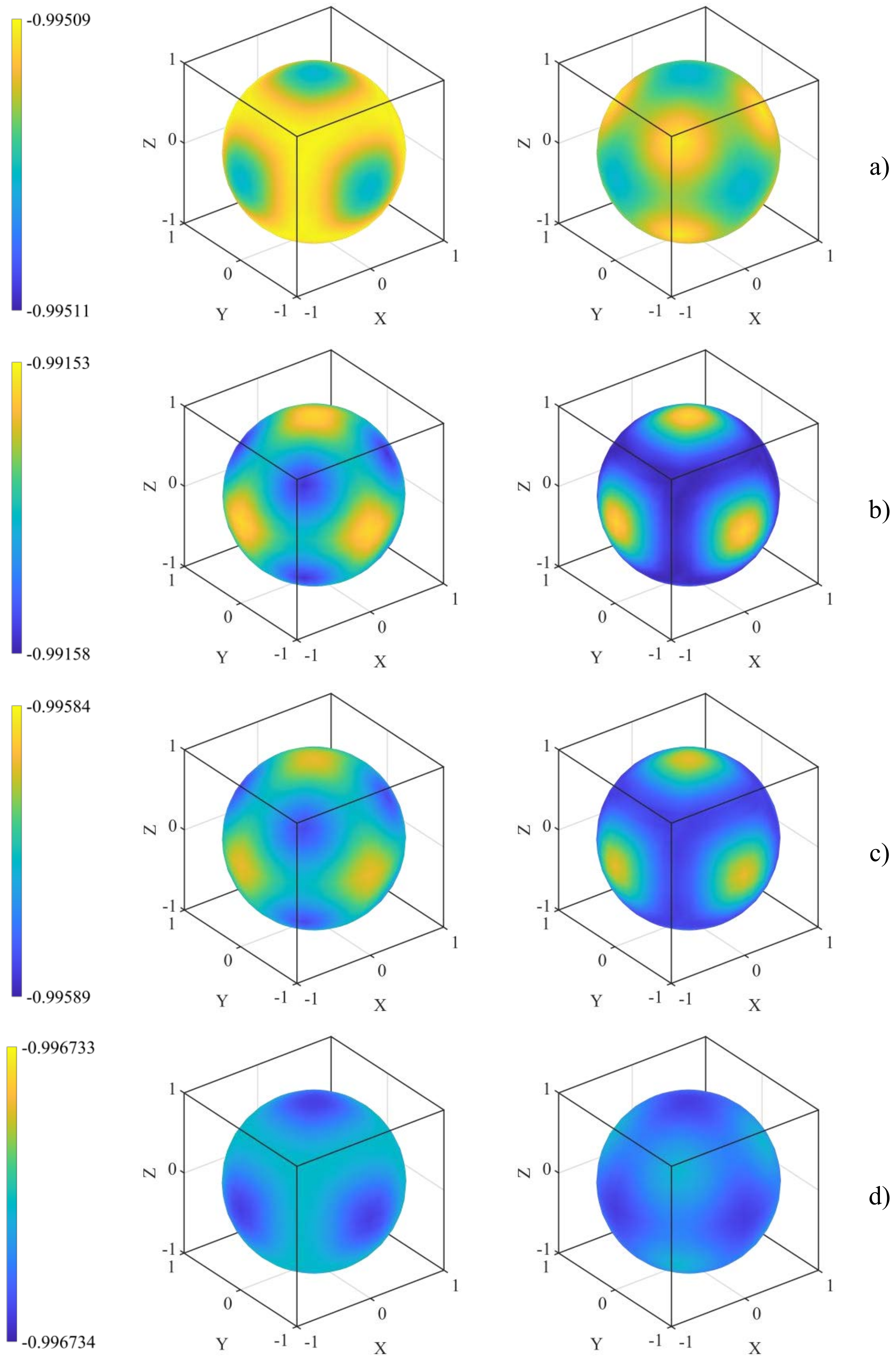

Figure 3.6. Surfaces of Poisson's ratios: a) Microstructure I; b) Microstructure II; c) Microstructure III; d) Microstructure IV. Left column: maximum Poisson's ratios; Right column: minimum Poisson's ratios.

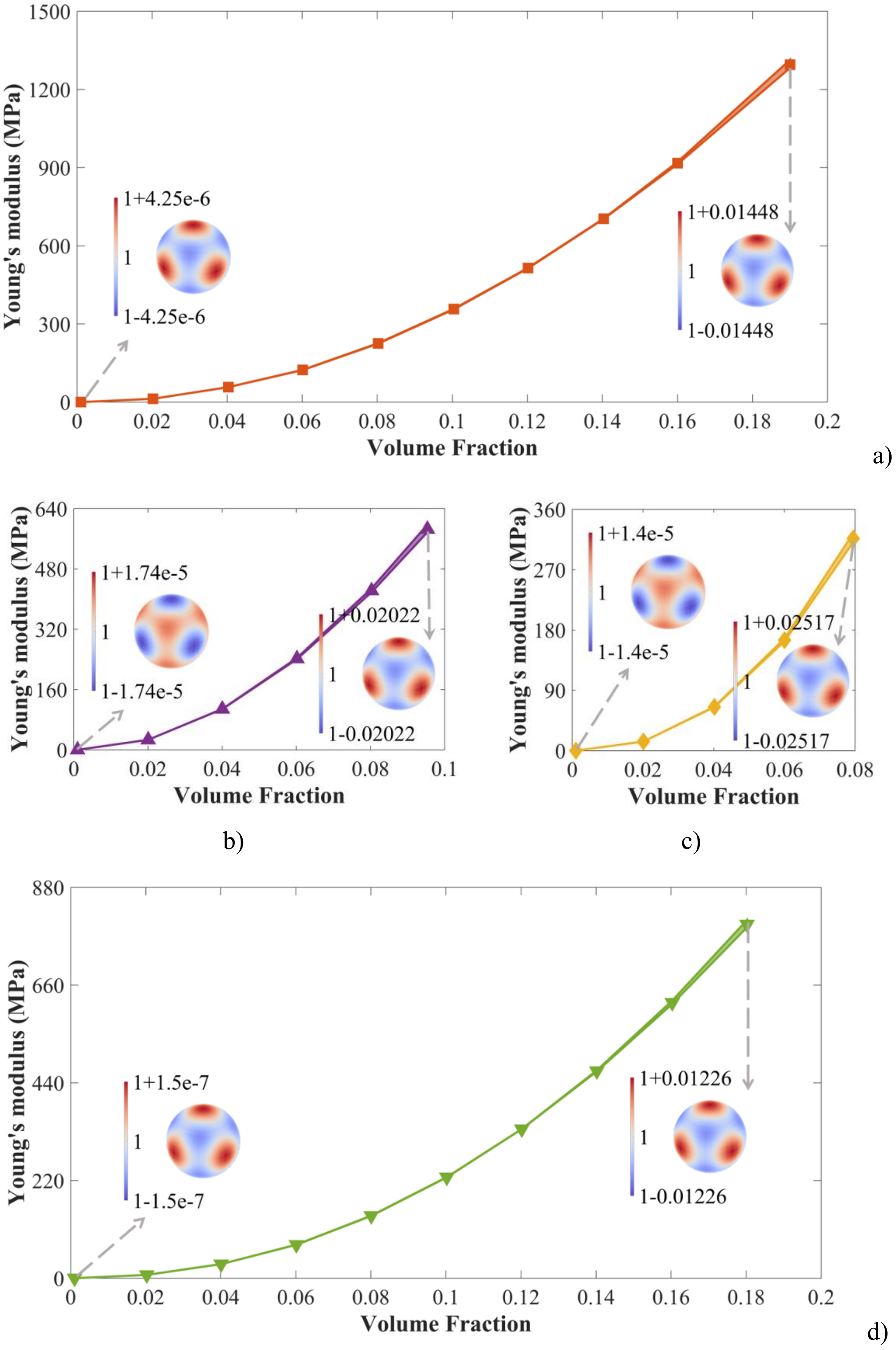

Figure 3.7. Tunable Young's moduli over different volume fractions: a) Microstructure I; b) Microstructure II; c) Microstructure III; d) Microstructure IV.

We further investigate how to tailor the effective Young's modulus through changing the volume fraction for these microstructures. For each curve in Figure 3.7, the vertical axis represents the corresponding effective Young's moduli. Figure 3.7 includes surfaces of directional Young's moduli for microstructures with two different volume fractions. By showing the directional Young's moduli for each curve, Figure 3.7 also provides insights into the anisotropy of the microstructures and how it varies with volume fraction. Different from Figure 3.6, since absolute values of Young's moduli can be seen from curves, we normalize surfaces of directional Young's moduli by their Hill averages [198]. From curves in Figure 3.7, we can see that effective Young's moduli are increasing rapidly with the increase of the volume fraction. For microstructures with 0.1% volume fraction, we can see that all those surfaces of the directional Young's moduli are almost spheres, and relative errors to Hill averages are all below 0.002%, which further demonstrates that all these microstructures are elastically isotropic. For microstructures with moderate volume fractions at the end of curves, surfaces of directional Young's moduli are still close to spheres, and relative errors to Hill averages are all below 3%. Compared with Poisson's ratios shown in Figure 3.6, Young's moduli are much closer to be elastically isotropic.

An isotropic pentamode metamaterial has a Poisson's ratio 0.5, and its stiffness characteristic is an infinite ratio of its bulk modulus to its shear modulus [128, 130]. On the contrary, for an isotropic unimode metamaterial possessing a Poisson's ratio at the theoretical lower limit -1, its stiffness characteristic is an infinite ratio of its shear modulus to its bulk modulus. Here, we investigated how the shear moduli will change with the bulk moduli for the four microstructures, which are shown in Figure 3.8. We can see that bulk moduli are decreasing more rapidly that of the shear moduli. For microstructures with lower volume fractions, ratios of the shear moduli to bulk moduli are larger. For microstructures with 0.1% volume fraction, their bulk moduli are close to zero, and ratios of shear moduli to bulk moduli are nearly infinite.

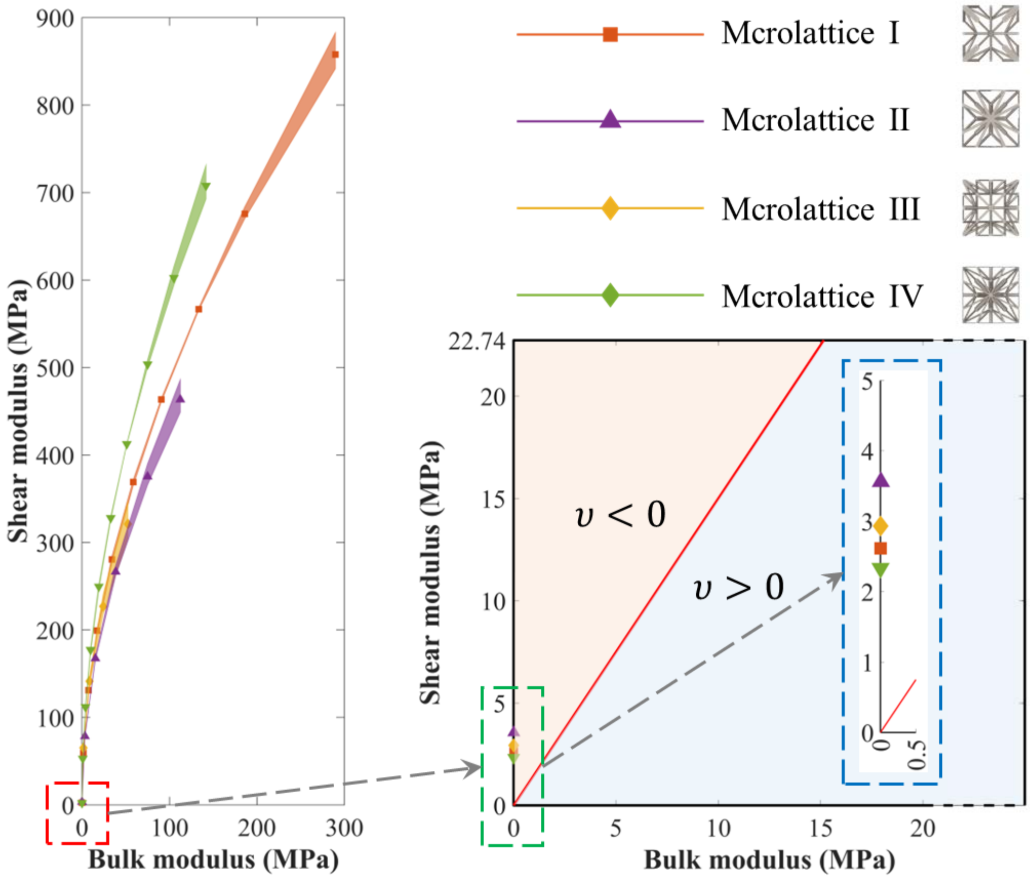

Figure 3.8. Effective bulk moduli and shear moduli. The portion of the curves in the red dashed rectangles is enlarged to be shown in the green and blue dashed rectangles.

Hence, these four strut-based microstructures can be used for auxetic metamaterials with tunability of Poisson's ratios and stiffness. Using the same strut layout, not only the theoretical lower limit -1, but also a broad range of negative values can be reached for effective Poisson's ratios by only alternating their volume fractions. We emphasize again that this tunning is based on directly increasing or decreasing cross-sectional dimensions of struts in a given optimized microstructure, which is totally different from other methods that setting different volume fractions as constraints to obtain different optimized designs.

3.3.3 Macroscopic deformation behaviors of lattice structures

As shown in Figure 3.9, the lattice structures I, II, III, and IV, are periodically assembled by using the isotropic unimode microstructures I, II, III, and IV. Since the computational homogenization is implemented under periodic boundary conditions, the number of microstructures used for configuring the bulk material has a strong effect on the macroscopic behaviors of the lattice. Here, we use lattice structures composed of 12×12×12 microstructures with 0.1% volume fractions for numerical simulations to analyze their macroscopic deformation behaviors. Numerical simulations have been conducted in COMSOL using beam elements. Each lattice structure is compressed along the Z-direction and can freely deform in the XY-plane. It is obvious that we can use a submodel that consists of 6×6×6 microstructures for a finite element analysis considering symmetric boundary conditions, which is illustrated in Figure 3.10a, b. Besides, six faces of the analyzed structure are defined in Figure 3.10b.

Finite element analysis results are given in Figure 3.11 and Figure 3.12, in which rainbow colors indicate different negative ratios of the X-direction translational displacement to the forced vertical displacement. In Figure 3.11, for the left column, lines with black color represent undeformed geometries viewed from the front face, and lines with rainbow colors represent deformed structures in a proper scale. For the right column, each lattice structure is viewed from the right face, but all other beams and vertices not lying exactly on the right face are invisible. From the left column of Figure 3.11, we can see that lattice structures keep their shapes almost unchanged when

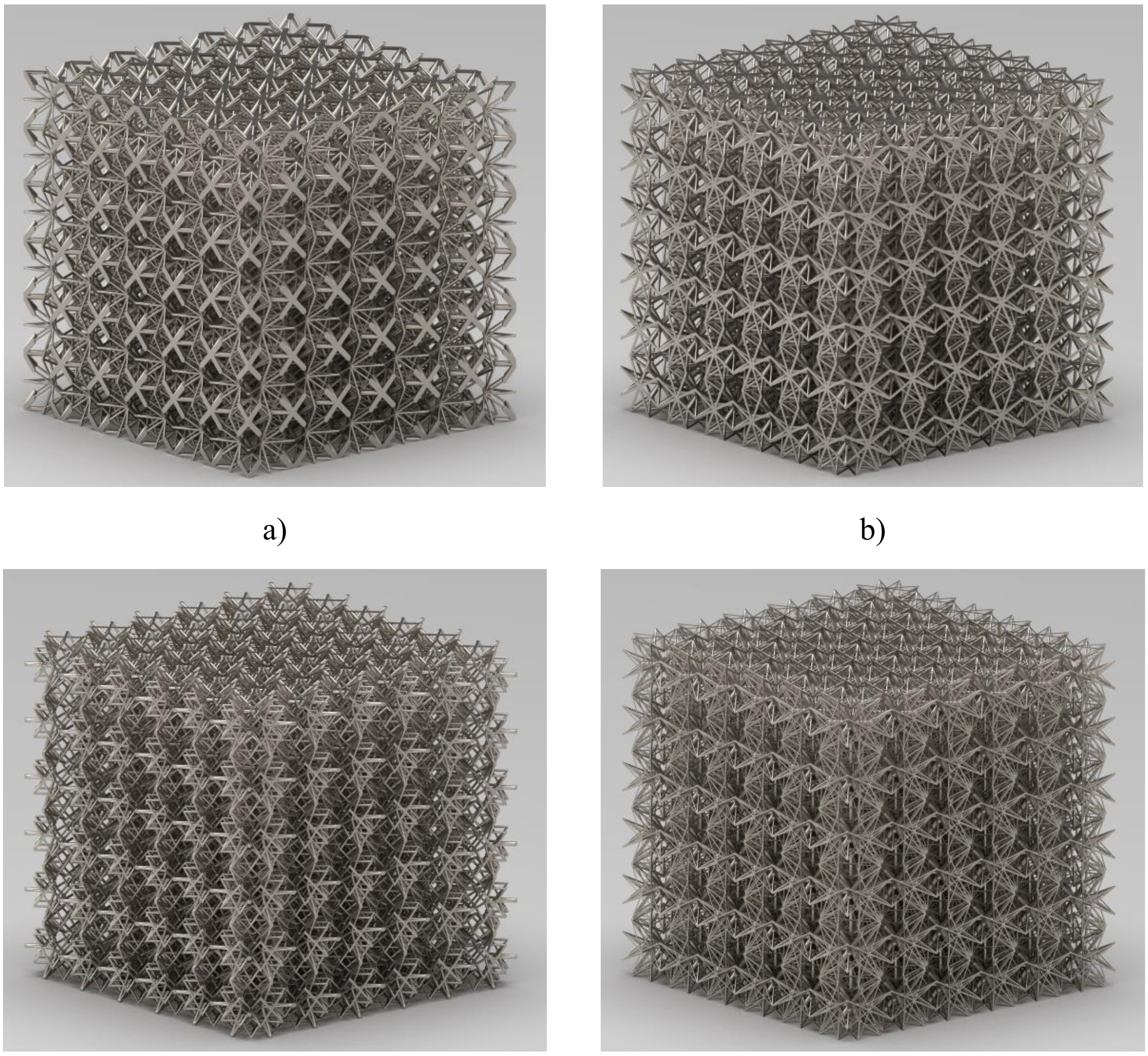

a) b)

c) d)

Figure 3.9. Lattice structures periodically assembled by novel isotropic unimode microstructures (Note: rendered effect): a) Lattice I; b) Lattice II; c) Lattice III; d) Lattice IV

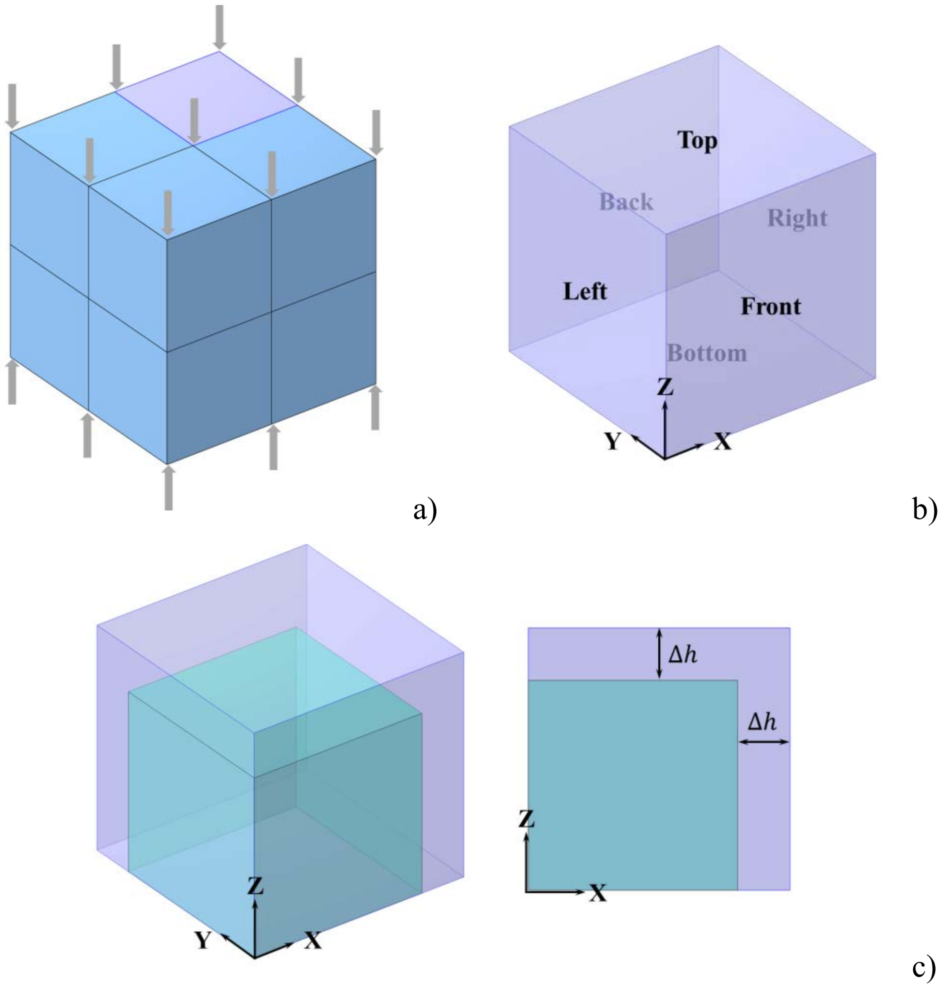

a) b) c)

Figure 3.10. Symmetric analysis model and expected deformation. a) A 3D structure with three orthogonal plane symmetries is under the uniaxial compression. The purple region represents one-eighth of the whole structure. b) For the one-eighth sub-structure, roller boundary conditions are imposed on the left, front, and bottom faces, while forced non-zero vertical displacements are imposed on the top face. c) For a cube (purple color) with isotropic Poisson's ratio -1, it would deform to be a smaller cube (green color) rather than a cuboid when uniaxially compressed.

deformed, which are represented by red dash squares. In other words, under a uniaxial compression, a cube-like lattice structure becomes smaller in all directions but keeps the shape as a cube. The demonstration of an isotropic material with a Poisson's ratio -1 is illustrated in Figure 3.10c. We can see that displacement ratios shown in the right column of Figure 3.11 are all below -0.99 for the lattice I. However, for other three lattice structures, displacement ratios are over -0.99 in partial due to the boundary effect. We triple the number of microstructures in each lattice structure for finite element analyses, and displacement ratios on right faces are shown in Figure 3.12. We can see that displacement ratios are all below -0.99 for the lattice IV now. Moreover, maximum displacement ratios of the lattice II and III are decreased from -0.9083 and -0.8707 to -0.9640 and -0.9543, respectively, which are closer to their homogenized Poisson's ratios. We can see that, when the lattice structure consists of a larger number of periodic underline microstructures, the less boundary effect occurs at its outer regions, where periodic boundary conditions cannot be satisfied due to a lack of neighboring microstructures. Besides, for different microstructures, the dependency of the boundary effect on the number of microstructures is also different.

3.4. Conclusion

In this work, we developed a generic rational design method using topology optimization to create mechanical metamaterials possessing both ideal elastic isotropy and extreme negative Poisson's ratio. Using this systematic method, novel 3D strut-based microstructures have been designed to demonstrate that ideal isotropy and Poisson's ratios close to -1 can be simultaneously achieved within one integrated design. It is worth noting that these 3D unimode microstructures are single-scale, single-phase, and constructed by elastic continua without using any mechanism components.

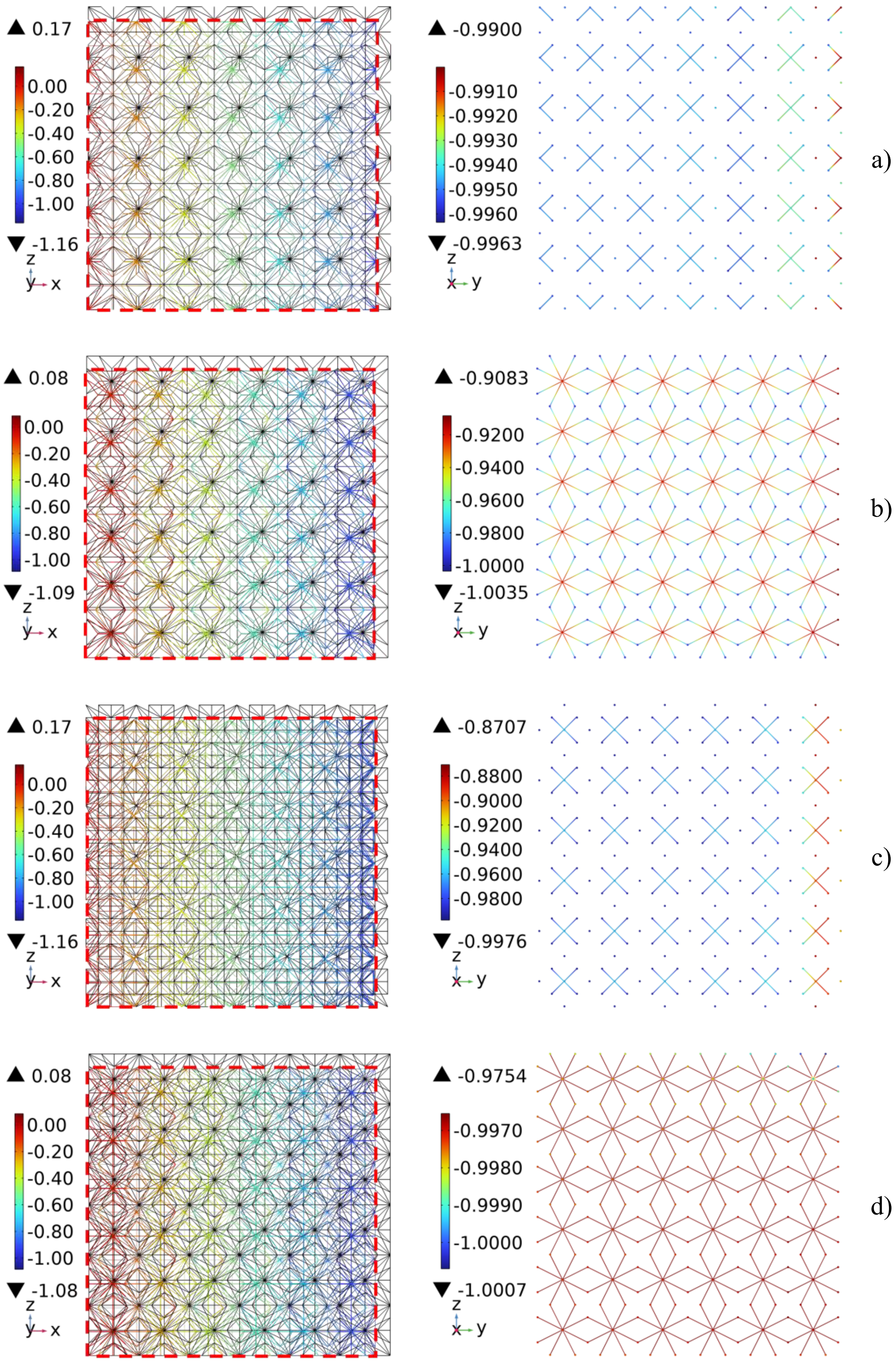

Figure 3.11. Negative ratios of the displacement in the X-direction to the forced displacement in the Z-direction: a) Lattice I; b) Lattice II; c) Lattice III; d) Lattice IV.

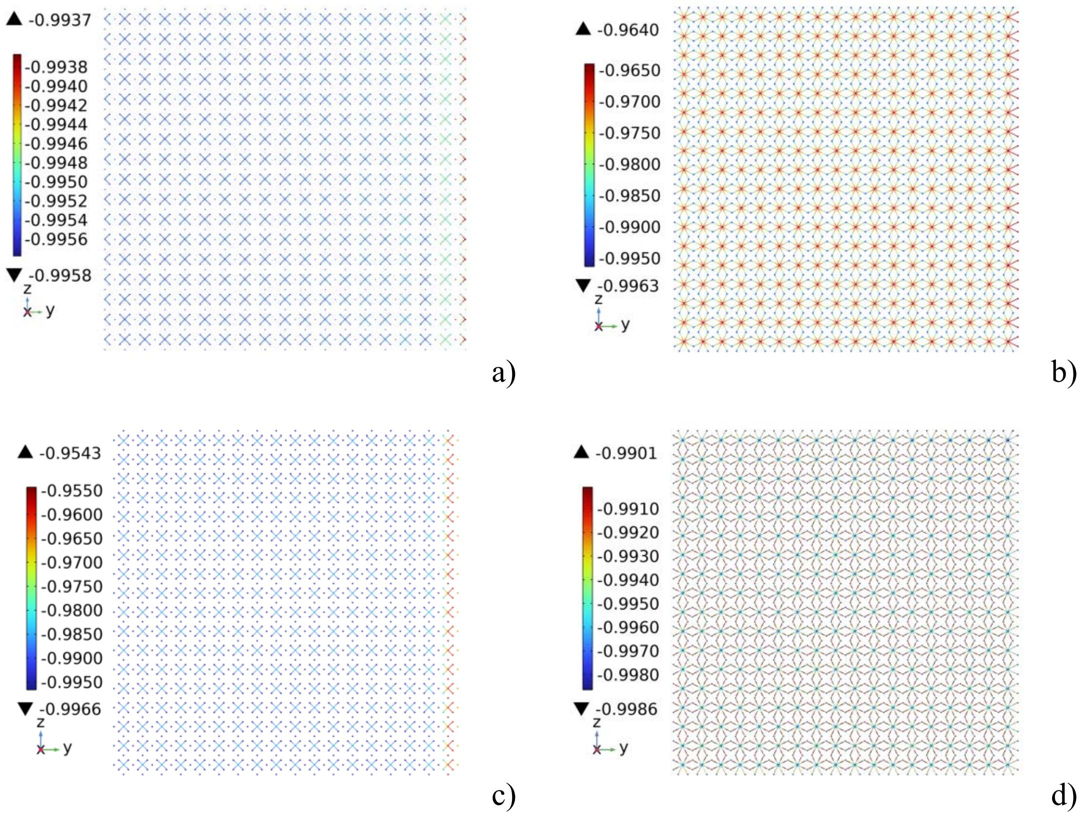

Figure 3.12. Negative displacement ratios of 18×18×18 microstructures: a) Lattice I; b) Lattice II; c) Lattice III; d) Lattice IV

We also numerically investigated customizing their effective material properties over a range of volume fractions. These microstructures exhibit ideal elastic isotropy and Poisson's ratios -1 when the volume fractions are sufficiently small. As the volume fraction increase, their Poisson's ratio and stiffness modulus also increase. By comparison, the type I and type IV microstructures can maintain their elastic isotropy over a larger range of volume fractions. These strut-based microstructures can be applied to develop wide-ranging metamaterials with tunability of negative Poisson's ratios and stiffness. We further analyzed macroscopic deformation behaviors of lattices structures with periodically arranged microstructures under uniaxial compression. Their sizes or volumes can be easily changed, while their shapes almost remain the same.

Chapter 4 Design of Multi-material Isotropic Auxetic Microstructures with Zero Thermal Expansion

4.1. Introduction

This chapter is a modified version of the journal paper titled “Design of multi-material isotropic auxetic microstructures with zero thermal expansion”, which was published in *Materials & Design* (Volume 222, 111051).

As introduced in Chapter 3, auxetic metamaterials have drawn great attention due to their exceptional mechanical properties and wide-spread applications, such as anti-blast equipment, vibration dampeners, smart filtration, and biomedical implants. However, 3D isotropic auxetic metamaterials with zero thermal expansion (ZTE) are still missing and in demand. The coefficient of thermal expansion (CTE) refers to the degree to which the length of a material changes in proportion to a change in temperature, typically expressed as a fractional value. It is a basic rule of physics that can affect the behavior and performance of materials and structures, particularly in applications where there are large temperature variations or thermal cycling. Understanding and controlling the CTE is therefore important in many fields of engineering and materials science. Most of common materials exhibit positive thermal expansion (PTE). They expand when they are heated and contract when they are cooled, as illustrated in Figure 4.1. This is because the atoms of these materials usually vibrate more vigorously and take up more space as the temperature rises, causing the materials to expand.

For metamaterials with non-positive thermal expansion coefficients, they exhibit unusual thermal deformation behaviors. For example, ZTE is a rare physical property, while a material with ZTE can maintain its geometrical shape and dimension unchanged over a certain temperature range. Hence, a ZTE material is expected to be thermally dimensionally stable across a range of temperatures. Since it is hard to find a material in nature that can withstand temperature changes without deforming, artificially engineered materials with ZTE are in high demand and will find applications in many engineering domains, e.g., high-precision devices and optical devices, where dimensional stability is crucial for their performance and reliability.

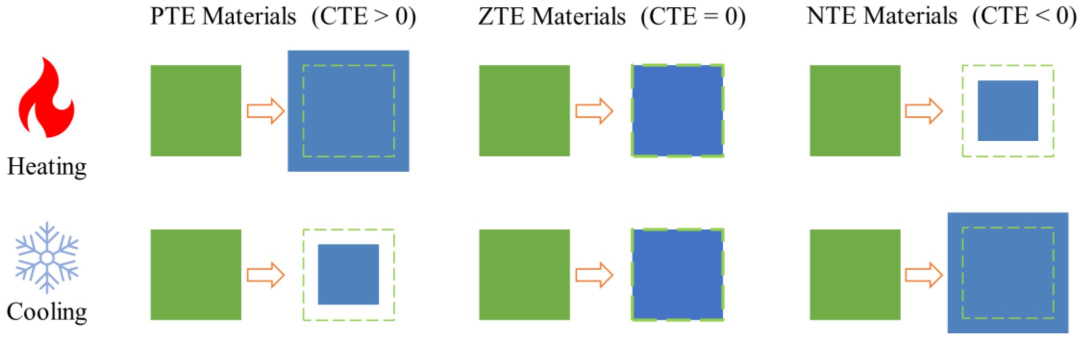

Figure 4.1. Thermal deformation of PTE, ZTE, and NTE materials

In this chapter, we will focus on designing auxetic metamaterials with ZTE, which have more potential in practice for wide-ranging applications due to their thermal dimensional stability in temperature-changing environments and identical material properties in any direction.

Gibson and Ashby [199] showed that the CTE of a single-material open-cell foam is equal to the CTE of its constituent material. Therefore, it is theoretically impossible to use a single constituent solid material with a non-zero CTE to design a ZTE microstructure. Only for a composite, it is possible to mix two or more constituent materials with dissimilar CTE values to achieve ZTE through designs [200, 201]. Hence, this chapter will develop a rational design method based on multi-material continuum topology optimization to find novel 3D isotropic NPR-ZTE microstructures.

It is worthy of note that, nowadays multi-material additive manufacturing grows fast for fabricating customized components to achieve tailored properties in a single process. It has recently been explored to deliver multi-material components, but there are still issues in mixing multiple materials with variable composition and properties, such as distribution of different metals or alloys within one layer, and multi-material interfacial strength. Hence, by using numerical simulation techniques, the objective of this work is to provide insights into studying effective properties of topologically optimized designs, rather than physical prototyping and testing in a laboratory setting.

4.2. Multi-material continuum topology optimization

In this section, we develop a continuum topology optimization method for systematically designing 3D isotropic NPR-ZTE microstructures. First, we establish a mathematical optimization formulation in accordance with the characteristics of elastically cubic symmetric materials. Second, the density-based topology optimization method and the material interpolation models are briefly introduced. Third, we will rigorously derive the sensitivity formulas for the mathematical optimization formulation.

Finally, the implementation detail of imposing a geometric cubic symmetry constraint on the design domain is introduced.

4.2.1. Homogenized coefficients of thermal expansion

The systematic design method proposed in this chapter is under the assumption that every intermediate design during the optimization iterations has at least elastic cubic symmetry. This assumption is guaranteed by imposing a geometric cubic symmetry constraint on the design domain, the detail of which will be given later in Section 4.2.4. For any 3D linear elastic material with elastic cubic symmetry, its elastic stiffness matrix $\boldsymbol{C}$ in the Voigt notation with engineering shear strains is given in Equation (3.1), and its CTE tensor $\boldsymbol{a}$ must be isotropic as written in Equation (4.1).

$$\boldsymbol{a} = [a_{11} \quad a_{11} \quad a_{11} \quad 0 \quad 0 \quad 0]^{\mathrm{T}} \tag{4.1}$$

Compared with anisotropic materials, we can see that the number of unique elastic constants is reduced from 21 to 3, and the number of unique thermal expansion coefficients changes from 6 to 1. Therefore, the definition of concerned material properties in topology optimization can be simplified.

During optimization iterations, the computational homogenization method introduced in Section 2.3.2 is employed to evaluate intermediate designs' effective material properties, including effective elastic stiffness matrices and effective coefficients of thermal expansion. In finite element analyses using solid elements for the homogenization, the periodic boundary conditions in Equation (2.21) can be imposed as multi-point constraints in the matrix form:

$$\boldsymbol{GU} = \boldsymbol{Q} \tag{4.2}$$

where $\boldsymbol{G}$ is a constant matrix and $\boldsymbol{Q}$ is a constant vector. Taking two independent equality constraints $u_3 - u_1 = 1$ and $u_4 - u_2 = 0$ as the example, they can be rewritten in the matrix form as $[-1\ \ 0\ \ 1\ \ 0;\ 0\ \ -1\ \ 0\ \ 1]\{u_1\ \ u_2\ \ u_3\ \ u_4\}^{\mathrm{T}} = \{1\ \ 0\}^{\mathrm{T}}$.

Such multi-point constraints can be exactly satisfied by using the Lagrange multiplier method for finite element analysis. We give the equilibrium equations as Equation (4.3).

$$\begin{bmatrix} \boldsymbol{K} & \boldsymbol{G}^T \\ \boldsymbol{G} & \boldsymbol{0} \end{bmatrix} \begin{Bmatrix} \boldsymbol{U} \\ \boldsymbol{\lambda} \end{Bmatrix} = \begin{Bmatrix} \boldsymbol{F} \\ \boldsymbol{Q} \end{Bmatrix} \tag{4.3}$$

where $\boldsymbol{\lambda}$ is the vector of unknown Lagrange multipliers, and $\boldsymbol{F}$ is the nodal force vector. For the computational homogenization of $\boldsymbol{C}^H$ based on prescribed macroscopic strains, the nodal values of $\boldsymbol{F}$ are all zero except for the fixed node with zero displacements.

Using the computational homogenization method, the vector of effective CTE tensor $\boldsymbol{a}^H$ of a microstructure can be calculated by:

$$\boldsymbol{a}^H = -\boldsymbol{C}^{H^{-1}}\overline{\boldsymbol{\sigma}}_{th} \tag{4.4}$$

where $\overline{\boldsymbol{\sigma}}_{th}$ is the vector of average stress components calculated in a different load case that considers the thermal expansion effect of constituent materials. In this load case, a unit temperature increase is applied, and periodic boundary conditions in Equation (2.21) are also considered in the finite element analysis, but macroscopic average strain components are all set as zero. The formula of $\bar{\boldsymbol{\sigma}}_{th}$ is:

$$\bar{\boldsymbol{\sigma}}_{th} = \frac{1}{V}\sum_{e=1}^{n}\left(\int_{\Omega_e} \boldsymbol{D}_e(\boldsymbol{B}_e\boldsymbol{u}_\theta^e - \boldsymbol{\alpha}_e)d\Omega_e\right) \tag{4.5}$$

where $\boldsymbol{D}_e$, $\boldsymbol{B}_e$, $\boldsymbol{\alpha}_e$, and Ω_e are respectively the elastic stiffness matrix, the strain-displacement matrix, the thermal expansion coefficient vector, and the volume of the eth element in the finite element analysis. The subscript θ represents the load case considering thermal expansion effects. n is the total number of elements.

Since a stress-form $\bar{\boldsymbol{\sigma}}_{th}$ will lead to difficulties on sensitivity derivations, based on the following Hill-Mandel lemma [152]:

$$\bar{\boldsymbol{\sigma}} : \bar{\boldsymbol{\varepsilon}} = \langle\boldsymbol{\sigma}\rangle : \langle\boldsymbol{\varepsilon}\rangle = \langle\boldsymbol{\sigma} : \boldsymbol{\varepsilon}\rangle \tag{4.6}$$

we can rewrite $\bar{\boldsymbol{\sigma}}_{th}$ to be a mutual energy form as follows:

$$\bar{\boldsymbol{\sigma}}_{th} = \boldsymbol{I}\,\bar{\boldsymbol{\sigma}}_{th} = \frac{1}{V}\sum_{e=1}^{n}\left(\int_{\Omega_e} {\boldsymbol{u}_\phi^e}^T {\boldsymbol{B}_e}^T \boldsymbol{D}_e(\boldsymbol{B}_e\boldsymbol{u}_\theta^e - \boldsymbol{\alpha}_e)d\Omega_e\right) \tag{4.7}$$

where $\boldsymbol{I}$ is an identity matrix representing macroscopic strain fields for the homogenization of $\boldsymbol{C}^H$, and the subscript ϕ represents the six load cases for calculating $\boldsymbol{C}^H$.

This energy-form $\bar{\boldsymbol{\sigma}}_{th}$ can be further rewritten as the finite element discretization form:

$$\begin{aligned}\bar{\boldsymbol{\sigma}}_{th} &= \frac{1}{V}\sum_{e=1}^{n}\left(\int_{\Omega_e} {\boldsymbol{u}_\phi^e}^T {\boldsymbol{B}_e}^T\boldsymbol{D}_e\boldsymbol{B}_e\boldsymbol{u}_\theta^e - {\boldsymbol{u}_\phi^e}^T {\boldsymbol{B}_e}^T\boldsymbol{D}_e\boldsymbol{\alpha}_e d\Omega_e\right)d\Omega \\ &= \frac{1}{V}\left({\boldsymbol{U}_\phi}^T\boldsymbol{K}\boldsymbol{U}_\theta - {\boldsymbol{U}_\phi}^T\boldsymbol{F}_\theta\right)\end{aligned} \tag{4.8}$$

4.2.2. Mathematical optimization formulation

The necessary and sufficient condition for a stiffness matrix $\boldsymbol{C}$ given in Equation (3.1) to be elastically isotropic is given in Equation (3.2). Once the condition of isotropy is satisfied, the Poisson's ratio ν and Young's modulus E can be calculated by Equation (3.3) and (3.4). When the Poisson's ratio is required to be a given value ν_{obj}, the necessary and sufficient condition required for the elastic constants will be defined as Equation (4.9). Moreover, if the given Poisson's ratio is non-zero, E is directly proportional to C_{12}, which is rewritten in Equation (4.10). We can find that the Young's modulus E will become larger when C_{12} becomes smaller if $-1 < \nu_{\mathrm{obj}} < 0$.

$$\frac{\nu_{\mathrm{obj}}}{1-\nu_{\mathrm{obj}}} C_{11} - C_{12} = 0 \tag{4.9}$$

$$E = \frac{1-\nu_{\mathrm{obj}} - 2{\nu_{\mathrm{obj}}}^2}{\nu_{\mathrm{obj}}} C_{12} \tag{4.10}$$

To simultaneously achieve three optimization targets, i.e., elastic isotropy, negative Poisson's ratio, and zero thermal expansion, three corresponding quadratic penalty terms are added into the objective function. Based on Equation (3.2), the minimization of $(C_{11} - C_{12} - 2C_{44})^2$ can ensure that the optimized microstructure is isotropic. Based on Equation (4.9), the minimization of $\left((\nu_{\mathrm{obj}}/(1-\nu_{\mathrm{obj}}))C_{11} - C_{12}\right)^2$ can ensure that the optimized microstructure has a Poisson's ratio approaching the specific value. Based on Equation (4.1), the minimization of ${a_{11}}^2$ can ensure that the optimized microstructure has a nearly zero thermal expansion coefficient. Moreover, to avoid an optimized design with impractically low stiffness, the minimization of C_{12} is also added into the objective function to enhance the Young's modulus based on Equation (4.10).

Two upper limits are respectively applied to the total volume of all solid materials and the volume of one specific solid phase material, which are imposed as the inequality constraints. The values of upper limits can be decided depending on the requirements of specific application situations.

To design a 3D microstructure, the design domain for topology optimization is defined as a cube. Since one of the optimization targets is to achieve ZTE, at least two phases of solid materials with dissimilar CTE values will be required in the design. Therefore, this is a multi-material optimization problem, and two types of artificial element densities will be used to describe structural topologies.

Finally, a general mathematical optimization formulation can be defined as in Equation (4.11), where $\boldsymbol{\rho}$ is a vector of design variables related to artificial densities of each element, V^s and V^{s2} are the material volumes respectively of all solid phases and the second solid phase, $V^s_{\max}$ and $V^{s2}_{\max}$ are the corresponding allowable maximum volumes. To enhance the optimization performance, the appropriate values of weight factors $\boldsymbol{\omega}$ in the objective function can be normalized by reference values of constituent materials. For instance, the four weight factors are respectively $1/\omega_s$, $1\mathrm{e}4/{\omega_{refs}}^2$, $1\mathrm{e}4/{\omega_{refs}}^2$, and $1\mathrm{e}2/{\omega_{refc}}^2$ for the numerical example in Section 4.3.1, where ω_{refs} and ω_{refc} are respectively selected from the Young's modulus and the CTE value of one constituent material.

When the objective function is minimized, the three quadratic penalty terms will all approach zero and then ensure that the optimized design is elastically isotropic, has a prescribed negative Poisson's ratio, and has a nearly zero CTE value.

Find: $\boldsymbol{\rho} = [\boldsymbol{\rho}^1 \quad \boldsymbol{\rho}^2] = [\rho_1^1 \quad \rho_2^1 \quad \dots \quad \rho_{n-1}^1 \quad \rho_n^1 \quad \rho_1^2 \quad \rho_2^2 \quad \dots \quad \rho_{n-1}^2 \quad \rho_n^2]$

Min:

$$\begin{aligned} f(\boldsymbol{\rho}) = {} & \omega_{stiff} {C_{12}}^H(\boldsymbol{\rho}) + \omega_{iso}\left({C_{11}}^H(\boldsymbol{\rho}) - {C_{12}}^H(\boldsymbol{\rho}) - 2{C_{44}}^H(\boldsymbol{\rho})\right)^2 \\ & + \omega_{npr}\left(\frac{\nu_{\text{obj}}}{1-\nu_{\text{obj}}}{C_{11}}^H(\boldsymbol{\rho}) - {C_{12}}^H(\boldsymbol{\rho})\right)^2 + \omega_{zte}{a_{11}}^H(\boldsymbol{\rho})^2 \end{aligned} \tag{4.11}$$

S. t.

$$\begin{cases} V^s(\boldsymbol{\rho}) \le V_{\max}^s \\ V^{s2}(\boldsymbol{\rho}) \le V_{\max}^{s2} \end{cases}$$

4.2.3. Multi-material density-based method

In the density-based topology optimization method, each element in the mesh is assigned with two artificial density variables to represent its material constituent. For each element, the first density variable $\tilde{\rho}^1$ represents the element is solid or void, and the second density variable $\tilde{\rho}^2$ represents which solid material the element will have. The value of each artificial density variable continuously varies between 0 and 1. For the e-th element with intermediate densities, the values of its material properties are calculated using the following material interpolation models:

$$\boldsymbol{D}_e = \boldsymbol{D}_e^1 + {\tilde{\rho}_e^1}^P(\boldsymbol{D}_e^2 - \boldsymbol{D}_e^1) + {\tilde{\rho}_e^1}^P {\tilde{\rho}_e^2}^P(\boldsymbol{D}_e^3 - \boldsymbol{D}_e^2) \tag{4.12}$$

$$\boldsymbol{\alpha}_e = \boldsymbol{\alpha}_e^1 + \tilde{\rho}_e^1(\boldsymbol{\alpha}_e^2 - \boldsymbol{\alpha}_e^1) + \tilde{\rho}_e^1\tilde{\rho}_e^2(\boldsymbol{\alpha}_e^3 - \boldsymbol{\alpha}_e^2) \tag{4.13}$$

where $\boldsymbol{D}_e^l$ and $\boldsymbol{\alpha}_e^l$ are respectively the elastic stiffness matrix and the thermal expansion coefficient vector of the l-th phase of constituent materials ($l = 1, 2, 3$). P is a parameter of the power-law relationship for the interpolation model in Eq (4.12), which is selected as 3 for the numerical example in Section 4.3.1. However, there is no need to apply such a power-law interpolation to $\boldsymbol{\alpha}_e$ in Eq (4.13), since black-white optimized designs can already be obtained by using a linearly interpolated CTE value. In this chapter, the first phase is void and the rest two are solids. The void will be treated as weak material with properties, i.e., $\boldsymbol{D}_e^1$ and $\boldsymbol{\alpha}_e^1$, to avoid numerical instability, defined by designers before the optimization. Hence, weak material properties are independent of the second solid density variables and keep unchanged during the optimization.

For the volume constraints in the optimization formulation, they are calculated using the following material interpolation models:

$$V^s = \sum\nolimits_{e=1}^{n} v_e^s = \sum\nolimits_{e=1}^{n} (\tilde{\rho}_e^1 v_e) \tag{4.14}$$

$$V^{s2} = \sum\nolimits_{e=1}^{n} v_e^{s2} = \sum\nolimits_{e=1}^{n} (\tilde{\rho}_e^1 (1 - \tilde{\rho}_e^2) v_e) \tag{4.15}$$

where v_e^s and v_e^{s2} are respectively the materials volumes of all solid phases and the second solid phase for the e-th element, and v_e is the spatial volume of the e-th element.

By changing the elemental density field values of a fixed finite element mesh, the spatial distribution of materials in the design domain can be changed. Therefore, optimization of topologies can be realized by linking design variables with elemental densities using the density filtering given in Equation (4.16) and the threshold projection in Equation (4.17).

$$\hat{\rho}_e^l = \frac{\sum_{j\in\mathbb{N}_e}\left(r_f - d_{ej}\right)v_j\rho_j^l}{\sum_{j\in\mathbb{N}_e}\left(r_f - d_{ej}\right)v_j} \tag{4.16}$$

where $\mathbb{N}_e$ are the set of all neighboring elements whose distance to the e-th element is smaller than a specified filter radius r_f; d_{ej} is the Euclidean distance between centers of the e-th and the j-th elements.

$$\tilde{\rho}_e^l = \frac{\tanh(\beta\eta) + \tanh(\beta\hat{\rho}_e^l - \beta\eta)}{\tanh(\beta\eta) + \tanh(\beta - \beta\eta)} \tag{4.17}$$

where β and η are parameters that can be automatically adjusted during the optimization. For further details about the filtering and the projection schemes, the readers can refer to [19].

4.2.4. Geometric constraint

As mentioned in Section 4.2.1, a geometric cubic symmetry constraint is applied on the design domain to guarantee that every intermediate design during the optimization has at least elastic cubic symmetry. In this chapter, such a geometric constraint is imposed by clustering the densities of symmetric elements. As illustrated in Figure 4.2, the cubical design domain is divided into 48 subdomains by 9 symmetric planes. For every two elements, respectively from two subdomains, that are symmetric about one of the planes, they have the same density values. In other words, for each element in one subdomain, it has the same density values as other 47 corresponding elements. Therefore, design variables are assigned to only one of the subdomains, which is named as the primary subdomain.

After elemental density values of the primary subdomain are calculated by the density filtering and the threshold projection from the design variables, density values of other subdomains can be easily obtained based on the clustering relationship given as follows:

$$\tilde{\rho}_E^l = \tilde{\rho}_e^l \qquad (\forall\, e \in \mathbb{Q}, \quad \forall\, E \in \mathbb{Z}_e) \tag{4.18}$$

where $\mathbb{Q}$ is the set of all elements in the primary subdomain, and $\mathbb{Z}_e$ is the set of 48 elements that are clustered to the eth element including the e-th element itself. To guarantee that each element in the primary subdomain can find its uniquely corresponding 47 elements in other subdomains, the total mesh of the full design domain is assembled by the unstructured mesh of the primary subdomain using solid elements with repeated mirror operations, which is illustrated in Figure 4.2.

4.2.5. Sensitivity analysis

To utilize the benefits of mathematical programming algorithms to solve optimization problems, sensitivities of the objective function and the constraint functions to the design variables will be rigorously derived here. Based on the chain rule, the sensitivity for any function $\mathcal{H}$ to a design variable ρ_k^l is given by:

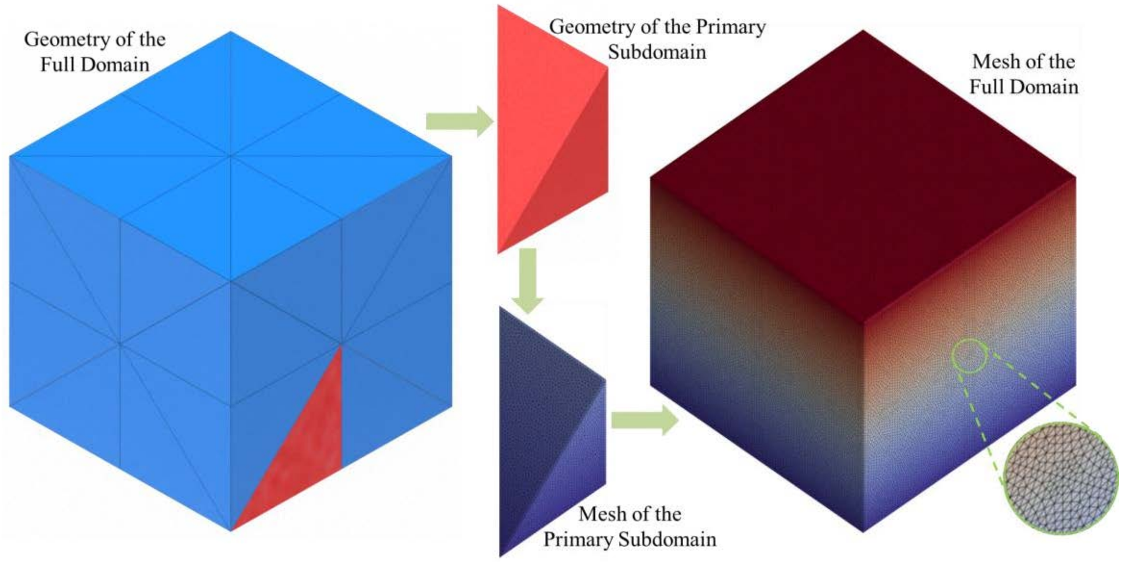

Figure 4.2. Geometric cubic symmetry of a continuum design domain

$$\frac{\partial \mathcal{H}}{\partial \rho_k^l} = \sum\nolimits_{e \in \mathbb{N}_k} \left(\left(\sum\nolimits_{E \in \mathbb{Z}_e} \frac{\partial \mathcal{H}}{\partial \tilde{\rho}_E^l} \right) \frac{\partial \tilde{\rho}_e^l}{\partial \hat{\rho}_e^l} \frac{\partial \hat{\rho}_e^l}{\partial \rho_k^l} \right), \qquad l = 1, 2 \quad k = 1, 2, \dots, \frac{n}{48} \tag{4.19}$$

For the density filtering, from Equation (4.16) we will have

$$\frac{\partial \hat{\rho}_e^l}{\partial \rho_k^l} = \frac{(r_f - d_{ek}) v_k}{\sum_{j \in \mathbb{N}_e} (r_f - d_{ej}) v_j} \tag{4.20}$$

For the threshold projection, Equation (4.17) gives

$$\frac{\partial \tilde{\rho}_e^l}{\partial \hat{\rho}_e^l} = \beta \frac{1 - \tanh^2(\beta \hat{\rho}_e^l - \beta \eta)}{\tanh(\beta \eta) + \tanh(\beta - \beta \eta)} \tag{4.21}$$

The sensitivities of constraint functions with respect to the elemental densities can be derived from Equation (4.14) and Equation (4.15) as follows:

$$\begin{cases} \dfrac{\partial V^s}{\partial \tilde{\rho}_e^1} = v_e \\[2ex] \dfrac{\partial V^s}{\partial \tilde{\rho}_e^2} = 0 \end{cases} \tag{4.22}$$

$$\begin{cases} \dfrac{\partial V^{s2}}{\partial \tilde{\rho}_e^1} = (1 - \tilde{\rho}_e^2) v_e \\[2ex] \dfrac{\partial V^{s2}}{\partial \tilde{\rho}_e^2} = -\tilde{\rho}_e^1 v_e \end{cases} \tag{4.23}$$

In accordance with Equation (4.11), the sensitivity of the objective function with respect to any elemental density can be derive by

$$\begin{aligned}\frac{\partial f}{\partial \tilde{\rho}_e^l} &= \omega_{stiff}\frac{\partial {C_{12}}^H}{\partial \tilde{\rho}_e^l} + 2\omega_{zte}{a_{11}}^H\frac{\partial {a_{11}}^H}{\partial \tilde{\rho}_e^l}\\ &+2\omega_{iso}\left({C_{11}}^H - {C_{12}}^H - 2{C_{44}}^H\right)\left(\frac{\partial {C_{11}}^H}{\partial \tilde{\rho}_e^l} - \frac{\partial {C_{12}}^H}{\partial \tilde{\rho}_e^l} - 2\frac{\partial {C_{44}}^H}{\partial \tilde{\rho}_e^l}\right)\\ &+2\omega_{npr}\left(\frac{\nu_{\mathrm{obj}}}{1-\nu_{\mathrm{obj}}}{C_{11}}^H - {C_{12}}^H\right)\left(\frac{\nu_{\mathrm{obj}}}{1-\nu_{\mathrm{obj}}}\frac{\partial {C_{11}}^H}{\partial \tilde{\rho}_e^l} - \frac{\partial {C_{12}}^H}{\partial \tilde{\rho}_e^l}\right)\end{aligned} \tag{4.24}$$

From Equation (2.20) we can have

$$\frac{\partial C_{ij}^H}{\partial \tilde{\rho}_e^l} = \frac{1}{V}\frac{\partial\left({\boldsymbol{U}_i}^T\boldsymbol{K}\boldsymbol{U}_j\right)}{\partial \tilde{\rho}_e^l} = \frac{1}{V}\left(\frac{\partial {\boldsymbol{U}_i}^T}{\partial \tilde{\rho}_e^l}\boldsymbol{K}\boldsymbol{U}_j + {\boldsymbol{U}_i}^T\frac{\partial \boldsymbol{K}}{\partial \tilde{\rho}_e^l}\boldsymbol{U}_j + {\boldsymbol{U}_i}^T\boldsymbol{K}\frac{\partial \boldsymbol{U}_j}{\partial \tilde{\rho}_e^l}\right) \tag{4.25}$$

From the equilibrium using the Lagrange multiplier method to deal with periodic boundary conditions in Equation (4.3), we can rewrite the above equation as Equation (4.26)

$$\begin{cases}\boldsymbol{KU} = \boldsymbol{F} - \boldsymbol{G}^T\boldsymbol{\lambda}\\ \boldsymbol{GU} = \boldsymbol{Q}\end{cases} \tag{4.26}$$

Then differentiating both sides of the above second equation gives

$$\boldsymbol{G}\frac{\partial \boldsymbol{U}}{\partial \tilde{\rho}_e^l} + \frac{\partial \boldsymbol{G}}{\partial \tilde{\rho}_e^l}\boldsymbol{U} = \boldsymbol{G}\frac{\partial \boldsymbol{U}}{\partial \tilde{\rho}_e^l} = \frac{\partial \boldsymbol{Q}}{\partial \tilde{\rho}_e^l} = \boldsymbol{0} \tag{4.27}$$

All degrees of freedom (DOFs) are divided into three groups: DOFs of the fixed node using the superscript *0*, DOFs of the nodes imposed with multi-point constraints using the superscript *m*, and DOFs of the remaining free nodes using the superscript *f*. As mentioned in Section 4.2.1, we can know that $\boldsymbol{U}_i^0$, $\boldsymbol{F}_j^m$, and $\boldsymbol{F}_j^f$ are all zero matrices for the six load cases to calculate $\boldsymbol{C}^H$, and therefore we can derive the following equation:

$$\begin{aligned}\frac{\partial \boldsymbol{U}_i{}^T}{\partial \tilde{\rho}_e^l}\boldsymbol{F}_j &= \frac{\partial \boldsymbol{U}_i^{0\,T}}{\partial \tilde{\rho}_e^l}\boldsymbol{F}_j^0 + \frac{\partial \boldsymbol{U}_i^{m\,T}}{\partial \tilde{\rho}_e^l}\boldsymbol{F}_j^{m\,T} + \frac{\partial \boldsymbol{U}_i^{f\,T}}{\partial \tilde{\rho}_e^l}\boldsymbol{F}_j^{f\,T} \\ &= \boldsymbol{0}^T\boldsymbol{F}_j^0 + \frac{\partial \boldsymbol{U}_i^{m\,T}}{\partial \tilde{\rho}_e^l}\boldsymbol{0} + \frac{\partial \boldsymbol{U}_i^{f\,T}}{\partial \tilde{\rho}_e^l}\boldsymbol{0} = 0\end{aligned} \tag{4.28}$$

Substituting Equation (4.26-4.28) into Equation (4.25) leads to

$$\frac{\partial \boldsymbol{U}_i{}^T}{\partial \tilde{\rho}_e^l}\boldsymbol{K}\boldsymbol{U}_j = \frac{\partial \boldsymbol{U}_i{}^T}{\partial \tilde{\rho}_e^l}\left(\boldsymbol{F}_j - \boldsymbol{G}^T\boldsymbol{\lambda}_j\right) = \frac{\partial \boldsymbol{U}_i{}^T}{\partial \tilde{\rho}_e^l}\boldsymbol{F}_j - \left(\boldsymbol{G}\frac{\partial \boldsymbol{U}_i}{\partial \tilde{\rho}_e^l}\right)^T\boldsymbol{\lambda}_j = 0 - \boldsymbol{0}^T\boldsymbol{\lambda}_j = 0 \tag{4.29}$$

Therefore, Equation (4.25) can be simplified as Equation (4.30), which is the sensitivity of an effective elastic constant with respect to an elemental density.

$$\frac{\partial C_{ij}^H}{\partial \tilde{\rho}_e^l} = \frac{1}{V}\boldsymbol{U}_i{}^T\frac{\partial \boldsymbol{K}}{\partial \tilde{\rho}_e^l}\boldsymbol{U}_j = \frac{1}{V}\left(\boldsymbol{u}_i^{eT}\frac{\partial \boldsymbol{k}^e}{\partial \tilde{\rho}_e^l}\boldsymbol{u}_j^e\right) \tag{4.30}$$

From Equation (4.8), the sensitivity of macroscopic thermal stress vector can be written by

$$\begin{aligned}\frac{\partial \overline{\boldsymbol{\sigma}}_{th}}{\partial \tilde{\rho}_e^l} &= \frac{1}{V}\left(\frac{\partial\left(\boldsymbol{U}_\phi{}^T\boldsymbol{K}\boldsymbol{U}_\theta\right)}{\partial \tilde{\rho}_e^l} - \frac{\partial \boldsymbol{U}_\phi{}^T}{\partial \tilde{\rho}_e^l}\boldsymbol{F}_\theta - \boldsymbol{U}_\phi{}^T\frac{\partial \boldsymbol{F}_\theta}{\partial \tilde{\rho}_e^l}\right) \\ &= \frac{1}{V}\left(\frac{\partial \boldsymbol{U}_\phi{}^T}{\partial \tilde{\rho}_e^l}\boldsymbol{K}\boldsymbol{U}_\theta + \boldsymbol{U}_\phi{}^T\frac{\partial \boldsymbol{K}}{\partial \tilde{\rho}_e^l}\boldsymbol{U}_\theta + \boldsymbol{U}_\phi{}^T\boldsymbol{K}\frac{\partial \boldsymbol{U}_\theta}{\partial \tilde{\rho}_e^l} - \frac{\partial \boldsymbol{U}_\phi{}^T}{\partial \tilde{\rho}_e^l}\boldsymbol{F}_\theta - \boldsymbol{U}_\phi{}^T\frac{\partial \boldsymbol{F}_\theta}{\partial \tilde{\rho}_e^l}\right)\end{aligned} \tag{4.31}$$

As given in Section 4.2.1, $\boldsymbol{U}_\theta^0$, $\boldsymbol{F}_\phi^m$, and $\boldsymbol{F}_\phi^f$ are all zero matrices, and therefore:

$$\begin{aligned}\frac{\partial \boldsymbol{U}_\theta{}^T}{\partial \tilde{\rho}_e^l}\boldsymbol{F}_\phi &= \frac{\partial \boldsymbol{U}_\theta^{0\,T}}{\partial \tilde{\rho}_e^l}\boldsymbol{F}_\phi^0 + \frac{\partial \boldsymbol{U}_\theta^{m\,T}}{\partial \tilde{\rho}_e^l}\boldsymbol{F}_\phi^{m\,T} + \frac{\partial \boldsymbol{U}_\theta^{f\,T}}{\partial \tilde{\rho}_e^l}\boldsymbol{F}_\phi^{f\,T} \\ &= \boldsymbol{0}^T\boldsymbol{F}_\phi^0 + \frac{\partial \boldsymbol{U}_\theta^{m\,T}}{\partial \tilde{\rho}_e^l}\boldsymbol{0} + \frac{\partial \boldsymbol{U}_\theta^{f\,T}}{\partial \tilde{\rho}_e^l}\boldsymbol{0} = 0\end{aligned} \tag{4.32}$$

From Equation (4.26)-(4.28), we can obtain the following equations:

$$\begin{cases} \dfrac{\partial \boldsymbol{U}_\phi{}^T}{\partial \tilde{\rho}_e^l} \boldsymbol{K} \boldsymbol{U}_\theta = \dfrac{\partial \boldsymbol{U}_\phi{}^T}{\partial \tilde{\rho}_e^l} (\boldsymbol{F}_\theta - \boldsymbol{G}^T \boldsymbol{\lambda}_\theta) = \dfrac{\partial \boldsymbol{U}_\phi{}^T}{\partial \tilde{\rho}_e^l} \boldsymbol{F}_\theta - \left(\boldsymbol{G} \dfrac{\partial \boldsymbol{U}_\phi}{\partial \tilde{\rho}_e^l} \right)^T \boldsymbol{\lambda}_\theta = \dfrac{\partial \boldsymbol{U}_\phi{}^T}{\partial \tilde{\rho}_e^l} \boldsymbol{F}_\theta \\ \dfrac{\partial \boldsymbol{U}_\theta{}^T}{\partial \tilde{\rho}_e^l} \boldsymbol{K} \boldsymbol{U}_\phi = \dfrac{\partial \boldsymbol{U}_\theta{}^T}{\partial \tilde{\rho}_e^l} (\boldsymbol{F}_\phi - \boldsymbol{G}^T \boldsymbol{\lambda}_\phi) = \dfrac{\partial \boldsymbol{U}_\theta{}^T}{\partial \tilde{\rho}_e^l} \boldsymbol{F}_\phi - \left(\boldsymbol{G} \dfrac{\partial \boldsymbol{U}_\theta}{\partial \tilde{\rho}_e^l} \right)^T \boldsymbol{\lambda}_\phi = 0 \end{cases} \tag{4.33}$$

Substituting Equation (4.33) into Equation (4.31) gives

$$\begin{aligned} \frac{\partial \overline{\boldsymbol{\sigma}}_{th}}{\partial \tilde{\rho}_e^l} &= \frac{1}{V} \left(\frac{\partial \boldsymbol{U}_\phi{}^T}{\partial \tilde{\rho}_e^l} \boldsymbol{F}_\theta + \boldsymbol{U}_\phi{}^T \frac{\partial \boldsymbol{K}}{\partial \tilde{\rho}_e^l} \boldsymbol{U}_\theta - \frac{\partial \boldsymbol{U}_\phi{}^T}{\partial \tilde{\rho}_e^l} \boldsymbol{F}_\theta - \boldsymbol{U}_\phi{}^T \frac{\partial \boldsymbol{F}_\theta}{\partial \tilde{\rho}_e^l} \right) \\ &= \frac{1}{V} \left(\boldsymbol{U}_\phi{}^T \frac{\partial \boldsymbol{K}}{\partial \rho} \boldsymbol{U}_\theta - \boldsymbol{U}_\phi{}^T \frac{\partial \boldsymbol{F}_\theta}{\partial \rho} \right) \end{aligned} \tag{4.34}$$

Based on Equation (4.4), (4.30), and (4.34), we can finally obtain the sensitivity of thermal expansion coefficients with respect to an elemental density, based on the energy-based homogenization method:

$$\begin{aligned} \frac{\partial \boldsymbol{a}^H}{\partial \tilde{\rho}_e^l} &= -\frac{\partial \left(\boldsymbol{C}^{H^{-1}} \right)}{\partial \tilde{\rho}_e^l} \overline{\boldsymbol{\sigma}}_{th} - \boldsymbol{C}^{H^{-1}} \frac{\partial \overline{\boldsymbol{\sigma}}_{th}}{\partial \tilde{\rho}_e^l} = \boldsymbol{C}^{H^{-1}} \frac{\partial \boldsymbol{C}^H}{\partial \tilde{\rho}_e^l} \boldsymbol{C}^{H^{-1}} \overline{\boldsymbol{\sigma}}_{th} - \boldsymbol{C}^{H^{-1}} \frac{\partial \overline{\boldsymbol{\sigma}}_{th}}{\partial \tilde{\rho}_e^l} \\ &= -\boldsymbol{C}^{H^{-1}} \left(\frac{\partial \boldsymbol{C}^H}{\partial \tilde{\rho}_e^l} \boldsymbol{a}^H + \frac{\partial \overline{\boldsymbol{\sigma}}_{th}}{\partial \tilde{\rho}_e^l} \right) \end{aligned} \tag{4.35}$$

After obtaining the sensitivities based on finite element analysis results, the method of moving asymptotes [202] can be adopted to solve the constrained optimization design problem.

4.3. Numerical results

In the numerical example, a 3D isotropic NPR-ZTE microstructure is topologically designed to demonstrate the effectiveness of the proposed optimization design method. In this section, we will show a high-resolution design from different aspects and individual geometries of two constituent materials. Based on the computational homogenization method, we studied the effective properties of the optimized microstructure to validate its auxetic and ZTE properties. We also visualize the spatial variation of its elastic properties to quantitatively showcase its elastic isotropy. Moreover, we conduct numerical analyses for a lattice structure to verify the macroscopic deformation behaviors of the optimized design.

4.3.1. An isotropic NPR-ZTE microstructure

For the proposed multi-material topology optimization method, three constituent materials are distributed in the design domain. In this chapter, we used Nickel and Invar as the two solid phase materials, the properties of which are listed in Table 4.1. An artificial weak material is also assigned to voids.

Table 4.1. Properties of constituent materials

	Nickel	Invar	Void
Young’s modulus (GPa)	200	150	2.0e-7
Poisson’s ratio	0.31	0.31	0.31
Thermal expansion coefficient (1e-6/°F)	7.3	0.8	7.3
Density (Kg/m^3)	8890	8100	0

Based on these constituent materials, a multi-material microstructure is finally obtained though the optimization design, as shown in Figure 4.3a. Here, the green part is filled with Nickel, while the blue part is filled with Invar. The artificial void phase material is not included in this final design. It is achieved by gradually removing regions full filled with void phase material from the design domain. Topology optimization will be conducted on the updated and remeshed design domain, which uses the last optimized design as the initial guess. Since the design domain is approaching the solid part step by step, a final optimized design with refined geometric surfaces can be obtained as shown in Fig. 4.3, which fully illustrates the effectiveness of this proposed method. Evolution histories are not given for these multiple times of topology optimization for the brevity.

Different views of the topologically optimized microstructure and individual geometries of two solid materials are also shown in Figure 4.3b and Figure 4.3c. We can see that the microstructure is a composite structure which has a geometric cubic symmetry and contains a smaller portion of Invar. Assuming that the design domain for topology optimization is a 1mm × 1mm × 1mm cube, the geometrical volume of the optimized microstructure is 0.29 mm^3, while the volume of Nickel is 0.241 mm^3 and the volume of Invar is 0.049 mm^3. Therefore, the effective mass density of the microstructure is about 2537 Kg/m^3.

Fabrication of such advanced lattice structures with multiple metallic materials using current industrial standard additive manufacturing equipment is challenging, but it is possible due to the recent rapid advancement of additive manufacturing techniques. Over the past few years, selective laser melting based techniques have been developed to manufacture multi-material structures with different metals mostly distributed along a specific direction, e.g., the vertical [203] or the horizontal [204] direction. A modified selective laser melting technique, which was combined with point-by-point powder dispensing and selective material removal, was also developed to deposit multiple metals both within the same layer and across different layers [205]. A selective powder deposition technique was invented to deposit up to three different metals simultaneously in a single layer [206]. Direct energy deposition techniques with multiple nozzles have also been developed for depositing multiple metals with full spatial distributions [207].

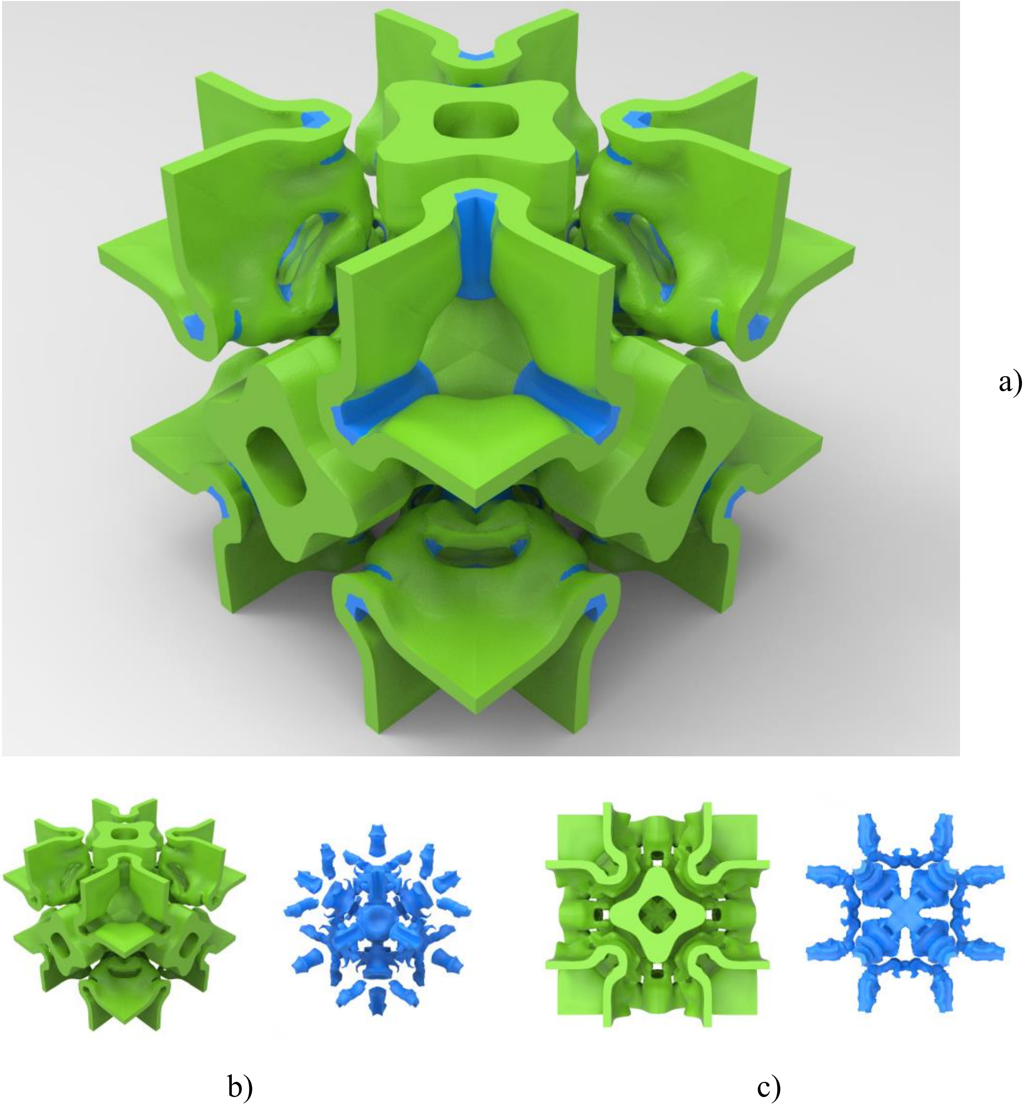

Figure 4.3. An isotropic NPR-ZTE microstructure (Note: rendered effect): a) Composite microstructure; b) Isometric view of two constituents; c) Top view of two constituents

4.3.2. Effective material properties

To calculate the effective properties more accurately, we remove the part of artificial weak material from the voids in the design domain and only re-mesh the solid parts. The model used for the computational homogenization will then has about 4.88 million solid elements and 2.81 million degrees of freedom, which is shown in Figure 4.4 with a zoom in view indicated by the green color dash box.

The effective elastic stiffness matrix of the microstructure calculated by the computational homogenization is given in Table 4.2. The corresponding elastic properties in three averaging schemes are also calculated and shown in Table 4.3. For theories and formulas of averaging schemes, the readers can refer to [198]. We can see that no matter which averaging scheme is used, the optimized multi-material microstructure has an effective Young’s modulus 2.6084 GPa and a negative Poisson’s ratio -0.4318.

We further studied the spatial dependence of Young’s modulus, shear modulus, and Poisson’s ratio as 3D surfaces, which are shown in Figure 4.5. Besides the graphical representations of directional elastic properties, we also quantitatively compare their extreme values as listed in Table 4.4. For each directional property, a measure of anisotropy is defined as the ratio of its maximum value to its minimum value. We can find that the surfaces of directional elastic properties are almost spheres, and the ratios of extreme values are all nearly one. Therefore, the microstructure designed in this chapter are elastically isotropic.

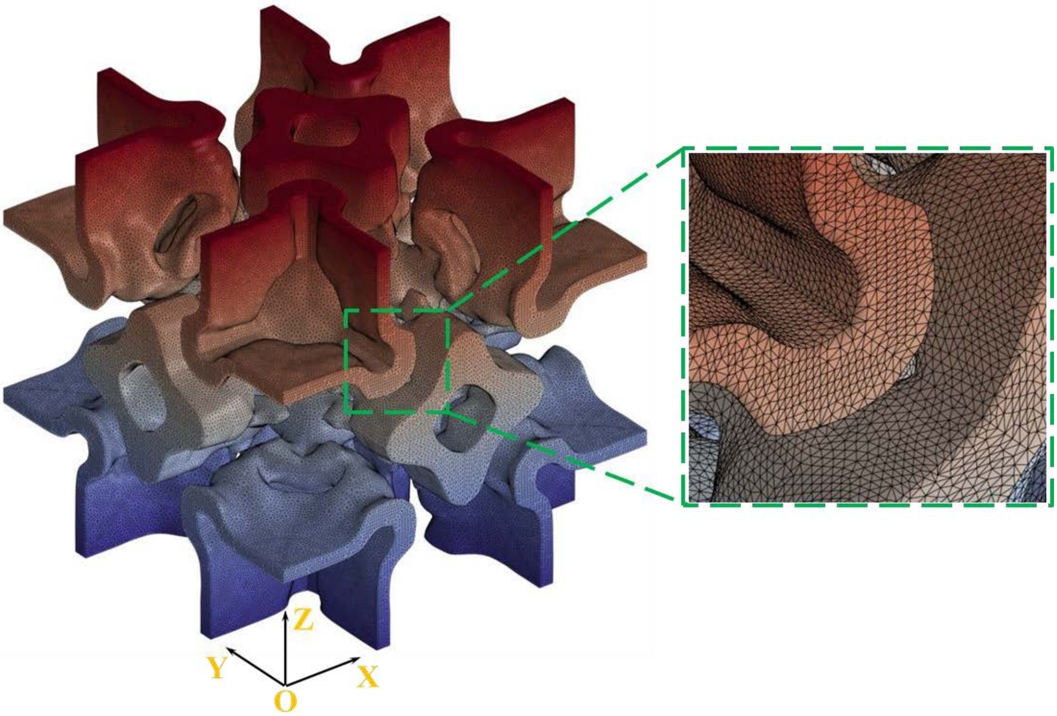

Figure 4.4. Finite element mesh model

Table 4.2. Effective elastic stiffness matrix (GPa)

$$\begin{bmatrix} 3.5554 & -1.0779 & -1.0779 & 0.0000 & 0.0000 & 0.0000 \\ -1.0779 & 3.5554 & -1.0779 & 0.0000 & 0.0000 & 0.0000 \\ -1.0779 & -1.0779 & 3.5554 & 0.0000 & 0.0000 & 0.0000 \\ 0.0000 & 0.0000 & 0.0000 & 2.2815 & 0.0000 & 0.0000 \\ 0.0000 & 0.0000 & 0.0000 & 0.0000 & 2.2815 & 0.0000 \\ 0.0000 & 0.0000 & 0.0000 & 0.0000 & 0.0000 & 2.2815 \end{bmatrix}$$

Table 4.3. Average elastic properties

	Voigt scheme	Reuss scheme	Hill scheme
Bulk modulus (GPa)	0.4665	0.4665	0.4665
Shear modulus (GPa)	2.2955	2.2954	2.2955
Young's modulus (GPa)	2.6084	2.6084	2.6084
Poisson's ratio	-0.4318	-0.4318	-0.4318

We further studied the spatial dependence of Young's modulus, shear modulus, and Poisson's ratio as 3D surfaces, which are shown in Figure 4.5. Besides the graphical representations of directional elastic properties, we also quantitatively compare their extreme values as listed in Table 4.4. For each directional property, a measure of anisotropy is defined as the ratio of its maximum value to its minimum value. We can find that the surfaces of directional elastic properties are almost spheres, and the ratios of extreme values are all nearly one. Therefore, the microstructure designed in this chapter are elastically isotropic.

Table 4.4. Extreme values of directional elastic properties

	Minimum value	Maximum value	Anisotropy ratio
Shear modulus (GPa)	2.2815	2.3166	1.0154
Young’s modulus (GPa)	2.6024	2.6175	1.0058
Poisson’s ratio	-0.4351	-0.4289	0.9857

For a comparison, three topologically optimized auxetic microstructures from [194, 195, 208] are selected to analyze their directional Poisson’s ratios. These microstructures are shown in Figure 4.6, and their surfaces of Poisson’s ratios are shown in Figure 4.7. We can see that they only exhibit negative Poisson’s ratios in narrow ranges of loading directions and even exhibit a large positive Poisson’s ratio in some specific directions.

The effective CTE values of the microstructure calculated by using the computational homogenization are listed in Table 4.5. Compared with the constituent materials, the microstructure has a negative isotropic thermal expansion coefficient -2.6247e-9/°F, the absolute value of which is relatively very small and can be approximately regarded as zero.

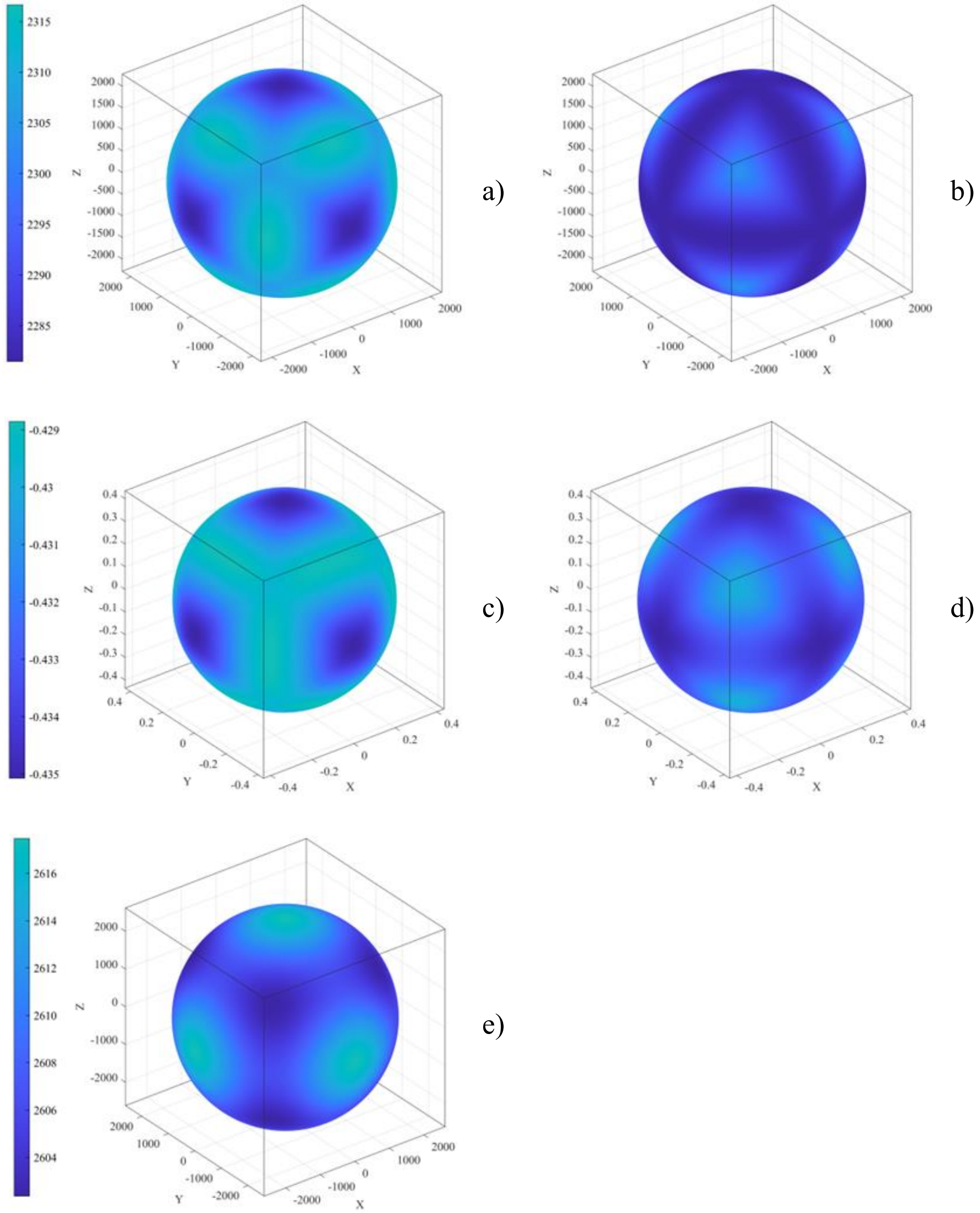

Figure 4.5. Surfaces of effective material properties: a) maximum shear modulus; b) minimum shear modulus; c) maximum Poisson’s ratio; d) minimum negative Poisson’s ratio; e) Young’s modulus (Unit for shear modulus and Young’s modulus: MPa)

We will further analyze and compare effective properties of a single material microstructure when fully filled with only Nickel or Invar, which are listed in Table 4.6. Since they are still isotropic, only the Hill scheme of average elastic properties is given here for the sake of simplicity. From the results given in Table 4.6, we can find that the composite microstructure has a much smaller thermal expansion coefficient than the microstructure filled with pure Nickel or Invar. Furthermore, it can be found that the mass density, bulk modulus, shear modulus, and Young's modulus of the composite microstructure are between that of the Nickel and Invar.

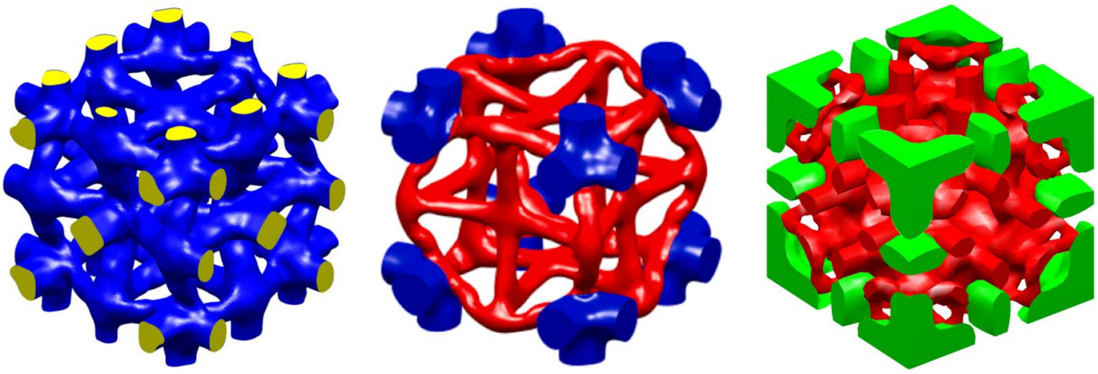

a) b) c)

Figure 4.6. Non-isotropic auxetic microstructures (Reprinted from [194, 195, 208])

If intermediate elemental densities of this topologically optimized design are remained, such a microstructure without post-processing has a Hill average Young's modulus 2.5892 GPa, a Hill average Poisson's ratio -0.4300, and a nearly zero CTE value -2.7394e-9/°F. The relative errors between them and values in Table 4.4-4.5 are respectively 0.74%, 0.42%, and 4.37%. Since two CTE values are nearly zero, their absolute error is actually very small. Therefore, the post-processed design has almost the same performance when compared to the original optimized design with intermediate densities.

Table 4.5. Effective coefficients of thermal expansion (Unit: 1e-9/°F)

α_{11}	α_{22}	α_{33}	α_{23}	α_{13}	α_{12}
-2.6247	-2.6247	-2.6247	0.0000	0.0000	0.0000

4.3.3. Numerical verifications using a lattice structure

To further verify the auxetic and ZTE behaviors at the macroscopic level, we conduct linear static finite element analysis of a lattice structure, which is periodically assembled by using $6 \times 6 \times 6$ microstructures. This composite lattice structure is shown in as shown in Figure 4.8a.

For the verification of its auxetic behavior, the lattice structure is uniaxially compressed, while it is free in other directions. For the verification of its ZTE behavior, roller boundary conditions are imposed on all out surfaces of the lattice structure to simulate surrounding structures which restrict its normal thermal expansion when subject to a temperature increase. To reduce the computational cost, we only use one eighth of the total structure for finite element analysis by utilizing geometric symmetry, e.g., the part given in Figure 4.8b. This smaller lattice structure is periodically assembled by $3 \times 3 \times 3$ microstructures.

In the load case of the auxetic behavior, a prescribed displacement along the negative Z-direction is imposed on nodes on the plane Z=3mm, while roller boundary conditions are imposed on nodes, respectively, on the planes X=0, Y=0, and Z=0. In the load case of ZTE, roller boundary conditions are imposed on all outermost nodes, and there is a 10°F increase in temperature. The mesh of this lattice structure is assembled by the microstructures as shown in Figure 4.4 with coincident nodes merged. It is a large-scale mesh with about 131.82 million solid elements and 75.21 million degrees of freedom.

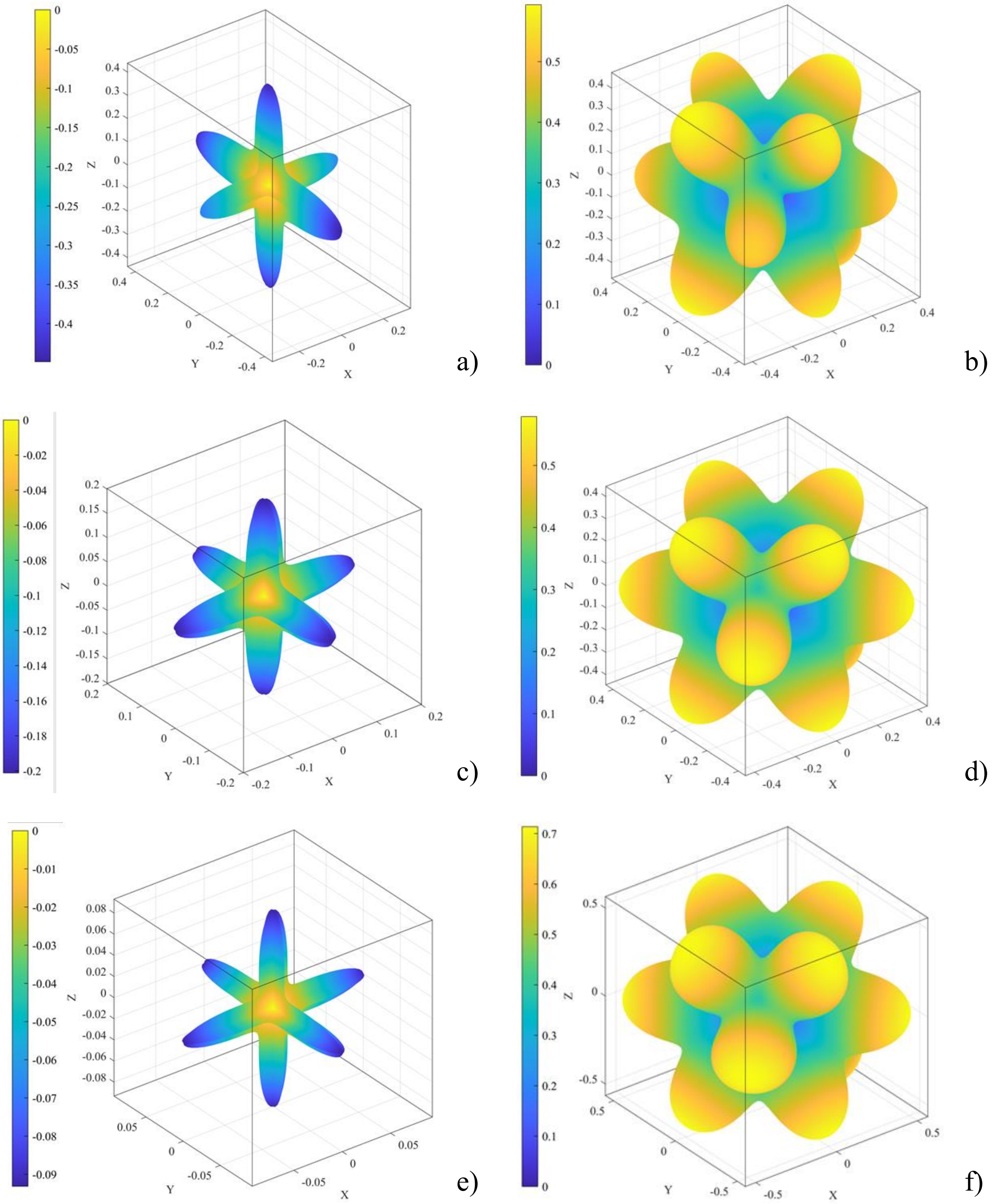

Figure 4.7. Surfaces of Poisson's ratios for non-isotropic auxetic microstructures in [193, 194, 207]: Surfaces of minimum negative Poisson's ratios for three microstructures are respectively given in a), c), and e); Surfaces of maximum positive Poisson's ratios for three microstructures are respectively shown in b), d), and f)

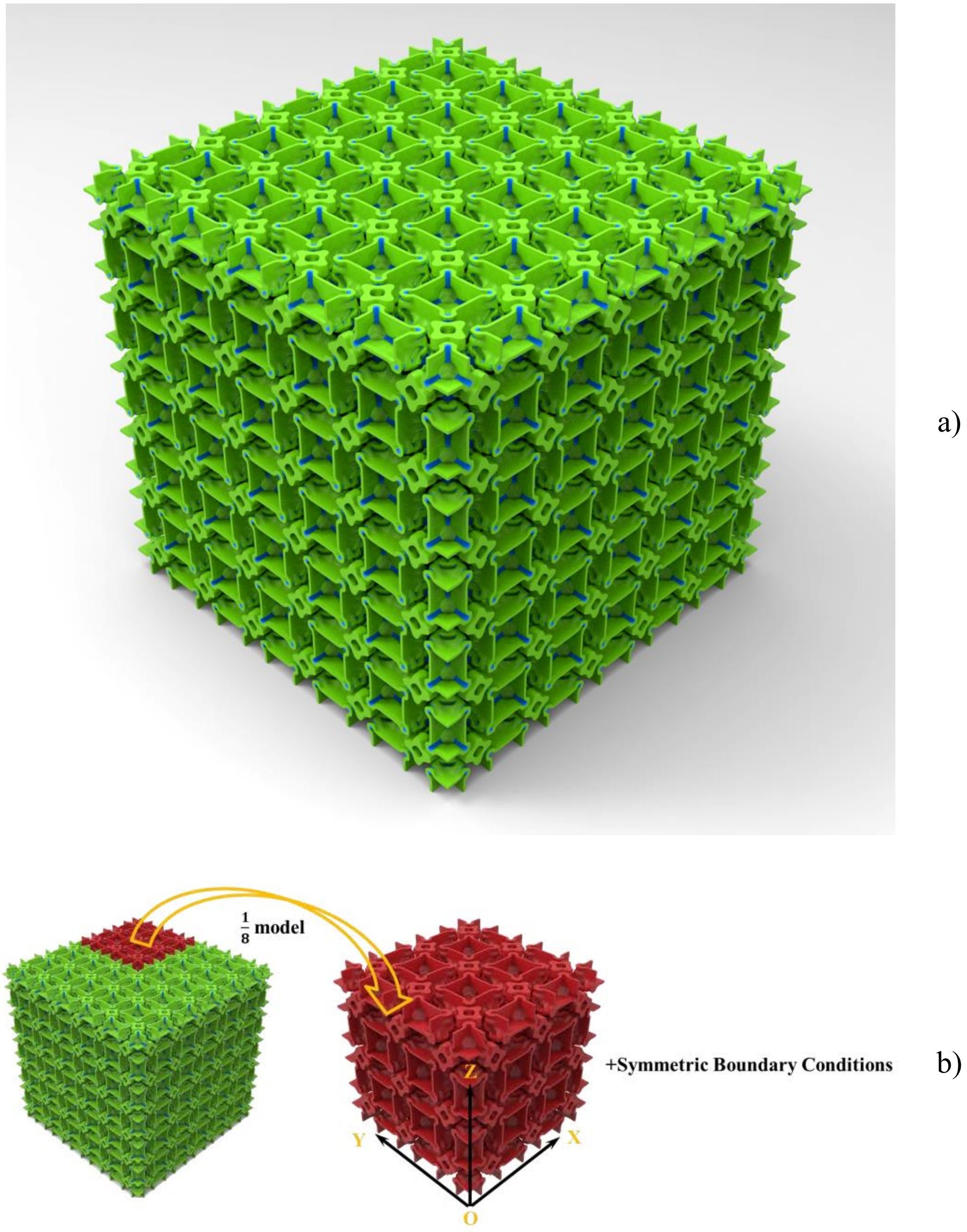

Figure 4.8. Composite lattice structure (Note: rendered effect): a) Entire lattice structure periodically assembled by 6 × 6 × 6 microstructures; b) One eighth of the lattice structure (in red color) used for finite element analysis

For the load case of the auxetic behavior, the directional displacement results of the lattice structure are shown in Figure 4.9a-c. Moreover, the deformed and undeformed shapes are respectively plotted on the planes X=3mm and Y=3mm to facilitate the observation of its auxetic behavior. As shown in Figure 4.9d and Figure 4.9e, for the undeformed shapes, only outlines in black color are plotted, while the deformed shapes are plotted as contours to represent the ratio of vertical to horizontal displacements. From these displacement results, we can find that the lattice structure exhibits an auxetic behavior in the horizontal directions when it is uniaxially compressed in the vertical direction. The negative ratio of horizontal to vertical displacements on the right and front faces varies from -0.40 to -0.48, which is slightly different from the effective Poisson's ratio -0.43 due to the boundary effect of the lattice structure. When the lattice structure consists of more microstructures, the macroscopic behavior of the lattice structure should be closer to the homogenized behavior under the periodic boundary conditions.

For the load case of the ZTE behavior, we are concerned with the total reaction forces with the surrounding structures. Therefore, the displacement results will not be shown here for the sake of simplicity. For this load case, three different finite element analyses are conducted for comparison purpose, in which the lattice structures are respectively

Table 4.6. Comparison of effective properties when filled with different materials

	Nickel	Invar	Optimized composite
Bulk modulus (GPa)	0.5476	0.4107	0.4665
Shear modulus (GPa)	2.5709	1.9282	2.2955
Young's modulus (GPa)	3.0068	2.2551	2.6084
Poisson's ratio	-0.4152	-0.4152	-0.4318
Thermal expansion coefficient (1e-6/°F)	7.3	0.8	-0.0026
Mass density (Kg/m^3)	2576	2347	2537

Table 4.7. Reaction forces of lattice structures filled with different materials (Unit: N)

		Nickel	Invar	Optimized composite
Nodes on the plane X=3mm	F_x	-1.07929	-0.08871	0.00066
	F_y	0.00000	0.00000	0.00000
	F_z	0.00000	0.00000	0.00000
Nodes on the plane Y=3mm	F_x	0.00000	0.00000	0.00000
	F_y	-1.07931	-0.08871	0.00027
	F_z	0.00000	0.00000	0.00000
Nodes on the plane Z=3mm	F_x	0.00000	0.00000	0.00000
	F_y	0.00000	0.00000	0.00000
	F_z	-1.07931	-0.08871	0.00030

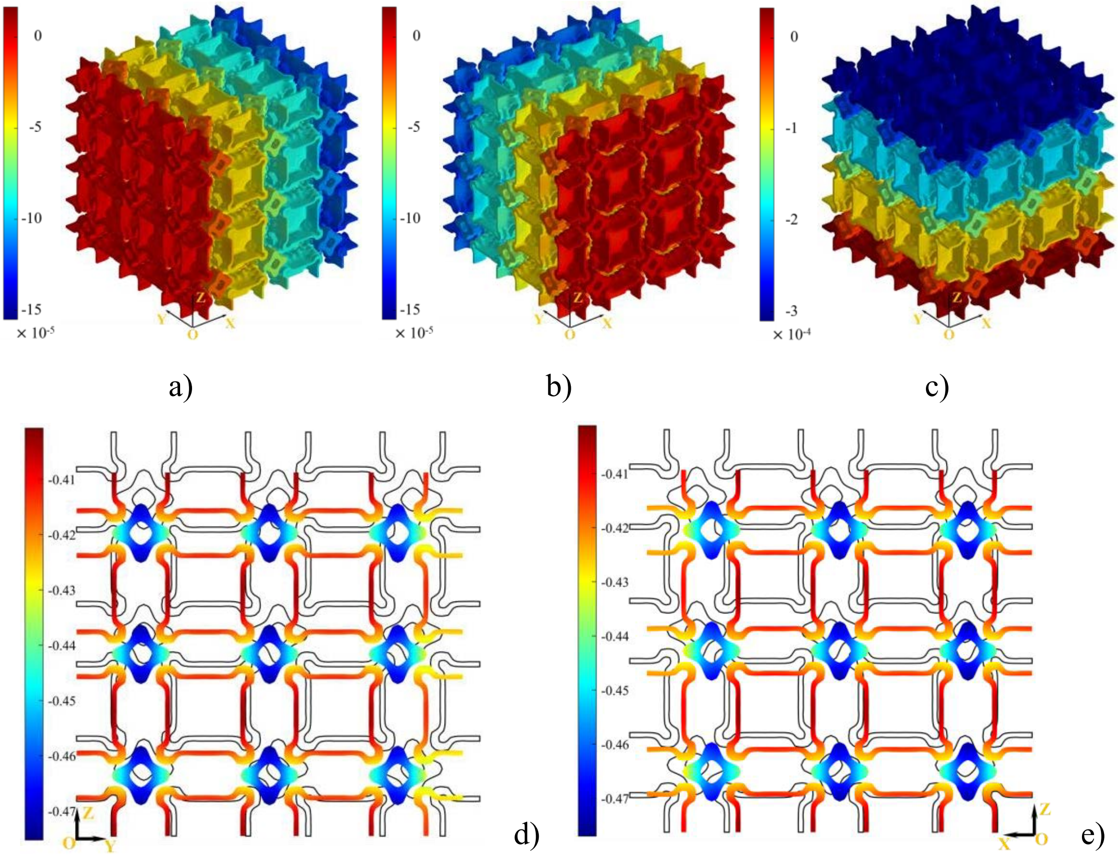

a) b) c)

d) e)

Figure 4.9. Displacement results in the NPR load case: a) Displacements in the X-direction; b) Displacements in the Y-direction; c) Displacements in the Z-direction; d) Negative ratios of displacements in the X-direction to displacements in the Z-direction for nodes on the plane X=3mm; e) Negative ratios of displacements in the Y-direction to displacements in the Z-direction for nodes on the plane Y=3mm

two-phase, single-phase with Nickel, and single-phase with Invar. The reaction force results are listed in Table 4.7. It can be found that even when compared with Invar, an alloy is well-known to have a small thermal expansion coefficient, the normal reaction forces of the composite lattice structure are about 295 times smaller. In other words, the designed lattice structure can be considered to apply nearly zero reaction forces to its surrounding structures when subjected to a temperature change, which demonstrates that the designed microstructure has a nearly zero effective thermal expansion.

4.4. Conclusion

This work has developed a systematic design method to find novel 3D isotropic NPR-ZTE microstructures. A new augmented mathematical optimization formulation is established by incorporating multiple quadratic penalty terms into the objective function to simultaneously meet three design criteria, i.e., elastic isotropy, negative Poisson's ratios, and zero thermal expansion. Moreover, the objective function can also ensure the stiffness of the optimized design. In the proposed method, a multi-material topology optimization method considering a geometric cubic symmetry constraint is used for the design problem. The element density clustering is imposed to guarantee that every intermediate design during the optimization has at least elastic cubic symmetry. The effective elastic stiffness matrix and thermal expansion coefficients are calculated by the energy-based homogenization technique based on finite element analysis.

A novel isotropic microstructure with both negative Poisson's ratios and zero thermal expansion has been found to demonstrate the effectiveness of the proposed design method. As an example, this 3D NPR-ZTE microstructure has a geometric cubic symmetry and consists of Nickel and Invar as constituent materials. Since surfaces of directional elastic properties are almost spheres and the ratios of extreme property values are all nearly one, this microstructure is elastically isotropic. Numerical analyses for a lattice structure are conducted to verify its macroscopic auxetic and ZTE behaviors. The results show that the lattice structure shrinks in the horizontal directions when it is uniaxially compressed in the vertical direction. The lattice structure also applies nearly zero reaction forces to its surrounding structures under a temperature change.

Chapter 5 Design of Mechanical Metamaterials with Tunable Double-negative Isotropic Properties

5.1. Introduction

This chapter is a modified version of the journal paper titled "Multifunctional mechanical metamaterials with tunable double-negative isotropic properties", which was published in *Materials & Design* (Volume 232, 112146).

As mentioned in Chapter 4, most of common materials have positive CTE values. Only a minority of materials exhibit negative thermal expansion (NTE), which include metal oxides [209], zeolites [210], and metal-organic frameworks [211], etc. As illustrated in Figure 4.1, these materials contract upon heating and expand when cooled, which are opposite to PTE materials. NTE materials can be used to compensate the thermal deformation of PTE materials and help tailor the overall thermal expansion of composite structures to specific positive, zero, or even negative values. This can be particularly useful for structures subject to significant temperature variations or thermal cycling, e.g., satellites and heat sinks, which usually suffer from thermal stress problems and increasing probability of structural failure due to mismatch thermal expansion of their constituent materials. For instance, the Cu/ZrW2O8 composite can be used for heat sinks in electronic devices to reduce the thermal expansion mismatch with silicon chips [212]. The use of NTE materials as thermal-expansion compensators can find a wide range of industrial applications, e.g., low-temperature sensors [213], fiber optic systems [214], astronomical telescope mirrors [215], and thermoelectric converters

[216]. In composites, they can reduce the residual stress caused by thermal mismatch of different components, leading to improved durability and performance.

Natural NTE materials are indeed rare and often have limitations in their properties, which has led to increased research interests on artificially engineered materials with unusual thermal expansion properties. As listed in Figure 5.1, by carefully designing the microstructure of a composite material and selecting appropriate constituent materials, achieving a desired NTE or ZTE value becomes possible, even if the constituent materials themselves have positive CTE values. This is because the thermal expansion behavior of a composite material is decided not only by the CTE of the constituent materials but also their arrangement and the relative proportions of each material. These materials can possess multiple benefits when compared to natural NTE materials, including greater tunability and the ability to be produced on different scales. In 1996, Lakes [217] proposed a 2D cellular solid with curved bi-layer ribs that can exhibit unbounded values of CTE, where each rib is made of two bonded layers of materials with dissimilar CTE values. After that, several microstructures with bi-layer ribs were reported to exhibit NTE, e.g., [218-222]. In 2005, some works [223, 224] developed strut-based microstructures that exhibit NTE along specific directions. A variety of strut-based microstructures that exhibit unusual thermal expansion properties have been found over the past twenty years, e.g., [225-235]. There are also some special types of architected metamaterials possessing unusual thermal expansion properties, such as multi-layered metal lattices [236], origami metamaterials with bi-layer plates [237], and kirigami-inspired hierarchical metamaterials [238]. While there have been successful designs of metamaterials with negative thermal expansion, many of them have relied on a few existing architectures using empirical or intuitive design approaches. These approaches may limit the exploration of novel metamaterial architectures with even more unique and desirable properties.

As mentioned before, auxetic metamaterials are another type of widely studied metamaterials exhibiting counterintuitive mechanical deformation behaviors. Nowadays, the demands of modern high-precision mechanical equipment necessitate the utilization of a combination of these types of deformations, as well as customized and isotropic properties. While for a solid material, properties of NPR and NTE/ZTE are not mutually exclusive. The combination of NTE and NPR in mechanical metamaterials can offer a greater variety of potential applications owing to a unique combination of the multiple negative properties, when compared to those metamaterials only having NTE or NPR. It can facilitate the invention of new sensors, actuators, soft robotics, and wearable technologies. For example, the negative thermal expansion can be utilized for temperature sensing and actuation, while the negative Poisson’s ratio can provide enhanced flexibility and adaptability to the material. Moreover, such multifunctional metamaterials can potentially be used in the construction of high-performance composites and protective materials, as they can offer improved resistance to thermal and mechanical stresses.

Hence, the development of mechanical metamaterials with both NTE and NPR has the potential to unlock new avenues for materials by design, and to revolutionize a wide range of industries. Although several works have attempted to develop metamaterials that can exhibit both NTE and NPR properties [220-222, 233-235], they have been designed using empirical design motifs, which limits the discovery of new designs. To overcome this limitation, there has been a growing fascination with developing advanced numerical design methods that can systematically and generatively create multifunctional metamaterials. These methods can be optimized to achieve specifically tailored multiple properties and explore a much wider design space.

Nowadays, topology optimization has proven to be an essential tool to unlock distinctive advantages offered by additive manufacturing techniques for allowing fabrications of structures with intricate shapes and features. It provides a means for designing and optimizing microstructural architectures to achieve counterintuitive deformation, such as NPR and NTE. Sigmund and Torquato [239] first utilized a density-based method to create composites with extremal thermal expansion behavior. Subsequently, various topology optimization techniques were employed to generate a couple of auxetic metamaterials exhibiting either zero or negative CTE values. [240-243], but they are limited to 2D designs. In Chapter 4, a continuum topology optimization method is developed to design 3D multi-material microstructures that can simultaneously exhibit elastic isotropy, NPR, and ZTE.

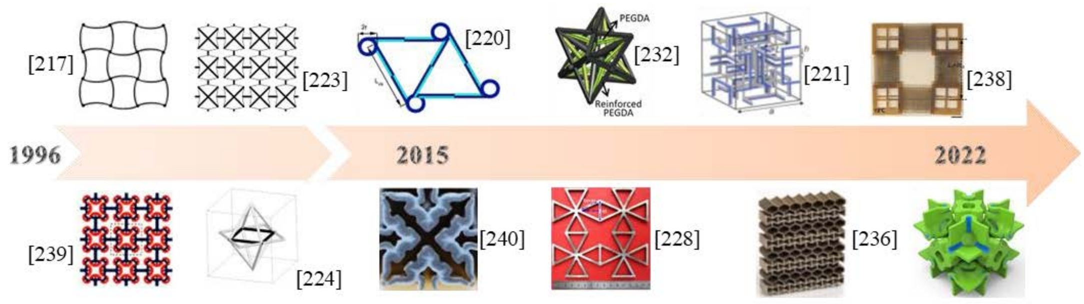

Figure 5.1. Metamaterials with unusual thermal expansion properties

However, microstructures designed using continuum topology optimization methods often result in highly complex geometries and large material interfaces, making them difficult to be converted into parametric models and fabricated even with most up-to-date additive manufacturing methods. Additionally, continuum topology optimization methods typically necessitate large-scale finite element models to describe high-resolution lightweight designs. This is computationally prohibitive and impractical for generating a collection of 3D microstructures with a broad spectrum of tunable property values. In recent years, one of the significant challenges in materials by design is achieving tunable performance by using a single microstructure. Although the design method proposed in Chapter 4 has higher ability to fully explore potential designs with complex geometries, it may be not suited for designing microstructures with parametric simple geometries and tunability of properties. However, strut-based microstructures designed in Chapter 3 possess good tunabilities of effective material properties by changing cross-sections of struts. It inspires the study in this chapter to develop a generic and rational design method for the discovery of 3D strut-based lattice metamaterials that simultaneously possess elastic isotropy, tunable thermal expansion, and tunable auxeticity. We will develop a discrete topology optimization method using a multi-material ground structure to create such multifunctional and tunable metamaterials with simple microstructural geometries and supports for multiple combinations of constituent materials.

5.2. Computational design method

This section will firstly develop a discrete topology optimization method based on a 3D multi-material strut-based ground structure. Then, an optimization formulation is established for designing microstructures of lattice materials with desired double-negative properties.

5.2.1. Multi-material ground structure

By properly selecting constituent materials, designing microstructural geometries, and determining the spatial distributions of multiple materials, novel lattice metamaterials with unconventional properties can be discovered using topology optimization methods. However, most of studies on multi-material topology optimization of metamaterials are using continuum-based methods [239-243]. The complex geometries produced by continuum topology optimization methods may impede their practical manufacturing and applications. Here, we propose a discrete topology optimization method based on a 3D multi-material ground structure that consists of beams and has the geometric cubic symmetry.

The procedure of generating a ground structure with geometric cubic symmetry is illustrated in Figure 5.2a, which is the same as we proposed in Section 3.2.1. To further describe a bi-material candidate design, we need to define three algorithm parameters and assign two types of design variables. The algorithm parameters are described as follows. Firstly, we should determine n_{gp}, the number of grid points along a principal axis, which is 5 in this work. As shown in Figure 5.2b, with a larger n_{gp}, the ground structure consists of more bars and therefore can describe more complex topologies. However, at the same time, it has more design variables that will increase computational cost. In this work, we use $n_{gp} = 5$, since a $5 \times 5 \times 5$ Cartesian point grid is sufficient for constructing a complicated ground structure as given in Figure 5.2a. Secondly, we will decide n_{b1} and n_{b2}, the number of active bars composed of the first or second type of constituent material in the primary ground substructure. Since the ground structure is geometrically cubic symmetric, small values for these two parameters will be employed to create a bi-material design. In this work, we use n_{b1} and n_{b2} that are no larger than 5. The first type of design variables is to determine which bars are active in the final design, which consists of index numbers of active bars in the primary ground substructure. The first n_{b1} and the latter n_{b2} integer variables are, respectively, related to active bars composed of the first type and the second type of constituent material. The second type of design variables is the cross-sectional radius of each active bar in the primary ground substructure, which is continuous in a given range. We can know that the number of total design variables is $n_{var} = 2(n_{b1} + n_{b2})$.

Based on the proposed ground structure, algorithm parameters, and design variables, a variety of strut-based bi-material microstructures with relatively simple geometries can be described, which can ease the fabrication and tunability of material properties. For instance, as illustrated in Figure 5.2c, a bi-material oct-truss microstructure with ZTE [200] can be described by the proposed ground structure. By defining the ground structure as a bi-material system, the design can have unusual thermal expansion properties due to the structural interaction of struts made of two materials with dissimilar CTE values. This multi-material ground structure allows for a wider range of tunable properties than a single-material system. It should be noted that in this research, different materials within the microstructure are assumed to be perfectly bonded, without considering effects induced by joints and graded interfaces.

5.2.2. Mathematical optimization formulation

We employ the computational homogenization method [152] to determine the effective elastic tensor $\boldsymbol{C}^H$ and the effective CTE tensor $\boldsymbol{\alpha}^H$ of a periodic composite microstructure. To simulate slender and cylindrical bars within the ground structure, we utilize beam elements, which yield sufficiently accurate finite element results. Note that inactive bars in the ground structure are not removed from the finite element analysis to prevent a singular global stiffness matrix. These bars are composed of the first type of constituent material, and they are assigned an identical value for their cross-sectional radius, which is small enough to have a negligible impact on the homogenized results.

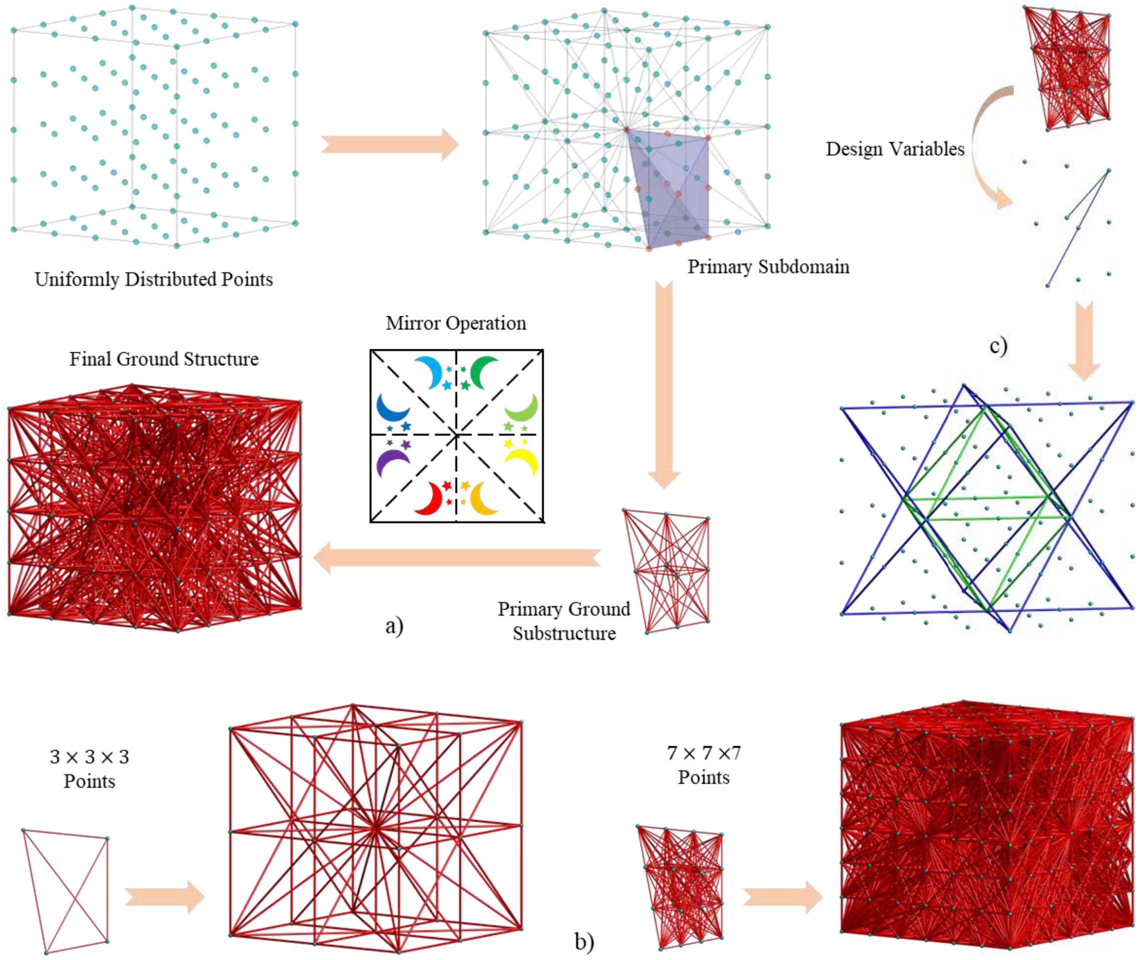

Figure 5.2. Multi-material Ground structure with the geometric cubic symmetry: a) Generation procedure; b) Ground structures respectively with $n_{gp} = 3$ and $n_{gp} = 7$; c) A bi-material example

During the calculation of homogenized CTE value, different from the method using solid elements in Chapter 4, the periodic boundary condition in Equation (2.23) should also be considered in the finite element analysis using beam elements. Moreover, for assembling $\boldsymbol{F}_\theta$ in Equation (4.8), the elemental thermal force of a 3D cylindrical beam is defined in the local coordinate system as follows:

$$\boldsymbol{F}_\theta^e = \begin{bmatrix} -E\alpha\Delta TA & 0 & 0 & 0 & 0 & 0 \\ E\alpha\Delta TA & 0 & 0 & 0 & 0 & 0 \end{bmatrix}^T \tag{5.1}$$

where E and α are respectively the Young's modulus and the CTE of the constituent material, ΔT and A are respectively the temperature change and the cross-sectional area of the beam.

The following mathematical optimization formulation is established for designing multifunctional metamaterials:

$$\text{Find:} \quad \boldsymbol{\rho} = [\rho_1 \quad \cdots \quad \rho_{n_{b1}} \quad \rho_{n_{b1}+1} \quad \cdots \quad \rho_{n_{b1}+n_{b2}} \quad \rho_{n_{b1}+n_{b2}+1} \quad \cdots \quad \rho_{n_{var}}]$$

$$\text{Min:} \quad f(\boldsymbol{\rho}) = \omega_{iso}\left(\frac{\left(C_{11}{}^{H}(\boldsymbol{\rho}) - C_{12}{}^{H}(\boldsymbol{\rho})\right)}{2C_{44}{}^{H}(\boldsymbol{\rho})} - 1\right)^2 + \omega_{pr}\left(\frac{C_{12}{}^{H}(\boldsymbol{\rho})}{C_{11}{}^{H}(\boldsymbol{\rho}) + C_{12}{}^{H}(\boldsymbol{\rho})} + 1\right)^2 + \omega_{cte}\frac{\alpha_{11}{}^{H}(\boldsymbol{\rho})}{\alpha_{ref}} + \omega_{geo}\left(N_{ins}(\boldsymbol{\rho}) + N_{isol}(\boldsymbol{\rho})\right) \tag{5.2}$$

where $\boldsymbol{\rho}$ is the vector of design variables that has been introduced in Section 5.2.1, f is the objective function that consists of multiple terms, and ω is the weight factor for each term. Four weight factors are respectively as 100, 1, 0.1, and 0.1 in this work.

When the value of the first term in $f(\boldsymbol{\rho})$ is close to zero (its minimum value), the necessary and sufficient condition of elastic isotropy would be satisfied. The aim of the second term is to make the effective isotropic Poisson's ratio negative and its absolute value as larger as possible. However, if we directly use ν in Equation (3.3) as the second term to be minimized, the optimization will tend to obtain non-isotropic designs with a very large NPR along principal directions. Based on the classical elasticity theory, the theoretical lower limit of an isotropic Poisson's ratio is -1. Therefore, we use $(\nu + 1)^2$ as the second term of f. Since the minimum value of ν is -1, the optimization will no longer favor non-isotropic designs with $\nu \ll -1$, and then this will reduce the conflict between elastic isotropy and NPR. The third term of f is to make the effective isotropic CTE negative and its absolute value as larger as possible. Since every potential design described by the proposed ground structure must have isotropic CTE, we can directly use α_{11} in Equation (4.1) as the third term to be minimized, which is different from the NPR term. α_{ref} is a reference CTE value as the normalization factor, which is defined as 10 ppm/°C in this work. Finally, we incorporate two geometric constraints into the objective function and served as a penalty term to ensure the design is practical. It should be noted again that it is because nonlinear equality constraints cannot be explicitly imposed by the genetic algorithm for optimization problems with integer variables. When the fourth term becomes zero (its minimum value), the design will not have intersecting bars or isolated parts.

Since the design variables consist of both integer and continuous variables, the discrete topology optimization in Equation (5.2) is a mixed integer programming problem and can be solved using the genetic algorithm. Here we use the built-in function *ga* in MATLAB [157] as a black-box optimization solver.

Once the optimal solutions are found, we will obtain microstructures that simultaneously exhibit elastic isotropy, NTE, and NPR. These optimized designs will consist of cylindrical struts and have no intersecting bars or isolated geometric parts. Therefore, they will possess tunability of effective material properties by altering the cross-sectional dimensions of struts. In this work, we aim to find the combination of the smallest possible algebraic values of CTE and Poisson’s ratio simultaneously, while ensuring the microstructures remain elastically isotropic. This is a constrained multi-objective optimization problem, which can be solved by the built-in function *gamultiobj* in MATLAB. As formulated in Equation (5.3), in this optimization, the design variables only include the cross-sectional dimensions of struts, two objective functions are the minimizations of Poisson's ratio and CTE value respectively, and the equality constrain function is defined to satisfy the elastic isotropy condition. It is worthy of note that nonlinear equality constraints can now be explicitly imposed by the genetic algorithm, because this constrained multi-objective optimization problem only has continuous variables. Pareto fronts can be obtained by solving this multi-objective optimization problem, which represent a series of isotropic microstructures with different combinations of NPR and NTE values.

If the microstructures are not required to remain elastically isotropic, the tunable ranges of their principal-directional Poisson's ratios and isotropic CTE values can be obtained by solving the single-objective optimization problem in Equation (5.4). Four objective functions in Equation (5.4) respectively correspond to finding the minimal and maximal values of Poisson's ratio and CTE. The genetic algorithm is also adopted as the solver.

$$\begin{aligned} &\text{Find: } \boldsymbol{\rho} = [\rho_1 \quad \cdots \quad \rho_{n_{b1}+n_{b2}}] \\ &\text{Min: } \begin{cases} F_1(\boldsymbol{\rho}) = \dfrac{{C_{12}}^H(\boldsymbol{\rho})}{{C_{11}}^H(\boldsymbol{\rho}) + {C_{12}}^H(\boldsymbol{\rho})} \\ F_2(\boldsymbol{\rho}) = {\alpha_{11}}^H(\boldsymbol{\rho}) \end{cases} \\ &\text{S.t.} \quad g(\boldsymbol{\rho}) = \dfrac{\left({C_{11}}^H(\boldsymbol{\rho}) - {C_{12}}^H(\boldsymbol{\rho})\right)}{2{C_{44}}^H(\boldsymbol{\rho})} - 1 = 0 \end{aligned} \tag{5.3}$$

Find: $\boldsymbol{\rho} = [\rho_1 \quad \cdots \quad \rho_{n_{b1}+n_{b2}}]$

$$\text{Min: } h(\boldsymbol{\rho}) = \begin{cases} \dfrac{{C_{12}}^H(\boldsymbol{\rho})}{{C_{11}}^H(\boldsymbol{\rho}) + {C_{12}}^H(\boldsymbol{\rho})} & \text{or} \\ -\dfrac{{C_{12}}^H(\boldsymbol{\rho})}{{C_{11}}^H(\boldsymbol{\rho}) + {C_{12}}^H(\boldsymbol{\rho})} & \text{or} \\ {\alpha_{11}}^H(\boldsymbol{\rho}) & \text{or} \\ -{\alpha_{11}}^H(\boldsymbol{\rho}) \end{cases} \tag{5.4}$$

5.3. Numerical results

By utilizing the proposed rational design method, it is possible to create 3D strut-based lattice metamaterials that exhibit an unprecedented combination of mechanical and thermal properties, including elastic isotropy, tunable thermal expansion, and tunable auxeticity, which cannot be achieved using conventional materials. However, before utilizing the proposed rational design method, it is crucial to identify a suitable combination of two constituent materials with different CTE values, yet mechanically and chemically compatible [226].

According to Takezawa and Kobashi [241], controlling the effective CTE of lattice metamaterials fabricated using polymers is challenging due to the strong temperature-dependent physical properties of polymers. This issue can be mitigated by using metals or alloys as constituent materials, as their physical properties exhibit less dependence on temperature. In this work, we investigate three different combinations of metals and alloys: Nickel and Invar (N-I), which has been previously utilized for lattices in [239]; Al 6061 and Ti6Al4V (A-T), which has been previously utilized for lattices in

[229, 244]; and CuCrZr and M300 (C-M), which is supported by a multi-metal additive manufacturing technique developed by [206]. Table 5.1 presents their material properties.

The ratios between the two CTE values for the three combinations are 9.125, 2.698, and 1.683, respectively, while the ratios between the two values of Young’s modulus are 1.333, 1.652, and 1.484. It can be observed that the N-I combination exhibits a high ratio of CTE values and the lowest ratio of Young's moduli, while the A-T combination displays a low ratio of CTE values and the highest ratio of Young's moduli. The C-M combination, on the other hand, has a very low ratio of CTE values. Notably, in the A-T or C-M combination, the constituent material with the higher CTE value has a lower Young's modulus than the other constituent material, which contrasts with the N-I combination. Additionally, the two Poisson’s ratios are identical for the N-I or C-M combination, and slightly different for the A-T combination.

Table 5.1. Properties listed for constituent materials

	Nickel	Invar	Al 6061	Ti6Al4V	CuCrZr	M300
Young’s modulus (GPa)	200	150	68.9	113.8	128	190
Poisson’s ratio	0.31	0.31	0.33	0.342	0.3	0.3
CTE (ppm/°C)	13.14	1.44	23.2	8.6	17	10.1

This section presents several novel optimized microstructures through a description of their geometries, an analysis of their effective material properties, and a demonstration of their macroscopic deformation behaviors. These 3D strut-based microstructures exhibit elastic isotropy, tunable auxeticity, and tunable thermal expansion for multiple combinations of constituent materials.

5.3.1. Novel microstructures

Figure 5.3 displays five novel microstructures discovered through the proposed design method, which are single-scale, bi-material, and strut-based. Their views from different angles are given in Figure 5.4. Unlike microstructures with bi-layer ribs previously reported in [217-222], each strut in these microstructures is a single-material cylinder with a constant cross-section, but different struts may be composed of distinct constituent materials and have varying cross-sectional radii. Furthermore, all microstructures are re-entrant and exhibit geometric cubic symmetry. The related geometry properties of these microstructures are summarized in Table 5.2. The microstructures I and II have simple geometries, and the microstructure V has the most complicated geometry.

Table 5.2. Geometry properties of microstructures

Microstructure	I	II	III	IV	V
Number of total vertices	54	45	78	51	75
Number of types of cross-sectional radii	3	4	6	6	7
n_{b1}	2	2	3	4	5
n_{b2}	1	2	3	2	2
Number of total struts	120	102	156	134	200
Number of struts composed of the second type of constituent material	48	48	96	54	72

5.3.2. Tunable effective material properties

Here, we numerically investigate the effective material properties of these microstructures. By changing their cross-sectional radii, we expect to obtain a range of different thermal and elastic properties. We define the range of variable radii as from 4e-3 to 1e-2 in this chapter when the length of the unit cell edge is set to one.

First, as shown in Figure 5.5, we study the tunable ranges of CTE and Poisson’s ratio without the constraint of elastic isotropy. This means that while tuning the material properties, we do not require the microstructures to remain elastically isotropic. Therefore, the Poisson's ratios given in Figure 5.5b are only values in the principal directions. However, due to the geometric cubic symmetry of the microstructures, their CTE is always isotropic.

From Figure 5.5a, we can see that except for microstructure II with the C-M material combination, all microstructures with the N-I, A-T, or C-M material combination exhibit a tunable range of NTE. For the N-I or A-T material combination, microstructure I exhibits a broad range of CTE from moderate PTE values to moderate NTE values, and microstructures III and IV can achieve large NTE values. Even for the C-M material combination with a low ratio of constituent CTE values, microstructures I, IV, and V can still exhibit a range of CTE from small PTE values to small NTE values. We also consider the tunable ranges of CTE when the two constituent materials are reversed within each microstructure. From Figure 5.5a, we can see that all microstructures with the reversed material combinations cannot be tuned to possess ZTE or NTE values, but they exhibit a tunable range of PTE with values much larger than those of the six constituent materials. For microstructure I, the obtainable values of CTE have partially overlapping ranges between the original and reversed material combinations.

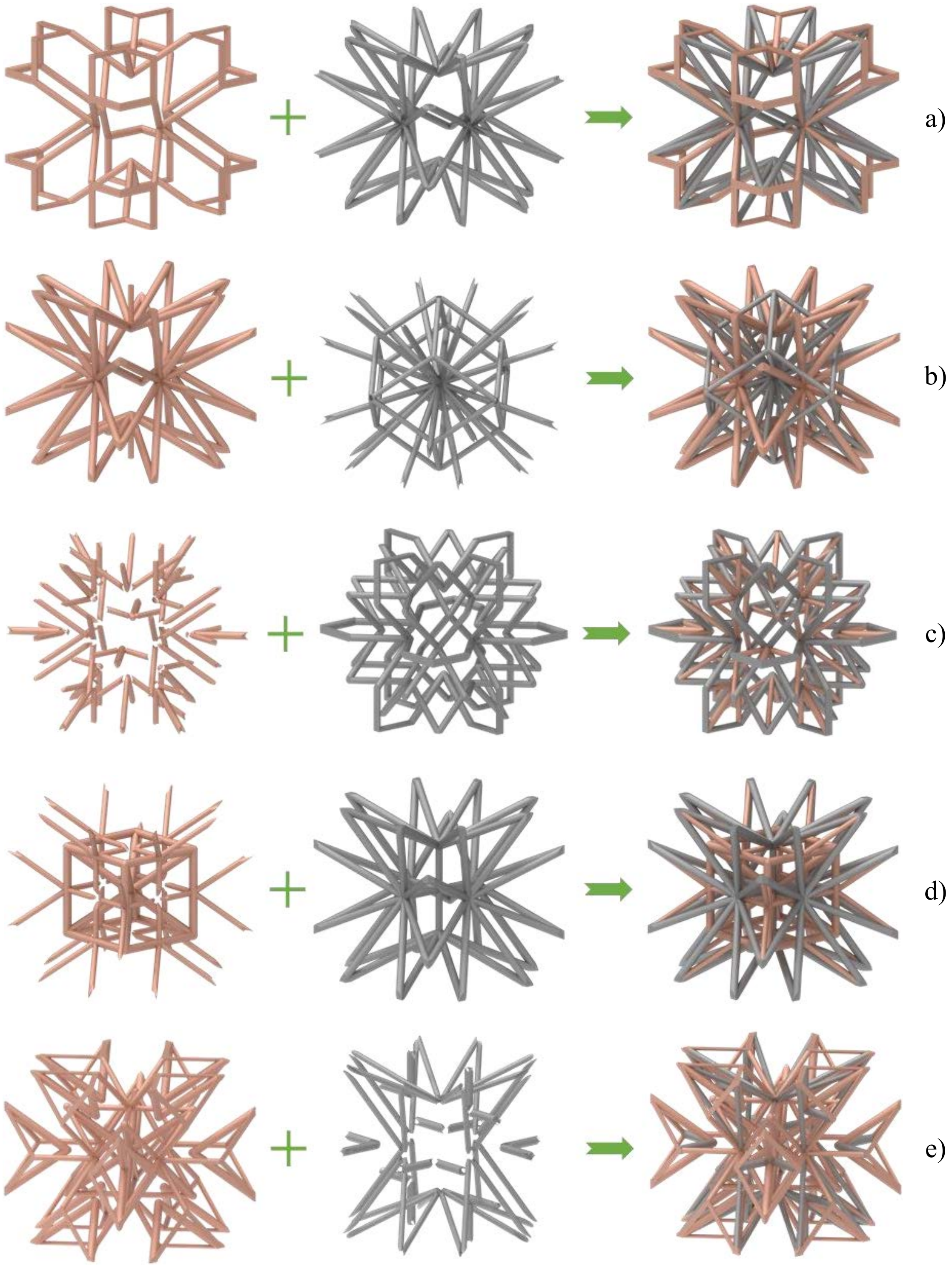

Figure 5.3. Novel strut-based bi-material microstructures and their two constituent parts (Note: rendered effect): a) Microstructure I; b) Microstructure II; c) Microstructure III; d) Microstructure IV; e) Microstructure V

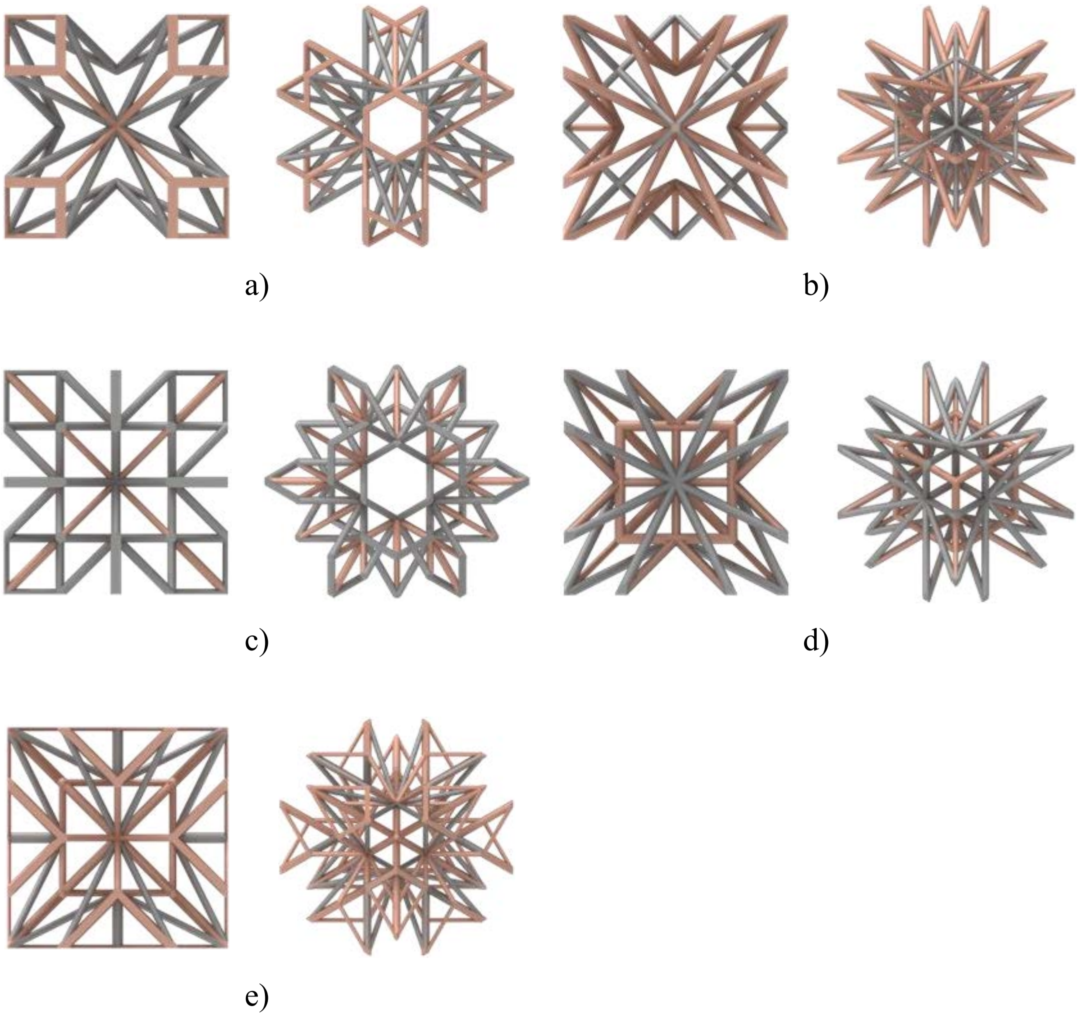

Figure 5.4. Novel strut-based bi-material microstructures viewed from other two angles (Note: rendered effect): a) Microstructure I; b) Microstructure II; c) Microstructure III; d) Microstructure IV; e) Microstructure V

From Figure 5.5b, we can see that for whether the original or the inverted material combinations, all microstructures can exhibit a very broad range of NPR in the principal directions. The microstructure I can even achieve large NPR values that are close to -0.9. For the microstructure II with the A-T and C-M material combination and the microstructure IV with the N-I, T-A, and M-C material combination, zero and small positive values of Poisson’s ratio are obtainable.

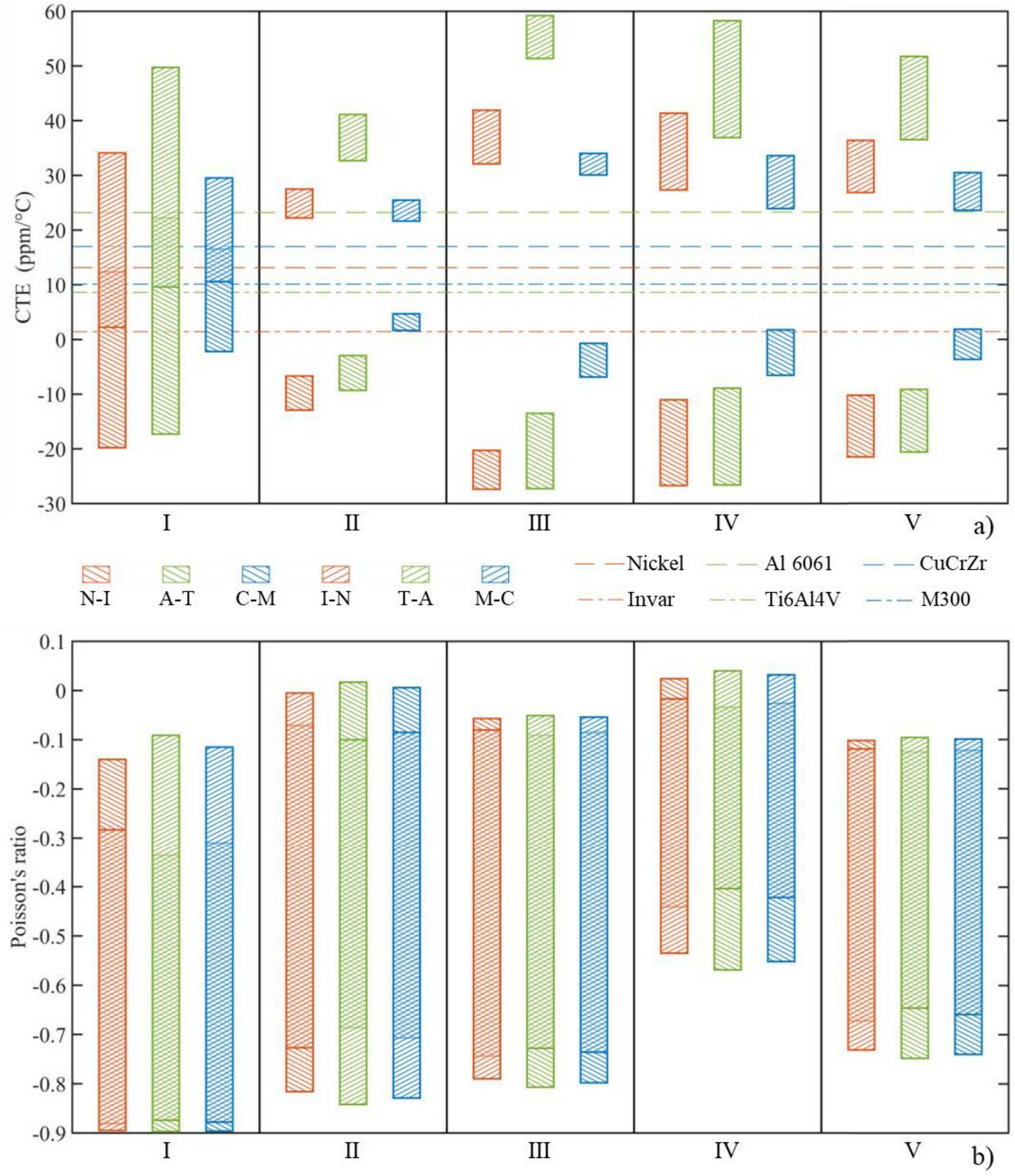

Figure 5.5. Tunable ranges of properties without elastic isotropy for six combinations of constituent materials: a) Isotropic CTE; b) Principal directional Poisson's ratio

Next, we will investigate the achievable values of the minimum CTE and the minimum Poisson's ratio while imposing the constraint of elastic isotropy. The Pareto fronts for five microstructures with three material combinations are respectively given in Figure5.6. For all the Pareto fronts, we can see that the smaller is the algebraic value of

Poisson’s ratio, the larger is the algebraic value of CTE. Besides, when the absolute values of NPR increase, the absolute values of NTE decrease faster.

For the N-I material with a high ratio of constituent CTE values, microstructure I can still exhibit NTE when it has a very large NPR (around -0.854). It has a moderate NPR (around -0.440) when it achieves NTE (around -18.51 ppm/°C) with the absolute values larger than its two constituent CTE values. For the N-I material combination, both microstructures III and IV can exhibit very large NTE with absolute values larger than the CTE values of all materials listed in Table 5.1. Compared with microstructure IV, microstructure III not only has a slightly larger NTE but also has a range of larger NPR values.

For the A-T material with a low ratio of constituent CTE values, all microstructures still exhibit NTE and NPR simultaneously, while they are also elastically isotropic. Microstructure I can exhibit NTE when it has a relatively large NPR (around -0.738), but the absolute value of its largest NTE (around -12.46 ppm/°C) is much smaller than the CTE value of Al 6061. Only microstructures III and IV can exhibit NTE with absolute values larger than 23.2 ppm/°C.

Even for the C-M material with a very low ratio of CTE values, microstructures III-V exhibit a range of NTE and NPR simultaneously, while they keep elastic isotropy. Microstructure I also exhibit small NTE when its Poisson’s ratio is larger than -0.511. Although microstructure II with the C-M material combination cannot exhibit NTE, its

PTE values are smaller than its two constituent CTE values.

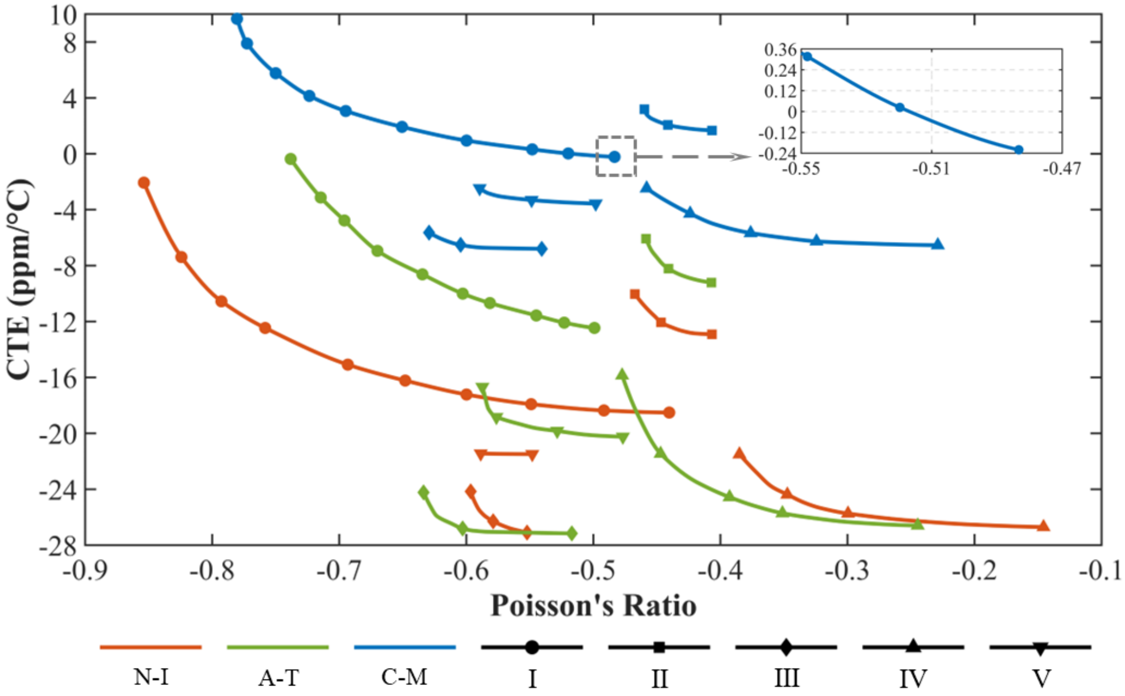

Figure 5.6. Pareto fronts of CTE and Poisson's ratio with the elastic isotropy constraint

Moreover, we select every microstructure represented by the data point with the smallest algebraic value of CTE, i.e., the right end point, of each Pareto front in Figure 5.6 for further analyses. It can be found that the surfaces of Young's modulus (See Figure 5.7) for these microstructures all exhibit a shape that is like a sphere, indicating that these microstructures have elastic isotropy, which is consistent with the constraint used in the optimization process to obtain the Pareto fronts. The relative errors between the maximal and minimal Young's moduli being below 0.05% further reinforces this observation. These results suggest that the microstructures designed in this study not only exhibit tunable thermal and elastic properties but also satisfy the requirement of elastic isotropy.

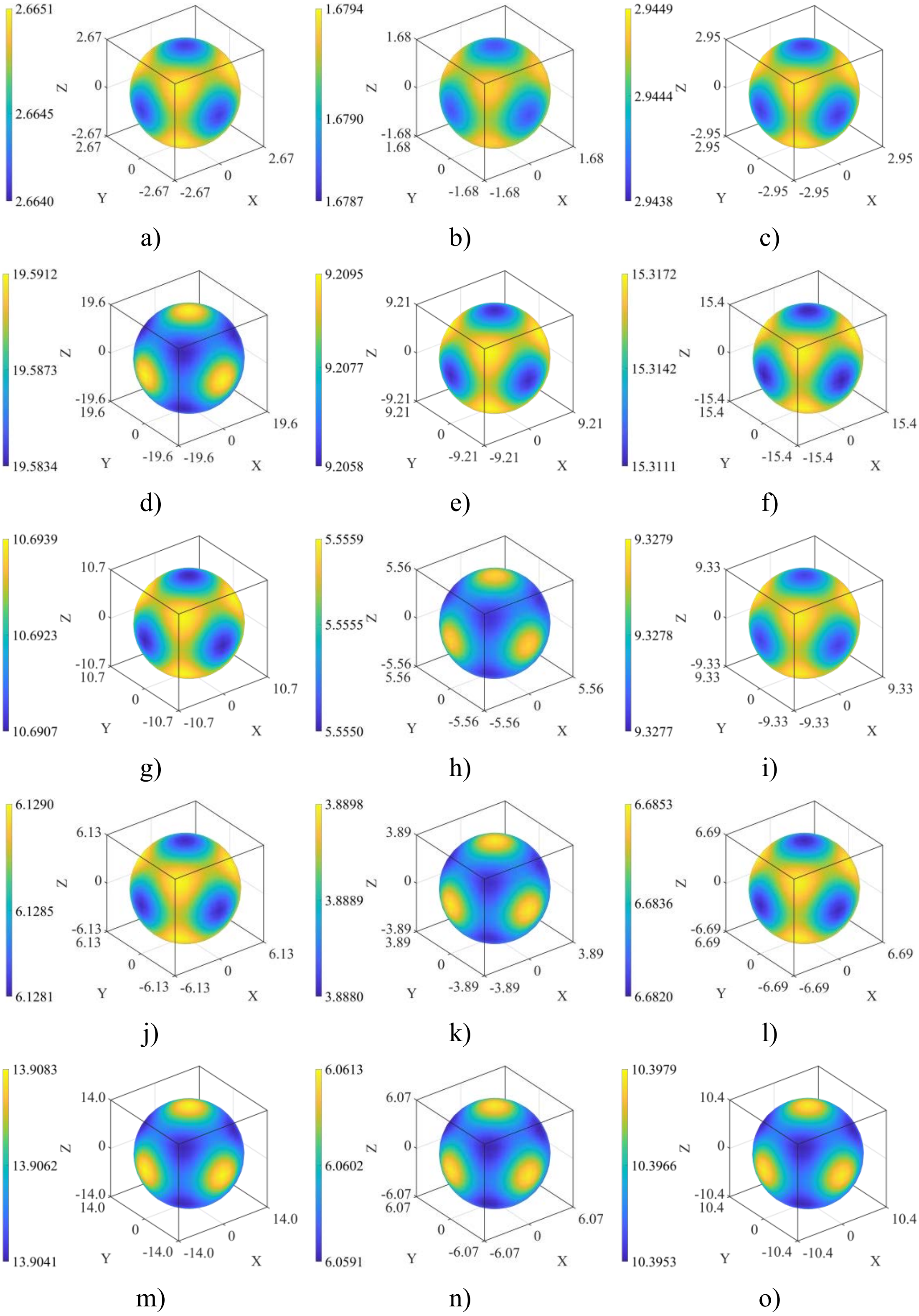

Figure 5.7. Surfaces of Young's modulus (Unit: MPa): a-c) Microstructure I; d-f) Microstructure II; g-i) Microstructure III; j-l) Microstructure IV; m-o) Microstructure V. Three columns respectively correspond to the N-I, A-T, and C-M material combinations.

It should be noted that visualization of evolution histories is not available here for multi-objective optimization results, since it would be a dynamic evolution of a curve. However, the proposed design method's maturity can be undeniably confirmed by the five optimized microstructures with totally novel topologies and multifunctionalities that have not been achieved before in literatures.

5.3.3. Analyses of lattice structures

By periodically assembling a cellular microstructure along three principal directions, a macroscopic 3D lattice structure can be generated. The novel microstructures in Figure 5.3 can be used to create lightweight strut-based lattice structures. These composite lattice structures can be made of metallic material combinations listed in Table 5.1 or any other two compatible materials with dissimilar properties.

To analyze the macroscopic deformation behaviors of the designed microstructures, we used the finite element method to numerically simulate macroscopic lattice structures. We assembled these structures using periodic arrays of microstructures and conducted the simulations in the commercial software COMSOL using beam elements. The geometric symmetry of the lattice structures is utilized to decrease the cost in the finite element simulation. For example, in a 2D structure with orthogonal symmetry undergoing free thermal expansion with a unit rise in temperature, only a quarter of the structure needs to be used in the analysis, as illustrated in Figure 5.8a. The same applies to simulating uniaxial compression, as shown in Figure 5.8b.

In a 3D lattice structure with orthogonal symmetry, only one-eighth of the structure needs to be used in the analysis, as represented by the purple region in Figure 5.8c. The right surface of the analyzed substructure is defined in the figure. If the structure undergoing free thermal expansion is made of a homogeneous material, the ratio of the translational displacement in the X-direction to the length of the structure would be equal to the CTE of the material at every point on the right surface. Similarly, if a structure undergoing a uniaxial compressive load in the Z-direction is made of a homogeneous material, the negative ratio of the translational displacement in the X-direction to the forced displacement in the Z-direction will be equal to the Poisson's ratio of the material at every point on the right surface.

The use of lattice structures composed of cellular and composite microstructures offers advantages over homogeneous materials, including greater strength and stiffness, improved energy absorption, and enhanced thermal and acoustic insulation. However, the ratios of points on the surface of these structures may fluctuate, which will affect their effective material properties. To ensure that the microstructures in the lattice structure meet the periodic boundary condition and maintain consistent effective properties, a certain number of microstructures will be required to infill the structure. This is important to minimize fluctuations in the ratios of points on the surface. The number of microstructures required to infill the lattice structure may depend on a variety of factors, including the size and geometry of the microstructures and the overall size and shape of the lattice structure. With a careful configuration, it is possible to minimize the number of microstructures required to meet the periodic boundary condition. This can help reduce costs and increase efficiency in manufacturing, while still providing the necessary performance characteristics.

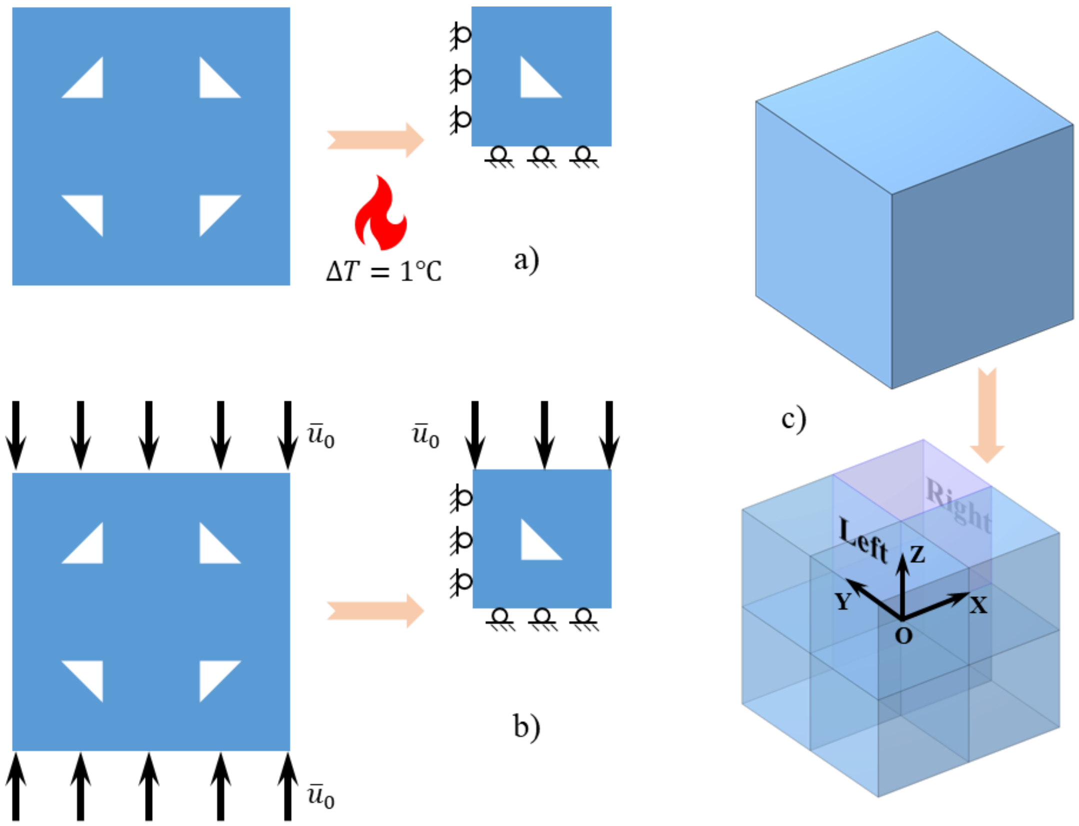

Figure 5.8. Reduced models with symmetric boundary conditions for analyses

The focus of this study is on lattice structures assembled using specific microstructures represented by the right end points of Pareto fronts in Figure 5.6. As shown in Figure 5.9, each lattice structure is assembled from 24×24×24 microstructures. Due to geometric symmetry, one-eighth of this structure (12×12×12 microstructures) is used in the finite element analysis. For the numerical results in Figure 5.9, black lines represent the undeformed structures, and colorful lines describe the deformed structures in a proper scale, where the values are displacement magnitudes. The results show that the lattice structures contract in three principal directions when subjected to a temperature increase and exhibit transverse contraction under forced vertical compression. For the sake of briefness, the numerical simulations consider the N-I material combination.

Figure 5.10 presents the displacement ratios on the right surfaces of these lattice structures. For the load case simulating free thermal expansion, lattice structures I, IV, and V exhibit very small fluctuations between their displacement ratios and effective CTE values, with relative errors all below 1%. This indicates a high level of consistency in their design. Lattice structures II and III have slightly larger relative errors. However, only small regions on the top right corners of lattice III have relative errors over 1%, and the largest relative error of lattice II is 1.74%, which is still acceptable. This suggests that the design of these lattice structures is generally consistent but may have some minor variations.

Figure 5.10 also presents numerical results for the uniaxial compression load case using the same lattice structures. It can be found that lattice IV has the smallest fluctuation between the displacement ratios and effective Poisson’s ratio, with relative errors around 4%~5%. Except for the regions on the right edges, lattice III has the second-smallest fluctuation. For all these lattices, the analysis indicates that most of the relative errors are larger than those of CTE, and the regions with large relative errors appear on different positions. However, a comparison of the numerical results for lattice structures assembled by a smaller number of microstructures shows that the more microstructures used to assemble the lattice structure, the fewer fluctuations there are

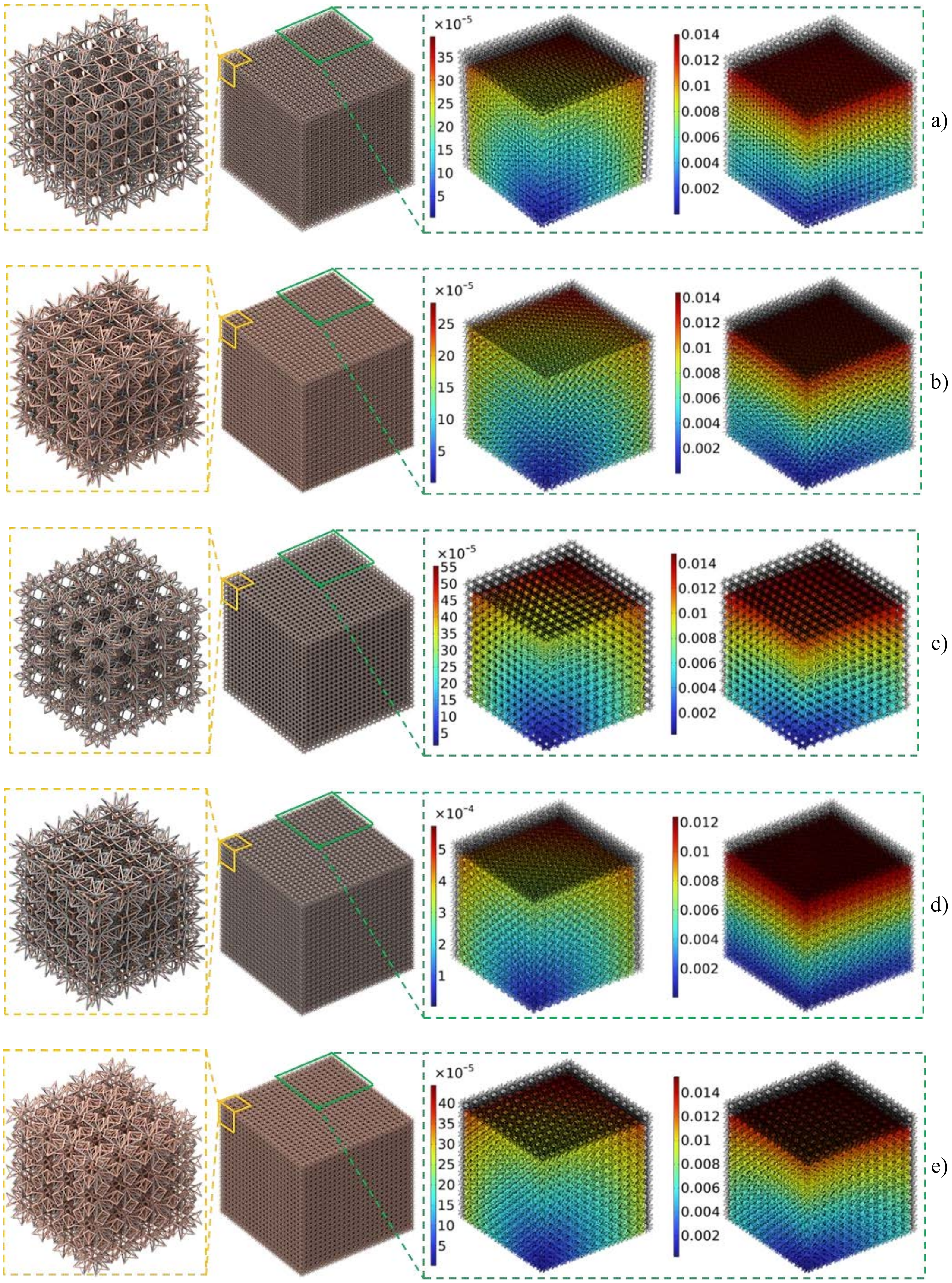

Figure 5.9. Macroscopic lattice structures and their deformations: a) Lattice I; b) Lattice II; ci) Lattice III; d) Lattice IV; e) Lattice V. Enlarged views of the lattice structures are given in orange dash rectangles (Note: rendered effect). Simulation results (Unit: mm) using the one-eighth structure are shown in green dashed rectangles for the load cases: free thermal expansion (left) and vertical compression (right).

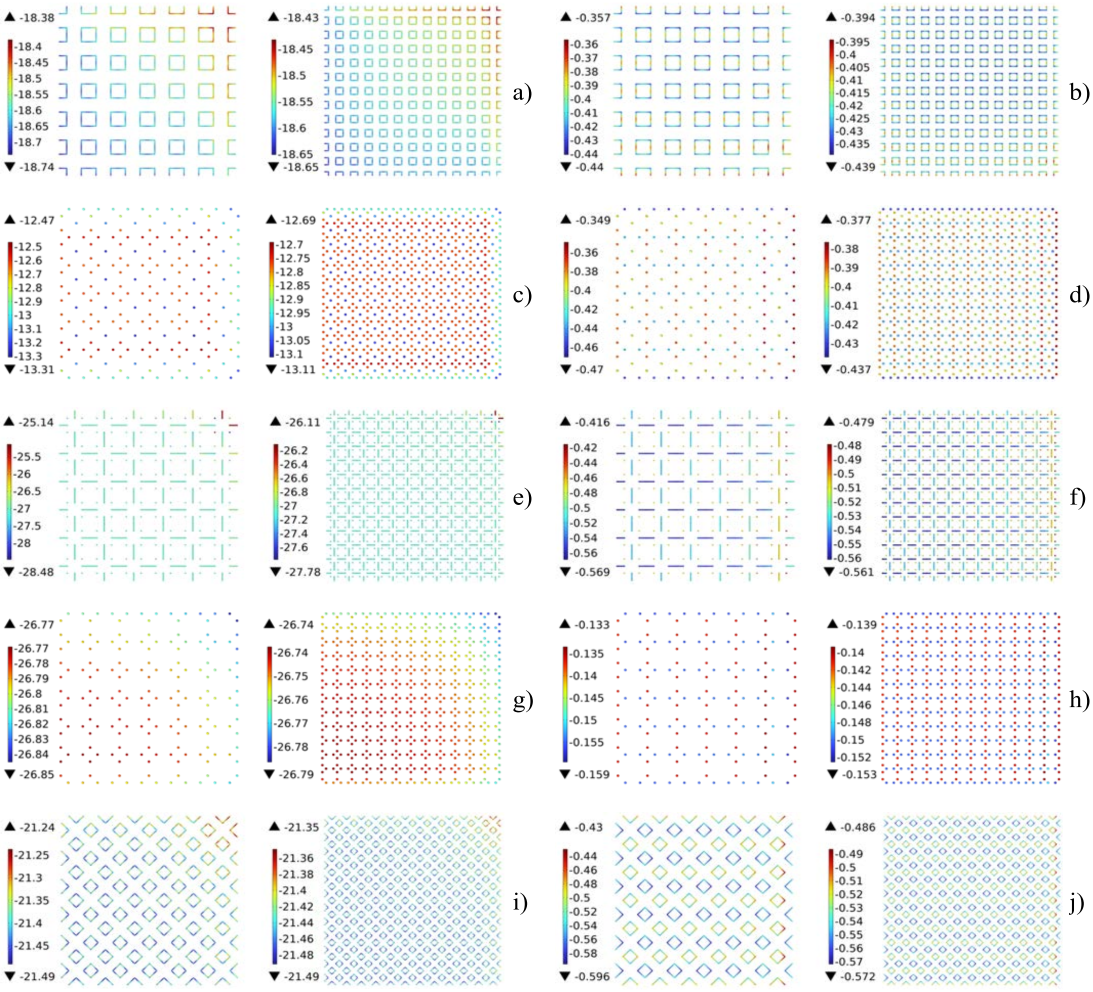

Figure 5.10. Displacement ratios of points on the right surface of the analyzed lattice structures: a-b) Lattice I; c-d) Lattice II; e-f) Lattice III; g-h) Lattice IV; i-j) Lattice V. a, c, e, g, i) displacement ratios in the load case simulating free thermal expansion; b, d, f, h, j) displacement ratios in the load case simulating uniaxial compression. In each subfigure, simulation results are given for two lattice structures that are respectively assembled by 6×6×6 microstructures (left) and 12×12×12 microstructures (right)

between the displacement ratios and effective Poisson's ratios. This also applies to the consistency of CTE. By analyzing the relative errors in their properties, this study provides insights into how to improve the consistency of these structures and identify the required microstructures for different design scenarios.

5.4. Conclusion

The work proposes a rational design method for discovering novel multifunctional lattice metamaterials with unusual mechanical properties. The proposed method involves a discrete topology optimization approach that uses a 3D muti-material ground structure with geometric cubic symmetry. To evaluate the potential designs generated by the ground structure, the study employs the computational homogenization method with beam elements to calculate effective elastic stiffness matrices and effective coefficients of thermal expansion. Based on these calculations, the research formulates a mathematical optimization formulation to identify metamaterials that simultaneously exhibit elastic isotropy, negative thermal expansion, and negative Poisson’s ratio. This is a mixed-integer programming problem that is solved using the genetic algorithm. This study can identify novel metamaterial designs that exhibit a combination of properties that have not been achieved before. Commercial finite element analysis software is used for the design of experiment to investigate the mechanical behaviors of lattice metamaterials with three different combinations of metals and alloys.

Chapter 6 Conclusions and Prospects

6.1 Conclusions

This research has developed a series of systematic and rational design methods based on topology optimization for finding four types of lattice metamaterials with unusual mechanical properties. A series of novel 3D microstructures have been found by the proposed design methods and studied in this research. These new design methods and novel microstructures are summarized as follows:

Chapter 2 focuses on pentamode metamaterials with at least elastic orthotropic symmetry. By deriving the necessary and sufficient condition required for their elasticity constants, a new mathematical optimization formulation is proposed for the design of such type of mechanical metamaterial. A discrete topology optimization method is developed by using a 3D ground structure with geometric orthogonal symmetry. This method is particularly computationally efficient to find many different optimized microstructures that consist of slender struts. Twenty-four novel 3D pentamode microstructures are found and studied in this chapter, including isotropic, transverse isotropic, and orthotropic ones. This library of microstructures can provide more metamaterial options for pentamode cloaking.

Chapter 3 focuses on 3D lattice metamaterials with ideal elastic isotropy and Poisson's ratios at the theoretical lower limit -1, which are a special type of unimode metamaterials. A discrete topology optimization method is developed by using a 3D ground structure with geometric cubic symmetry. Both integer and continuous variables are adopted for topological descriptions based on the ground structure. This method has a small number of design variables and a good ability of structural description. It is computationally efficient to design ultra-light microstructures that consist of struts with various cross-sectional dimensions. In the mathematical optimization formulation, constraints on intersecting bars and isolated geometric parts are proposed, which provide an essential contribution for obtaining practical designs in discrete topology optimization of mechanical metamaterials. As numerical examples, four novel isotropic unimode microstructures are found and studied in this chapter. These 3D microstructures with isotropic Poisson's ratios at the theoretical lower limit are single-scale, single-phase, and constructed by elastic continua, filling an important blank of the engineered material library.

Chapter 4 focuses on 3D isotropic auxetic metamaterials with thermal dimensional stability. A multi-material continuum topology optimization method customized for designing 3D isotropic microstructures is developed. By imposing the geometric cubic symmetry constraint on the design domain with element density clustering, this method can guarantee that every intermediate design has at least elastic cubic symmetry and then easily obtain elastically isotropic optimized designs. A novel 3D composite microstructure is found and studied in this chapter, which simultaneously exhibits elastic isotropy, negative Poisson's ratio, and zero thermal expansion.

Chapter 5 focuses on multifunctional isotropic metamaterials with tunabilities of thermal expansion and auxeticity. A multi-material discrete topology optimization method is developed by using a 3D bi-material ground structure with geometric cubic symmetry. Both integer and continuous variables are adopted to describe bi-material microstructures that consist of beams with a few types of cross-sections. This method can easily generate bi-material microstructures with relatively simpler geometries when compared with continuum topology optimization methods. Furthermore, this method can provide parametric designs that exhibit tunabilities of effective material properties. Five novel 3D strut-based composite microstructures are found and studied in this chapter. By tailoring either the cross-sectional dimensions or the constituent material combination of struts, these microstructures can simultaneously exhibit a range of negative Poisson's ratios and negative coefficients of thermal expansion while keeping elastically isotropic.

6.2 Prospects

Based on the research results of this thesis, prospective future works are outlined as follows:

1) A systematic design method can be developed for finding fully anisotropic pentamode metamaterials. Applications of these pentamode metamaterials in elastic cloaks and acoustic cloaks can be studied.

2) Systematic design methods should be developed for finding lattice metamaterials

with other combinations of unusual properties, e.g., pentamode and ZTE/NTE, ultra-conductive and ZTE/NTE.

3) Using the state-of-the-art multi-metallic additive manufacturing technique, bi-metallic metamaterials with unusual thermal expansion can be fabricated and experimentally studied.

4) Robust topology optimization methods can be developed to consider both geometric and material uncertainties induced by multi-metallic additive manufacturing.

References

[1] V.G. Veselago, The electrodynamics of substances with simultaneously negative values of ϵ and μ, Sov. Phys. Uspekhi. 10 (1968) 509. https://doi.org/10.1070/PU1968v010n04ABEH003699.

[2] J.B. Pendry, A.J. Holden, W.J. Stewart, I. Youngs, Extremely Low Frequency Plasmons in Metallic Mesostructures, Phys. Rev. Lett. 76 (1996) 4773–4776. https://doi.org/10.1103/PhysRevLett.76.4773.

[3] J.B. Pendry, A.J. Holden, D.J. Robbins, W.J. Stewart, Magnetism from conductors and enhanced nonlinear phenomena, IEEE Trans. Microw. Theory Tech. 47 (1999) 2075–2084. https://doi.org/10.1109/22.798002.

[4] S. John, Strong localization of photons in certain disordered dielectric superlattices, Phys. Rev. Lett. 58 (1987) 2486–2489. https://doi.org/10.1103/PhysRevLett.58.2486.

[5] E. Yablonovitch, Inhibited Spontaneous Emission in Solid-State Physics and Electronics, Phys. Rev. Lett. 58 (1987) 2059–2062. https://doi.org/10.1103/PhysRevLett.58.2059.

[6] Z. Liu, X. Zhang, Y. Mao, Y.Y. Zhu, Z. Yang, C.T. Chan, P. Sheng, Locally Resonant Sonic Materials, Science (80-.). 289 (2000) 1734–1736. https://doi.org/10.1126/science.289.5485.1734.

[7] M.-H. Lu, L. Feng, Y.-F. Chen, Phononic crystals and acoustic metamaterials, Mater. Today. 12 (2009) 34–42. https://doi.org/10.1016/S1369-7021(09)70315-3.

[8] C.Z. Fan, Y. Gao, J.P. Huang, Shaped graded materials with an apparent negative thermal conductivity, Appl. Phys. Lett. 92 (2008) 251907. https://doi.org/10.1063/1.2951600.

[9] T. Chen, C.-N. Weng, J.-S. Chen, Cloak for curvilinearly anisotropic media in conduction, Appl. Phys. Lett. 93 (2008) 114103. https://doi.org/10.1063/1.2988181.

[10] R. Schittny, M. Kadic, S. Guenneau, M. Wegener, Experiments on Transformation Thermodynamics: Molding the Flow of Heat, Phys. Rev. Lett. 110 (2013) 195901. https://doi.org/10.1103/PhysRevLett.110.195901.

[11] R. Hu, S. Zhou, Y. Li, D.-Y. Lei, X. Luo, C.-W. Qiu, Illusion Thermotics, Adv. Mater. 30 (2018) 1707237. https://doi.org/10.1002/adma.201707237.

[12] V.S. Deshpande, N.A. Fleck, M.F. Ashby, Effective properties of the octet-truss lattice material, J. Mech. Phys. Solids. 49 (2001) 1747–1769. https://doi.org/10.1016/S0022-5096(01)00010-2.

[13] X. Zheng, H. Lee, T.H. Weisgraber, M. Shusteff, J. DeOtte, E.B. Duoss, J.D. Kuntz, M.M. Biener, Q. Ge, J.A. Jackson, S.O. Kucheyev, N.X. Fang, C.M. Spadaccini,

Ultralight, ultrastiff mechanical metamaterials, Science (80-.). 344 (2014) 1373–1377. https://doi.org/10.1126/science.1252291.

[14] J.B. Berger, H.N.G. Wadley, R.M. McMeeking, Mechanical metamaterials at the theoretical limit of isotropic elastic stiffness, Nature. 543 (2017) 533–537. https://doi.org/10.1038/nature21075.

[15] https://srrcalculator.blogspot.com/p/calculator.html

[16] M. Kadic, G.W. Milton, M. van Hecke, M. Wegener, 3D metamaterials, Nat. Rev. Phys. 1 (2019) 198–210. https://doi.org/10.1038/s42254-018-0018-y.

[17] M.P. Bendsøe, Optimal shape design as a material distribution problem, Struct. Optim. 1 (1989) 193–202. https://doi.org/10.1007/BF01650949.

[18] O. Sigmund, A 99 line topology optimization code written in Matlab, Struct. Multidiscip. Optim. 21 (2001) 120–127. https://doi.org/10.1007/s001580050176.

[19] F. Wang, B.S. Lazarov, O. Sigmund, On projection methods, convergence and robust formulations in topology optimization, Struct. Multidiscip. Optim. 43 (2011) 767–784. https://doi.org/10.1007/s00158-010-0602-y.

[20] Y.M. Xie, G.P. Steven, A simple evolutionary procedure for structural optimization, Comput. Struct. 49 (1993) 885–896. https://doi.org/10.1016/0045-7949(93)90035-C.

[21] Q. Li, G.P. Steven, O.M. Querin, Y.M. Xie, Shape and topology design for heat conduction by Evolutionary Structural Optimization, Int. J. Heat Mass Transf. 42 (1999) 3361–3371. https://doi.org/10.1016/S0017-9310(99)00008-3.

[22] X. Huang, Y.M. Xie, Bi-directional evolutionary topology optimization of continuum structures with one or multiple materials, Comput. Mech. 43 (2009) 393–401. https://doi.org/10.1007/s00466-008-0312-0.

[23] M.Y. Wang, X. Wang, D. Guo, A level set method for structural topology optimization, Comput. Methods Appl. Mech. Eng. 192 (2003) 227–246. https://doi.org/10.1016/S0045-7825(02)00559-5.

[24] G. Allaire, F. Jouve, A.-M. Toader, Structural optimization using sensitivity analysis and a level-set method, J. Comput. Phys. 194 (2004) 363–393. https://doi.org/10.1016/j.jcp.2003.09.032.

[25] Z. Luo, M.Y. Wang, S. Wang, P. Wei, A level set-based parameterization method for structural shape and topology optimization, Int. J. Numer. Methods Eng. (2008). https://doi.org/10.1002/nme.2092.

[26] X. Guo, W. Zhang, W. Zhong, Doing topology optimization explicitly and geometrically-a new moving morphable components based framework, J. Appl. Mech. Trans. ASME. 81 (2014). https://doi.org/10.1115/1.4027609.

[27] J.A. Norato, B.K. Bell, D.A. Tortorelli, A geometry projection method for

continuum-based topology optimization with discrete elements, Comput. Methods Appl. Mech. Eng. 293 (2015) 306–327. https://doi.org/10.1016/j.cma.2015.05.005.

[28] Y. Zhou, W. Zhang, J. Zhu, Z. Xu, Feature-driven topology optimization method with signed distance function, Comput. Methods Appl. Mech. Eng. 310 (2016) 1–32. https://doi.org/10.1016/j.cma.2016.06.027.

[29] W.S. Dorn, R.E. Gomory, H.J. Greenberg, Automatic design of optimal structures, J Mec. 3 (1964) 25-52.

[30] T. Zegard, G.H. Paulino, GRAND — Ground structure based topology optimization for arbitrary 2D domains using MATLAB, Struct. Multidiscip. Optim. 50 (2014) 861–882. https://doi.org/10.1007/s00158-014-1085-z.

[31] N. Aage, E. Andreassen, B.S. Lazarov, O. Sigmund, Giga-voxel computational morphogenesis for structural design, Nature. 550 (2017) 84–86. https://doi.org/10.1038/nature23911.

[32] M. Baandrup, O. Sigmund, H. Polk, N. Aage, Closing the gap towards super-long suspension bridges using computational morphogenesis, Nat. Commun. 11 (2020) 2735. https://doi.org/10.1038/s41467-020-16599-6.

[33] M.P. Bendsøe, N. Kikuchi, Generating optimal topologies in structural design using a homogenization method, Comput. Methods Appl. Mech. Eng. 71 (1988) 197–224. https://doi.org/10.1016/0045-7825(88)90086-2.

[34] M. Stolpe, K. Svanberg, An alternative interpolation scheme for minimum compliance topology optimization, Struct. Multidiscip. Optim. 22 (2001) 116–124. https://doi.org/10.1007/s001580100129.

[35] O. Sigmund, On the Design of Compliant Mechanisms Using Topology Optimization, Mech. Struct. Mach. 25 (1997) 493–524. https://doi.org/10.1080/08905459708945415.

[36] B. Bourdin, Filters in topology optimization, Int. J. Numer. Methods Eng. 50 (2001) 2143–2158. https://doi.org/10.1002/nme.116.

[37] J.K. Guest, J.H. Prévost, T. Belytschko, Achieving minimum length scale in topology optimization using nodal design variables and projection functions, Int. J. Numer. Methods Eng. 61 (2004) 238–254. https://doi.org/10.1002/nme.1064.

[38] J.K. Guest, Imposing maximum length scale in topology optimization, Struct. Multidiscip. Optim. 37 (2009) 463–473. https://doi.org/10.1007/s00158-008-0250-7.

[39] O. Sigmund, Morphology-based black and white filters for topology optimization, Struct. Multidiscip. Optim. 33 (2007) 401–424. https://doi.org/10.1007/s00158-006-0087-x.

[40] Y. Yu, T. Hur, J. Jung, I.G. Jang, Deep learning for determining a near-optimal

topological design without any iteration, Struct. Multidiscip. Optim. 59 (2019) 787–799. https://doi.org/10.1007/s00158-018-2101-5.

[41] D.W. Abueidda, S. Koric, N.A. Sobh, Topology optimization of 2D structures with nonlinearities using deep learning, Comput. Struct. 237 (2020) 106283. https://doi.org/10.1016/j.compstruc.2020.106283.

[42] A. Chandrasekhar, K. Suresh, TOuNN: Topology Optimization using Neural Networks, Struct. Multidiscip. Optim. 63 (2021) 1135–1149. https://doi.org/10.1007/s00158-020-02748-4.

[43] H. Jeong, J. Bai, C.P. Batuwatta-Gamage, C. Rathnayaka, Y. Zhou, Y. Gu, A Physics-Informed Neural Network-based Topology Optimization (PINNTO) framework for structural optimization, Eng. Struct. 278 (2023) 115484. https://doi.org/10.1016/j.engstruct.2022.115484.

[44] O.M. Querin, G.P. Steven, Y.M. Xie, Evolutionary structural optimisation (ESO) using a bidirectional algorithm, Eng. Comput. 15 (1998) 1031–1048. https://doi.org/10.1108/02644409810244129.

[45] Q. Li, G.P. Steven, Y.M. Xie, A simple checkerboard suppression algorithm for evolutionary structural optimization, Struct. Multidiscip. Optim. 22 (2001) 230–239. https://doi.org/10.1007/s001580100140.

[46] Q. Li, G.P. Steven, O.M. Querin, Y.M. Xie, Structural topology design with multiple thermal criteria, Eng. Comput. 17 (2000) 715–734. https://doi.org/10.1108/02644400010340642.

[47] Q. Li, G.P. Steven, Y. M. Xie, Thermoelastic topology optimization for problems with varying temperature fields, J. Therm. Stress. 24 (2001) 347–366. https://doi.org/10.1080/01495730151078153.

[48] Q. Li, G.P. Steven, Y.M. Xie, O.M. Querin, Evolutionary topology optimization for temperature reduction of heat conducting fields, Int. J. Heat Mass Transf. 47 (2004) 5071–5083. https://doi.org/10.1016/j.ijheatmasstransfer.2004.06.010.

[49] M. Burger, B. Hackl, W. Ring, Incorporating topological derivatives into level set methods, J. Comput. Phys. 194 (2004) 344–362. https://doi.org/10.1016/j.jcp.2003.09.033.

[50] G. Allaire, F. de Gournay, F. Jouve, A.-M. Toader, Structural optimization using topological and shape sensitivity via a level set method, Control Cybern. 34 (2005) 59–80. http://eudml.org/doc/209353.

[51] S.Y. Wang, K.M. Lim, B.C. Khoo, M.Y. Wang, An extended level set method for shape and topology optimization, J. Comput. Phys. 221 (2007) 395–421. https://doi.org/10.1016/j.jcp.2006.06.029.

[52] A. Takezawa, S. Nishiwaki, M. Kitamura, Shape and topology optimization based on the phase field method and sensitivity analysis, J. Comput. Phys. 229 (2010)

2697–2718. https://doi.org/10.1016/j.jcp.2009.12.017.

[53] T. Yamada, K. Izui, S. Nishiwaki, A. Takezawa, A topology optimization method based on the level set method incorporating a fictitious interface energy, Comput. Methods Appl. Mech. Eng. 199 (2010) 2876–2891. https://doi.org/10.1016/j.cma.2010.05.013.

[54] F. Wein, P.D. Dunning, J.A. Norato, A review on feature-mapping methods for structural optimization, Struct. Multidiscip. Optim. 62 (2020) 1597–1638. https://doi.org/10.1007/s00158-020-02649-6.

[55] W. Zhang, J. Yuan, J. Zhang, X. Guo, A new topology optimization approach based on Moving Morphable Components (MMC) and the ersatz material model, Struct. Multidiscip. Optim. 53 (2016) 1243–1260. https://doi.org/10.1007/s00158-015-1372-3.

[56] W. Zhang, D. Li, J. Yuan, J. Song, X. Guo, A new three-dimensional topology optimization method based on moving morphable components (MMCs), Comput. Mech. 59 (2017) 647–665. https://doi.org/10.1007/s00466-016-1365-0.

[57] S. Zhang, J.A. Norato, A.L. Gain, N. Lyu, A geometry projection method for the topology optimization of plate structures, Struct. Multidiscip. Optim. 54 (2016) 1173–1190. https://doi.org/10.1007/s00158-016-1466-6.

[58] J.A. Norato, Topology optimization with supershapes, Struct. Multidiscip. Optim. 58 (2018) 415–434. https://doi.org/10.1007/s00158-018-2034-z.

[59] J. Gielis, A generic geometric transformation that unifies a wide range of natural and abstract shapes, Am. J. Bot. (2003). https://doi.org/10.3732/ajb.90.3.333.

[60] W. Zhang, Y. Zhou, J. Zhu, A comprehensive study of feature definitions with solids and voids for topology optimization, Comput. Methods Appl. Mech. Eng. 325 (2017) 289–313. https://doi.org/10.1016/j.cma.2017.07.004.

[61] Y. Zhou, J. Zhu, H. Zhan, W. Zhang, Y. Gu, A bio-inspired B-Spline Offset Feature for structural topology optimization, Comput. Methods Appl. Mech. Eng. 386 (2021) 114081. https://doi.org/10.1016/j.cma.2021.114081.

[62] T. Zegard, G.H. Paulino, GRAND3 — Ground structure based topology optimization for arbitrary 3D domains using MATLAB, Struct. Multidiscip. Optim. 52 (2015) 1161–1184. https://doi.org/10.1007/s00158-015-1284-2.

[63] O. Sigmund, Materials with prescribed constitutive parameters: An inverse homogenization problem, Int. J. Solids Struct. 31 (1994) 2313–2329. https://doi.org/10.1016/0020-7683(94)90154-6.

[64] O. Sigmund, Tailoring materials with prescribed elastic properties, Mech. Mater. 20 (1995) 351–368. https://doi.org/10.1016/0167-6636(94)00069-7.

[65] J.E. Cadman, S. Zhou, Y. Chen, Q. Li, On design of multi-functional

microstructural materials, J. Mater. Sci. 48 (2013) 51–66. https://doi.org/10.1007/s10853-012-6643-4.

[66] W. Li, F. Meng, Y. Chen, Y. fan Li, X. Huang, Topology Optimization of Photonic and Phononic Crystals and Metamaterials: A Review, Adv. Theory Simulations. 2 (2019) 1900017. https://doi.org/10.1002/adts.201900017.

[67] D.C. Dobson, S.J. Cox, Maximizing Band Gaps in Two-Dimensional Photonic Crystals, SIAM J. Appl. Math. 59 (1999) 2108–2120. https://doi.org/10.1137/S0036139998338455.

[68] C.Y. Kao, S. Osher, E. Yablonovitch, Maximizing band gaps in two-dimensional photonic crystals by using level set methods, Appl. Phys. B. 81 (2005) 235–244. https://doi.org/10.1007/s00340-005-1877-3.

[69] L. He, C.-Y. Kao, S. Osher, Incorporating topological derivatives into shape derivatives based level set methods, J. Comput. Phys. 225 (2007) 891–909. https://doi.org/10.1016/j.jcp.2007.01.003.

[70] F. Meng, X. Huang, B. Jia, Bi-directional evolutionary optimization for photonic band gap structures, J. Comput. Phys. 302 (2015) 393–404. https://doi.org/10.1016/j.jcp.2015.09.010.

[71] F. Meng, Y. Li, S. Li, H. Lin, B. Jia, X. Huang, Achieving Large Band Gaps in 2D Symmetric and Asymmetric Photonic Crystals, J. Light. Technol. 35 (2017) 1670–1676. https://doi.org/10.1109/JLT.2017.2667681.

[72] A. Takezawa, M. Kitamura, Phase field method to optimize dielectric devices for electromagnetic wave propagation, J. Comput. Phys. 257 (2014) 216–240. https://doi.org/10.1016/j.jcp.2013.09.051.

[73] O. Sigmund, K. Hougaard, Geometric Properties of Optimal Photonic Crystals, Phys. Rev. Lett. 100 (2008) 153904. https://doi.org/10.1103/PhysRevLett.100.153904.

[74] Y. Yan, P. Liu, X. Zhang, Y. Luo, Photonic crystal topological design for polarized and polarization-independent band gaps by gradient-free topology optimization, Opt. Express. 29 (2021) 24861–24883. https://doi.org/10.1364/OE.430079.

[75] H. Men, K.Y.K. Lee, R.M. Freund, J. Peraire, S.G. Johnson, Robust topology optimization of three-dimensional photonic-crystal band-gap structures, Opt. Express. 22 (2014) 22632–22648. https://doi.org/10.1364/OE.22.022632.

[76] F. Meng, B. Jia, X. Huang, Topology-Optimized 3D Photonic Structures with Maximal Omnidirectional Bandgaps, Adv. Theory Simulations. 1 (2018) 1800122. https://doi.org/10.1002/adts.201800122.

[77] K.E. Swartz, D.A. White, D.A. Tortorelli, K.A. James, Topology optimization of 3D photonic crystals with complete bandgaps, Opt. Express. 29 (2021) 22170–22191. https://doi.org/10.1364/OE.427702.

[78] A.R. Diaz, O. Sigmund, A topology optimization method for design of negative permeability metamaterials, Struct. Multidiscip. Optim. 41 (2010) 163–177. https://doi.org/10.1007/s00158-009-0416-y.

[79] S. Zhou, W. Li, Y. Chen, G. Sun, Q. Li, Topology optimization for negative permeability metamaterials using level-set algorithm, Acta Mater. 59 (2011) 2624–2636. https://doi.org/10.1016/j.actamat.2010.12.049.

[80] M. Otomori, T. Yamada, K. Izui, S. Nishiwaki, J. Andkjær, A topology optimization method based on the level set method for the design of negative permeability dielectric metamaterials, Comput. Methods Appl. Mech. Eng. 237–240 (2012) 192–211. https://doi.org/10.1016/j.cma.2012.04.022.

[81] S. Zhou, W. Li, G. Sun, Q. Li, A level-set procedure for the design of electromagnetic metamaterials, Opt. Express. 18 (2010) 6693–6702. https://doi.org/10.1364/OE.18.006693.

[82] W. Wang, W.K. Xu, H. Hai, An effective method for designing new structural left-handed material based on topology optimisation, Eur. Phys. J. Appl. Phys. 53 (2011). https://doi.org/10.1051/epjap/2010100140.

[83] S. Zhou, W. Li, Q. Li, Design of 3-D Periodic Metamaterials for Electromagnetic Properties, IEEE Trans. Microw. Theory Tech. 58 (2010) 910–916. https://doi.org/10.1109/TMTT.2010.2042845.

[84] X. Huang, Y.M. Xie, B. Jia, Q. Li, S.W. Zhou, Evolutionary topology optimization of periodic composites for extremal magnetic permeability and electrical permittivity, Struct. Multidiscip. Optim. 46 (2012) 385–398. https://doi.org/10.1007/s00158-012-0766-8.

[85] S. Nishi, T. Yamada, K. Izui, S. Nishiwaki, K. Terada, Isogeometric topology optimization of anisotropic metamaterials for controlling high-frequency electromagnetic wave, Int. J. Numer. Methods Eng. 121 (2020) 1218–1247. https://doi.org/10.1002/nme.6263.

[86] N. Murai, Y. Noguchi, K. Matsushima, T. Yamada, Multiscale topology optimization of electromagnetic metamaterials using a high-contrast homogenization method, Comput. Methods Appl. Mech. Eng. 403 (2023) 115728. https://doi.org/10.1016/j.cma.2022.115728.

[87] O. Sigmund, J.Sø. Jensen, Systematic design of phononic band-gap materials and structures by topology optimization, Philos. Trans. R. Soc. A Math. Phys. Eng. Sci. 361 (2003) 1001–1019. https://doi.org/10.1098/rsta.2003.1177.

[88] S. Halkjær, O. Sigmund, J.S. Jensen, Maximizing band gaps in plate structures, Struct. Multidiscip. Optim. 32 (2006) 263–275. https://doi.org/10.1007/s00158-006-0037-7.

[89] Y. fan Li, X. Huang, F. Meng, S. Zhou, Evolutionary topological design for

phonic band gap crystals, Struct. Multidiscip. Optim. 54 (2016) 595–617. https://doi.org/10.1007/s00158-016-1424-3.

[90] Y. Chen, X. Huang, G. Sun, X. Yan, G. Li, Maximizing spatial decay of evanescent waves in phononic crystals by topology optimization, Comput. Struct. 182 (2017) 430–447. https://doi.org/10.1016/j.compstruc.2017.01.001.

[91] H.W. Dong, X.X. Su, Y.S. Wang, C. Zhang, Topological optimization of two-dimensional phononic crystals based on the finite element method and genetic algorithm, Struct. Multidiscip. Optim. 50 (2014) 593–604. https://doi.org/10.1007/s00158-014-1070-6.

[92] H.W. Dong, X.X. Su, Y.S. Wang, Multi-objective optimization of two-dimensional porous phononic crystals, J. Phys. D. Appl. Phys. 47 (2014). https://doi.org/10.1088/0022-3727/47/15/155301.

[93] S. Hedayatrasa, K. Abhary, M.S. Uddin, J.K. Guest, Optimal design of tunable phononic bandgap plates under equibiaxial stretch, Smart Mater. Struct. 25 (2016) 0. https://doi.org/10.1088/0964-1726/25/5/055025.

[94] H.W. Dong, X.X. Su, Y.S. Wang, C. Zhang, Topology optimization of two-dimensional asymmetrical phononic crystals, Phys. Lett. Sect. A Gen. At. Solid State Phys. 378 (2014) 434–441. https://doi.org/10.1016/j.physleta.2013.12.003.

[95] H.-W. Dong, Y.-S. Wang, Y.-F. Wang, C. Zhang, Reducing symmetry in topology optimization of two-dimensional porous phononic crystals, AIP Adv. 5 (2015) 117149. https://doi.org/10.1063/1.4936640.

[96] H.-W. Dong, Y.-S. Wang, T.-X. Ma, X.-X. Su, Topology optimization of simultaneous photonic and phononic bandgaps and highly effective phoxonic cavity, J. Opt. Soc. Am. B. 31 (2014) 2946. https://doi.org/10.1364/josab.31.002946.

[97] Y. Luo, Y. Li, Tunable Bandgap Design of Soft Phononic Crystals Using Topology Optimization, Adv. Theory Simulations. 5 (2022) 2100620. https://doi.org/10.1002/adts.202100620.

[98] Y. Lu, Y. Yang, J.K. Guest, A. Srivastava, 3-D phononic crystals with ultra-wide band gaps, Sci. Rep. 7 (2017) 43407. https://doi.org/10.1038/srep43407.

[99] W. Li, F. Meng, Y. fan Li, X. Huang, Topological design of 3D phononic crystals for ultra-wide omnidirectional bandgaps, Struct. Multidiscip. Optim. 60 (2019) 2405–2415. https://doi.org/10.1007/s00158-019-02329-0.

[100] H. Gao, Y. Qu, G. Meng, Topology Optimization and Wave Propagation of Three-Dimensional Phononic Crystals, J. Vib. Acoust. 145 (2022). https://doi.org/10.1115/1.4054745.

[101] L. Lu, T. Yamamoto, M. Otomori, T. Yamada, K. Izui, S. Nishiwaki, Topology optimization of an acoustic metamaterial with negative bulk modulus using local resonance, Finite Elem. Anal. Des. 72 (2013) 1–12.

https://doi.org/10.1016/j.finel.2013.04.005.

[102] L. Lu, M. Otomori, T. Yamada, T. Yamamoto, K. Izui, S. Nishiwaki, Topology optimization of acoustic metamaterials with negative mass density using a level set-based method, Mech. Eng. J. 1 (2014) DSM0040–DSM0040. https://doi.org/10.1299/mej.2014dsm0040.

[103] T. Matsuki, T. Yamada, K. Izui, S. Nishiwaki, Topology optimization for locally resonant sonic materials, Appl. Phys. Lett. 104 (2014). https://doi.org/10.1063/1.4878259.

[104] Y. Noguchi, T. Yamada, K. Izui, S. Nishiwaki, Topology optimization for hyperbolic acoustic metamaterials using a high-frequency homogenization method, Comput. Methods Appl. Mech. Eng. 335 (2018) 419–471. https://doi.org/10.1016/j.cma.2018.02.031.

[105] H.W. Dong, S.D. Zhao, Y.S. Wang, C. Zhang, Topology optimization of anisotropic broadband double-negative elastic metamaterials, J. Mech. Phys. Solids. 105 (2017) 54–80. https://doi.org/10.1016/j.jmps.2017.04.009.

[106] S. Torquato, S. Hyun, A. Donev, Multifunctional Composites: Optimizing Microstructures for Simultaneous Transport of Heat and Electricity, Phys. Rev. Lett. 89 (2002) 266601. https://doi.org/10.1103/PhysRevLett.89.266601.

[107] S. Torquato, S. Hyun, A. Donev, Optimal design of manufacturable three-dimensional composites with multifunctional characteristics, J. Appl. Phys. 94 (2003) 5748–5755. https://doi.org/10.1063/1.1611631.

[108] S. Zhou, J. Cadman, Y. Chen, W. Li, Y.M. Xie, X. Huang, R. Appleyard, G. Sun, Q. Li, Design and fabrication of biphasic cellular materials with transport properties – A modified bidirectional evolutionary structural optimization procedure and MATLAB program, Int. J. Heat Mass Transf. 55 (2012) 8149–8162. https://doi.org/10.1016/j.ijheatmasstransfer.2012.08.028.

[109] S. Zhou, Q. Li, Computational design of multi-phase microstructural materials for extremal conductivity, Comput. Mater. Sci. 43 (2008) 549–564. https://doi.org/10.1016/j.commatsci.2007.12.021.

[110] A. Radman, X. Huang, Y.M. Xie, Topological design of microstructures of multi-phase materials for maximum stiffness or thermal conductivity, Comput. Mater. Sci. 91 (2014) 266–273. https://doi.org/10.1016/j.commatsci.2014.04.064.

[111] S. Zhou, Q. Li, Computational design of multi-phase microstructural materials for extremal conductivity, Comput. Mater. Sci. 43 (2008) 549–564. https://doi.org/10.1016/j.commatsci.2007.12.021.

[112] S. Torquato, A. Donev, Minimal surfaces and multifunctionality, Proc. R. Soc. London. Ser. A Math. Phys. Eng. Sci. 460 (2004) 1849–1856. https://doi.org/10.1098/rspa.2003.1269.

[113] S. Torquato, S. Hyun, A. Donev, Optimal design of manufacturable three-dimensional composites with multifunctional characteristics, J. Appl. Phys. 94 (2003) 5748–5755. https://doi.org/10.1063/1.1611631.

[114] N. de Kruijf, S. Zhou, Q. Li, Y.-W. Mai, Topological design of structures and composite materials with multiobjectives, Int. J. Solids Struct. 44 (2007) 7092–7109. https://doi.org/10.1016/j.ijsolstr.2007.03.028.

[115] V.J. Challis, A.P. Roberts, A.H. Wilkins, Design of three dimensional isotropic microstructures for maximized stiffness and conductivity, Int. J. Solids Struct. 45 (2008) 4130–4146. https://doi.org/10.1016/j.ijsolstr.2008.02.025.

[116] M.M. Neves, H. Rodrigues, J.M. Guedes, Optimal design of periodic linear elastic microstructures, Comput. Struct. 76 (2000) 421–429. https://doi.org/10.1016/S0045-7949(99)00172-8.

[117] T. Chatterjee, S. Chakraborty, S. Goswami, S. Adhikari, M.I. Friswell, Robust topological designs for extreme metamaterial micro-structures, Sci. Rep. 11 (2021) 15221. https://doi.org/10.1038/s41598-021-94520-x.

[118] L. Ai, X.-L. Gao, Topology optimization of 2-D mechanical metamaterials using a parametric level set method combined with a meshfree algorithm, Compos. Struct. 229 (2019) 111318. https://doi.org/10.1016/j.compstruct.2019.111318.

[119] X. Huang, A. Radman, Y.M. Xie, Topological design of microstructures of cellular materials for maximum bulk or shear modulus, Comput. Mater. Sci. 50 (2011) 1861–1870. https://doi.org/10.1016/j.commatsci.2011.01.030.

[120] A. Radman, X. Huang, Y.M. Xie, Topological optimization for the design of microstructures of isotropic cellular materials, Eng. Optim. 45 (2013) 1331–1348. https://doi.org/10.1080/0305215X.2012.737781.

[121] H.T. Kollmann, D.W. Abueidda, S. Koric, E. Guleryuz, N.A. Sobh, Deep learning for topology optimization of 2D metamaterials, Mater. Des. 196 (2020) 109098. https://doi.org/10.1016/j.matdes.2020.109098.

[122] J.K. Guest, J.H. Prévost, Optimizing multifunctional materials: Design of microstructures for maximized stiffness and fluid permeability, Int. J. Solids Struct. 43 (2006) 7028–7047. https://doi.org/10.1016/j.ijsolstr.2006.03.001.

[123] Y. Wang, Z. Luo, N. Zhang, Q. Qin, Topological shape optimization of multifunctional tissue engineering scaffolds with level set method, Struct. Multidiscip. Optim. 54 (2016) 333–347. https://doi.org/10.1007/s00158-016-1409-2.

[124] Y.M. Xie, X. Yang, J. Shen, X. Yan, A. Ghaedizadeh, J. Rong, X. Huang, S. Zhou, Designing orthotropic materials for negative or zero compressibility, Int. J. Solids Struct. 51 (2014) 4038–4051. https://doi.org/10.1016/j.ijsolstr.2014.07.024.

[125] X. Yang, Y.Y. Kim, Topology optimization for the design of perfect

mode-converting anisotropic elastic metamaterials, Compos. Struct. 201 (2018) 161–177. https://doi.org/10.1016/j.compstruct.2018.06.022.

[126] W. Chen, X. Huang, Topological design of 3D chiral metamaterials based on couple-stress homogenization, J. Mech. Phys. Solids. 131 (2019) 372–386. https://doi.org/10.1016/j.jmps.2019.07.014.

[127] Q. Zeng, S. Duan, Z. Zhao, P. Wang, H. Lei, Inverse Design of Energy-Absorbing Metamaterials by Topology Optimization, Adv. Sci. 10 (2023) 2204977. https://doi.org/10.1002/advs.202204977.

[128] G.W. Milton, A. V. Cherkaev, Which elasticity tensors are realizable?, J. Eng. Mater. Technol. Trans. ASME. 117 (1995) 483–493. https://doi.org/10.1115/1.2804743.

[129] G.W. Milton, M. Briane, J.R. Willis, On cloaking for elasticity and physical equations with a transformation invariant form, New J. Phys. 8 (2006) 248. https://doi.org/10.1088/1367-2630/8/10/248.

[130] M. Kadic, T. Bückmann, N. Stenger, M. Thiel, M. Wegener, On the practicability of pentamode mechanical metamaterials, Appl. Phys. Lett. 100 (2012) 191901. https://doi.org/10.1063/1.4709436.

[131] C. Cai, Z. Wang, Q. Li, Z. Xu, X. Tian, Pentamode metamaterials with asymmetric double-cone elements, J. Phys. D. Appl. Phys. 48 (2015) 175103. https://doi.org/10.1088/0022-3727/48/17/175103.

[132] Y. Huang, X. Lu, G. Liang, Z. Xu, Pentamodal property and acoustic band gaps of pentamode metamaterials with different cross-section shapes, Phys. Lett. Sect. A Gen. At. Solid State Phys. 380 (2016) 1334–1338. https://doi.org/10.1016/j.physleta.2016.01.041.

[133] A.N. Norris, Acoustic metafluids, J. Acoust. Soc. Am. 125 (2009) 839–849. https://doi.org/10.1121/1.3050288.

[134] R. Schittny, T. Bückmann, M. Kadic, M. Wegener, Elastic measurements on macroscopic three-dimensional pentamode metamaterials, Appl. Phys. Lett. 103 (2013) 231905. https://doi.org/10.1063/1.4838663.

[135] R. Hedayati, A.M. Leeflang, A.A. Zadpoor, Additively manufactured metallic pentamode meta-materials, Appl. Phys. Lett. 110 (2017) 91905. https://doi.org/10.1063/1.4977561.

[136] A.N. Norris, Acoustic cloaking theory, Proc. R. Soc. A Math. Phys. Eng. Sci. 464 (2008) 2411–2434. https://doi.org/10.1098/rspa.2008.0076.

[137] N.H. Gokhale, J.L. Cipolla, A.N. Norris, Special transformations for pentamode acoustic cloaking, J. Acoust. Soc. Am. 132 (2012) 2932–2941. https://doi.org/10.1121/1.4744938.

[138] C.N. Layman, C.J. Naify, T.P. Martin, D.C. Calvo, G.J. Orris, Highly anisotropic elements for acoustic pentamode applications, Phys. Rev. Lett. 111 (2013) 24302. https://doi.org/10.1103/PhysRevLett.111.024302.

[139] Y. Chen, X. Liu, G. Hu, Latticed pentamode acoustic cloak, Sci. Rep. 5 (2015) 15745. https://doi.org/10.1038/srep15745.

[140] Y. Guo, T. Dekorsy, M. Hettich, Topological guiding of elastic waves in phononic metamaterials based on 2D pentamode structures, Sci. Rep. 7 (2017) 18043. https://doi.org/10.1038/s41598-017-18394-8.

[141] Z. Sun, H. Jia, Y. Chen, Z. Wang, J. Yang, Design of an underwater acoustic bend by pentamode metafluid, J. Acoust. Soc. Am. 143 (2018) 1029–1034. https://doi.org/10.1121/1.5024351.

[142] A.O. Krushynska, P. Galich, F. Bosia, N.M. Pugno, S. Rudykh, Hybrid metamaterials combining pentamode lattices and phononic plates, Appl. Phys. Lett. 113 (2018) 201901. https://doi.org/10.1063/1.5052161.

[143] T. Bückmann, M. Thiel, M. Kadic, R. Schittny, M. Wegener, An elasto-mechanical unfeelability cloak made of pentamode metamaterials, Nat. Commun. 5 (2014) 4130. https://doi.org/10.1038/ncomms5130.

[144] L. Hai, Q. Zhao, Y. Meng, Unfeelable Mechanical Cloak Based on Proportional Parameter Transform in Bimode Structures, Adv. Funct. Mater. 28 (2018) 1801473. https://doi.org/10.1002/adfm.201801473.

[145] F. Fabbrocino, A. Amendola, G. Benzoni, F. Fraternali, Seismic application of pentamode lattices, Ing. Sismica. 33 (2016) 62–70.

[146] G.F. Méjica, A.D. Lantada, Comparative study of potential pentamodal metamaterials inspired by Bravais lattices, Smart Mater. Struct. 22 (2013) 115013. https://doi.org/10.1088/0964-1726/22/11/115013.

[147] B. Xu, Five kinds of micro-structures of pentamode metamaterials and their performance analysis, Dalian University of Technology, 2015.

[148] Q. Li, J.S. Vipperman, Three-dimensional pentamode acoustic metamaterials with hexagonal lattices, J. Acoust. Soc. Am. 145 (2019) 1372–1377. https://doi.org/10.1121/1.5093622.

[149] Y. Huang, X. Zhang, M. Kadic, G. Liang, Stiffer, stronger and centrosymmetrical class of pentamodal mechanical metamaterialss, Materials. 12 (2019) 3470. https://doi.org/10.3390/ma12213470.

[150] M. Kadic, T. Bückmann, R. Schittny, M. Wegener, On anisotropic versions of three-dimensional pentamode metamaterials, New J. Phys. 15 (2013) 23029. https://doi.org/10.1088/1367-2630/15/2/023029.

[151] G.W. Milton, M. Briane, D. Harutyunyan, On the possible effective elasticity

tensors of 2-dimensional and 3-dimensional printed materials, Math. Mech. Complex Syst. 5 (2017) 41–94. https://doi.org/10.2140/memocs.2017.5.41.

[152] J. Yvonnet, Computational Homogenization of Heterogeneous Materials with Finite Elements, 1st ed., Springer, Cham, 2019. https://doi.org/10.1007/978-3-030-18383-7.

[153] M. Ohsaki, N. Katoh, Topology optimization of trusses with stress and local constraints on nodal stability and member intersection, Struct. Multidiscip. Optim. 29 (2005) 190–197. https://doi.org/10.1007/s00158-004-0480-2.

[154] H. Cui, H. An, H. Huang, Truss topology optimization considering local buckling constraints and restrictions on intersection and overlap of bar members, Struct. Multidiscip. Optim. 58 (2018) 575–594. https://doi.org/10.1007/s00158-018-1910-x.

[155] F. Wang, O. Sigmund, J.S. Jensen, Design of materials with prescribed nonlinear properties, J. Mech. Phys. Solids. 69 (2014) 156–174. https://doi.org/10.1016/j.jmps.2014.05.003.

[156] P. Bourke, The shortest line between two lines in 3D, (1998). http://paulbourke.net/geometry/pointlineplane/.

[157] The MathWorks, Global Optimization Toolbox, (2019). https://www.mathworks.com/help/gads/.

[158] Y. Wang, O. Sigmund, Quasiperiodic mechanical metamaterials with extreme isotropic stiffness, Extrem. Mech. Lett. 34 (2020) 100596. https://doi.org/10.1016/j.eml.2019.100596.

[159] K. Bertoldi, P.M. Reis, S. Willshaw, T. Mullin, Negative Poisson's Ratio Behavior Induced by an Elastic Instability, Adv. Mater. 22 (2010) 361–366. https://doi.org/10.1002/adma.200901956.

[160] G.N. Greaves, A.L. Greer, R.S. Lakes, T. Rouxel, Poisson's ratio and modern materials, Nat. Mater. 10 (2011) 823–837. https://doi.org/10.1038/nmat3134.

[161] J. Dagdelen, J. Montoya, M. de Jong, K. Persson, Computational prediction of new auxetic materials, Nat. Commun. 8 (2017) 323. https://doi.org/10.1038/s41467-017-00399-6.

[162] X. Ren, R. Das, P. Tran, T. Ngo, Y. Xie, Auxetic metamaterials and structures: A review. Smart Mater. Struct. 27 (2018) 023001. https://doi.org/10.1088/1361-665X/aaa61c.

[163] W. Jiang, X. Ren, S.L. Wang, X.G. Zhang, X.Y. Zhang, C. Luo, Y.M. Xie, F. Scarpa, A. Alderson, K.E. Evans, Manufacturing, characteristics and applications of auxetic foams: A state-of-the-art review, Compos. Part B Eng. 235 (2022) 109733. https://doi.org/10.1016/j.compositesb.2022.109733.

[164] L. Wang, G. Ulliac, B. Wang, J.A. Iglesias Martínez, K.K. Dudek, V. Laude, M. Kadic, 3D Auxetic Metamaterials with Elastically-Stable Continuous Phase Transition, Adv. Sci. 9 (2022) 2204721. https://doi.org/10.1002/advs.202204721.

[165] A. Takezawa, K. Yonekura, Y. Koizumi, X. Zhang, M. Kitamura, Isotropic Ti-6Al-4V lattice via topology optimization and electron beam melting, Addi. Manuf. 22 (2018) 634-642. https://doi.org/10.1016/j.addma.2018.06.008.

[166] F. Kamarei, T. Goudarzi, A novel method for investigating the isotropy of response for randomly generated unit cells of particulate composites, Compos. Struct. 290 (2022) 115462. https://doi.org/10.1016/j.compstruct.2022.115462.

[167] R. Lakes, Foam Structures with a Negative Poisson's Ratio, Science. 235 (1987) 1038–1040. https://doi.org/10.1126/science.235.4792.1038.

[168] P.S. Theocaris, G.E. Stavroulakis, P.D. Panagiotopoulos, Negative Poisson's ratios in composites with star-shaped inclusions: a computational homogenization approach, Arch. Appl. Mech. 67 (1997) 274–286. https://doi.org/10.1007/s004190050117.

[169] M. Oster, M.A. Dias, T. de Wolff, M.E. Evans, Reentrant tensegrity: A three-periodic, chiral, tensegrity structure that is auxetic, Sci. Adv. 7 (2022) eabj6737. https://doi.org/10.1126/sciadv.abj6737.

[170] A. Farzaneh, N. Pawar, C.M. Portela, J.B. Hopkins, Sequential metamaterials with alternating Poisson's ratios, Nat. Commun. 13 (2022) 1041. https://doi.org/10.1038/s41467-022-28696-9.

[171] D. Prall, R.S. Lakes, Properties of a chiral honeycomb with a poisson's ratio of — 1, Int. J. Mech. Sci. 39 (1997) 305–314. https://doi.org/10.1016/S0020-7403(96)00025-2.

[172] J.N. Grima, R. Gatt, P.-S. Farrugia, On the properties of auxetic meta-tetrachiral structures, Phys. Status Solidi. 245 (2008) 511–520. https://doi.org/10.1002/pssb.200777704.

[173] J.N. Grima, K.E. Evans, Auxetic behavior from rotating squares, J. Mater. Sci. Lett. 19 (2000) 1563–1565. https://doi.org/10.1023/A:1006781224002.

[174] M. Taylor, L. Francesconi, M. Gerendás, A. Shanian, C. Carson, K. Bertoldi, Low Porosity Metallic Periodic Structures with Negative Poisson's Ratio, Adv. Mater. 26 (2014) 2365–2370. https://doi.org/10.1002/adma.201304464.

[175] B.M. Lempriere, Poisson's ratio in orthotropic materials, AIAA J. 6 (1968) 2226–2227. https://doi.org/10.2514/3.4974.

[176] T.C.T. Ting, T. Chen, Poisson's ratio for anisotropic elastic materials can have no bounds, Q. J. Mech. Appl. Math. 58 (2005) 73–82. https://doi.org/10.1093/qjmamj/hbh021.

[177] R. Almgren, An isotropic three-dimensional structure with Poisson's ratio =−1, J. Elast. 15 (1985) 427–430. https://doi.org/10.1007/BF00042531.

[178] G.W. Milton, Composite materials with poisson's ratios close to — 1, J. Mech. Phys. Solids. 40 (1992) 1105–1137. https://doi.org/10.1016/0022-5096(92)90063-8.

[179] G.W. Milton, Complete characterization of the macroscopic deformations of periodic unimode metamaterials of rigid bars and pivots, J. Mech. Phys. Solids. 61 (2013) 1543–1560. https://doi.org/10.1016/j.jmps.2012.08.011.

[180] K.K. Dudek, D. Attard, R. Caruana-Gauci, K.W. Wojciechowski, J.N. Grima, Unimode metamaterials exhibiting negative linear compressibility and negative thermal expansion, Smart Mater. Struct. 25 (2016) 25009. https://doi.org/10.1088/0964-1726/25/2/025009.

[181] T. Bückmann, R. Schittny, M. Thiel, M. Kadic, G.W. Milton, M. Wegener, On three-dimensional dilational elastic metamaterials, New J. Phys. 16 (2014) 33032. https://doi.org/10.1088/1367-2630/16/3/033032.

[182] Z. Lu, Q. Wang, X. Li, Z. Yang, Elastic properties of two novel auxetic 3D cellular structures, Int. J. Solids Struct. 124 (2017) 46–56. https://doi.org/10.1016/j.ijsolstr.2017.05.031.

[183] Q. Wang, Z. Li, Y. Zhang, S. Cui, Z. Yang, Z. Lu, Ultra-low density architectured metamaterial with superior mechanical properties and energy absorption capability, Compos. Part B Eng. 202 (2020) 108379. https://doi.org/10.1016/j.compositesb.2020.108379.

[184] D.R. Reid, N. Pashine, A.S. Bowen, S.R. Nagel, J.J. de Pablo, Ideal isotropic auxetic networks from random networks, Soft Matter. 15 (2019) 8084–8091. https://doi.org/10.1039/C9SM01241A.

[185] E. Andreassen, B.S. Lazarov, O. Sigmund, Design of manufacturable 3D extremal elastic microstructure, Mech. Mater. 69 (2014) 1–10. https://doi.org/10.1016/j.mechmat.2013.09.018.

[186] U.D. Larsen, O. Signund, S. Bouwsta, Design and fabrication of compliant micromechanisms and structures with negative Poisson's ratio, J. Microelectromechanical Syst. 6 (1997) 99–106. https://doi.org/10.1109/84.585787.

[187] A. Clausen, F. Wang, J.S. Jensen, O. Sigmund, J.A. Lewis, Topology Optimized Architectures with Programmable Poisson's Ratio over Large Deformations, Adv. Mater. 27 (2015) 5523–5527. https://doi.org/10.1002/adma.201502485.

[188] Y. Wang, Z. Luo, N. Zhang, Z. Kang, Topological shape optimization of microstructural metamaterials using a level set method, Comput. Mater. Sci. 87 (2014) 178–186. https://doi.org/10.1016/j.commatsci.2014.02.006.

[189] J. Wu, Z. Luo, H. Li, N. Zhang, Level-set topology optimization for mechanical metamaterials under hybrid uncertainties, Comput. Methods Appl. Mech. Eng. 319

(2017) 414–441. https://doi.org/10.1016/j.cma.2017.03.002.

[190] Y. Zheng, Y. Wang, X. Lu, Z. Liao, J. Qu, Evolutionary topology optimization for mechanical metamaterials with auxetic property, Int. J. Mech. Sci. 179 (2020) 105638. https://doi.org/10.1016/j.ijmecsci.2020.105638.

[191] M. Borovinšek, N. Novak, M. Vesenjak, Z. Ren, M. Ulbin, Designing 2D auxetic structures using multi-objective topology optimization, Mater. Sci. Eng. A. 795 (2020) 139914. https://doi.org/10.1016/j.msea.2020.139914.

[192] J. Gao, L. Wang, M. Xiao, L. Gao, P. Li, An isogeometric approach to topological optimization design of auxetic composites with tri-material micro-architectures, Compos. Struct. 271 (2021) 114163. https://doi.org/10.1016/j.compstruct.2021.114163.

[193] J. Gao, H. Xue, L. Gao, Z. Luo, Topology optimization for auxetic metamaterials based on isogeometric analysis, Comput. Methods Appl. Mech. Eng. 352 (2019) 211–236. https://doi.org/10.1016/j.cma.2019.04.021.

[194] C. Nguyen, X. Zhuang, L. Chamoin, X. Zhao, H. Nguyen-Xuan, T. Rabczuk, Three-dimensional topology optimization of auxetic metamaterial using isogeometric analysis and model order reduction, Comput. Methods Appl. Mech. Eng. 371 (2020) 113306. https://doi.org/10.1016/j.cma.2020.113306.

[195] Y. Zhou, H. Li, X. Li, L. Gao, Design of multiphase auxetic metamaterials by a parametric color level set method, Compos. Struct. 287 (2022) 115385. https://doi.org/10.1016/j.compstruct.2022.115385.

[196] A. Marmier, Z.A.D. Lethbridge, R.I. Walton, C.W. Smith, S.C. Parker, K.E. Evans, ElAM: A computer program for the analysis and representation of anisotropic elastic properties, Comput. Phys. Commun. 181 (2010) 2102–2115. https://doi.org/10.1016/j.cpc.2010.08.033.

[197] R. Gaillac, P. Pullumbi, F.-X. Coudert, ELATE: an open-source online application for analysis and visualization of elastic tensors, J. Phys. Condens. Matter. 28 (2016) 275201. https://doi.org/10.1088/0953-8984/28/27/275201.

[198] R. Hill, The Elastic Behaviour of a Crystalline Aggregate, Proc. Phys. Soc. Sect. A. 65 (1952) 349–354. https://doi.org/10.1088/0370-1298/65/5/307.

[199] L. J. Gibson and M. F. Ashby, Cellular Solids, 2nd ed. (Cambridge Press University, Cambridge, 1997), p. 292.

[200] J. Lehman, R. Lakes, Stiff, strong zero thermal expansion lattices via the Poisson effect, J. Mater. Res. 28 (2013) 2499–2508. https://doi.org/10.1557/jmr.2013.154.

[201] J. Lehman, R. Lakes, Stiff lattices with zero thermal expansion and enhanced stiffness via rib cross section optimization, Int. J. Mech. Mater. Des. 9 (2013) 213–225. https://doi.org/10.1007/s10999-012-9210-x.

[202] K. Svanberg, The method of moving asymptotes—a new method for structural optimization, Int. J. Numer. Methods Eng. 24 (1987) 359–373. https://doi.org/10.1002/nme.1620240207.

[203] D. Wang, L. Liu, G. Deng, C. Deng, Y. Bai, Y. Yang, W. Wu, J. Chen, Y. Liu, Y. Wang, X. Lin, C. Han, Recent progress on additive manufacturing of multi-material structures with laser powder bed fusion, Virtual Phys. Prototyp. 17 (2022) 329–365. https://doi.org/10.1080/17452759.2022.2028343.

[204] Y. Wen, B. Zhang, R.L. Narayan, P. Wang, X. Song, H. Zhao, U. Ramamurty, X. Qu, Laser powder bed fusion of compositionally graded CoCrMo-Inconel 718, Addit. Manuf. 40 (2021) 101926. https://doi.org/10.1016/j.addma.2021.101926.

[205] C. Wei, L. Li, X. Zhang, Y.-H. Chueh, 3D printing of multiple metallic materials via modified selective laser melting, CIRP Ann. 67 (2018) 245–248. https://doi.org/10.1016/j.cirp.2018.04.096.

[206] https://aerosint.com/

[207] S. Hasanov, S. Alkunte, M. Rajeshirke, A. Gupta, O. Huseynov, I. Fidan, F. Alifui-Segbaya, A. Rennie, Review on Additive Manufacturing of Multi-Material Parts: Progress and Challenges, J. Manuf. Mater. Process. . 6 (2022). https://doi.org/10.3390/jmmp6010004.

[208] J. Gao, Isogeometric topology optimization for auxetic metamaterials and structures, PhD Thesis, University of Technology Sydney, November 2019.

[209] T.A. Mary, J.S.O. Evans, T. Vogt, A.W. Sleight, Negative Thermal Expansion from 0.3 to 1050 Kelvin in ZrW2O8, Science (80-.). 272 (1996) 90–92. https://doi.org/10.1126/science.272.5258.90.

[210] M.P. Attfield, A.W. Sleight, Exceptional Negative Thermal Expansion in AlPO4-17, Chem. Mater. 10 (1998) 2013–2019. https://doi.org/10.1021/cm9801587.

[211] A.L. Goodwin, M. Calleja, M.J. Conterio, M.T. Dove, J.S.O. Evans, D.A. Keen, L. Peters, M.G. Tucker, Colossal Positive and Negative Thermal Expansion in the Framework Material Ag3[Co(CN)6], Science (80-.). 319 (2008) 794–797. https://doi.org/10.1126/science.1151442.

[212] A.W. Sleight, Negative thermal expansion materials, Curr. Opin. Solid State Mater. Sci. 3 (1998) 128–131. https://doi.org/10.1016/S1359-0286(98)80076-4.

[213] J. S. O. Evans, Negative thermal expansion materials †, J. Chem. Soc. Dalt. Trans. (1999) 3317–3326. https://doi.org/10.1039/A904297K.

[214] A. Kelly, L.N. McCartney, W.J. Clegg, R.J. Stearn, Controlling thermal expansion to obtain negative expansivity using laminated composites, Compos. Sci. Technol. 65 (2005) 47–59. https://doi.org/10.1016/j.compscitech.2004.06.003.

[215] G.D. Barrera, J.A.O. Bruno, T.H.K. Barron, N.L. Allan, Negative thermal expansion, J. Phys. Condens. Matter. 17 (2005) R217. https://doi.org/10.1088/0953-8984/17/4/R03.

[216] K. Takenaka, Negative thermal expansion materials: technological key for control of thermal expansion, Sci. Technol. Adv. Mater. 13 (2012) 13001. https://doi.org/10.1088/1468-6996/13/1/013001.

[217] R. Lakes, Cellular solid structures with unbounded thermal expansion, J. Mater. Sci. Lett. 15 (1996) 475–477. https://doi.org/10.1007/BF00275406.

[218] R. Lakes, Cellular solids with tunable positive or negative thermal expansion of unbounded magnitude, Appl. Phys. Lett. 90 (2007) 221905. https://doi.org/10.1063/1.2743951.

[219] X. Ni, X. Guo, J. Li, Y. Huang, Y. Zhang, J.A. Rogers, 2D Mechanical Metamaterials with Widely Tunable Unusual Modes of Thermal Expansion, Adv. Mater. 31 (2019) 1905405. https://doi.org/10.1002/adma.201905405.

[220] C.S. Ha, E. Hestekin, J. Li, M.E. Plesha, R.S. Lakes, Controllable thermal expansion of large magnitude in chiral negative Poisson's ratio lattices, Phys. Status Solidi. 252 (2015) 1431–1434. https://doi.org/10.1002/pssb.201552158.

[221] J. Qu, M. Kadic, A. Naber, M. Wegener, Micro-Structured Two-Component 3D Metamaterials with Negative Thermal-Expansion Coefficient from Positive Constituents, Sci. Rep. 7 (2017) 40643. https://doi.org/10.1038/srep40643.

[222] H. Yu, W. Wu, J. Zhang, J. Chen, H. Liao, D. Fang, Drastic tailorable thermal expansion chiral planar and cylindrical shell structures explored with finite element simulation, Compos. Struct. 210 (2019) 327–338. https://doi.org/10.1016/j.compstruct.2018.11.043.

[223] T.-C. Lim, Anisotropic and negative thermal expansion behavior in a cellular microstructure, J. Mater. Sci. 40 (2005) 3275–3277. https://doi.org/10.1007/s10853-005-2700-6.

[224] J. Aboudi, R. Gilat, Micromechanical analysis of lattice blocks, Int. J. Solids Struct. 42 (2005) 4372–4392. https://doi.org/10.1016/j.ijsolstr.2005.01.008.

[225] J.N. Grima, P.S. Farrugia, R. Gatt, V. Zammit, A system with adjustable positive or negative thermal expansion, Proc. R. Soc. A Math. Phys. Eng. Sci. 463 (2007) 1585–1596. https://doi.org/10.1098/rspa.2007.1841.

[226] C.A. Steeves, S.L. dos Santos e Lucato, M. He, E. Antinucci, J.W. Hutchinson, A.G. Evans, Concepts for structurally robust materials that combine low thermal expansion with high stiffness, J. Mech. Phys. Solids. 55 (2007) 1803–1822. https://doi.org/10.1016/j.jmps.2007.02.009.

[227] W. Miller, D.S. Mackenzie, C.W. Smith, K.E. Evans, A generalised scale-independent mechanism for tailoring of thermal expansivity: Positive and

negative, Mech. Mater. 40 (2008) 351–361. https://doi.org/10.1016/j.mechmat.2007.09.004.

[228] K. Wei, H. Chen, Y. Pei, D. Fang, Planar lattices with tailorable coefficient of thermal expansion and high stiffness based on dual-material triangle unit, J. Mech. Phys. Solids. 86 (2016) 173–191. https://doi.org/10.1016/j.jmps.2015.10.004.

[229] H. Xu, A. Farag, D. Pasini, Routes to program thermal expansion in three-dimensional lattice metamaterials built from tetrahedral building blocks, J. Mech. Phys. Solids. 117 (2018) 54–87. https://doi.org/10.1016/j.jmps.2018.04.012.

[230] J. Li, H.-T. Liu, Z.-Y. Zhang, Stiffness characteristics for bi-directional tunable thermal expansion metamaterial based on bi-material triangular unit, Int. J. Mech. Sci. 241 (2023) 107983. https://doi.org/10.1016/j.ijmecsci.2022.107983.

[231] J. Lehman, R. Lakes, Stiff, strong zero thermal expansion lattices via the Poisson effect, J. Mater. Res. 28 (2013) 2499–2508. https://doi.org/10.1557/jmr.2013.154.

[232] Q. Wang, J.A. Jackson, Q. Ge, J.B. Hopkins, C.M. Spadaccini, N.X. Fang, Lightweight Mechanical Metamaterials with Tunable Negative Thermal Expansion, Phys. Rev. Lett. 117 (2016) 175901. https://doi.org/10.1103/PhysRevLett.117.175901.

[233] L. Ai, X.-L. Gao, Three-dimensional metamaterials with a negative Poisson's ratio and a non-positive coefficient of thermal expansion, Int. J. Mech. Sci. 135 (2018) 101–113. https://doi.org/10.1016/j.ijmecsci.2017.10.042.

[234] K. Wei, Y. Peng, Z. Qu, Y. Pei, D. Fang, A cellular metastructure incorporating coupled negative thermal expansion and negative Poisson's ratio, Int. J. Solids Struct. 150 (2018) 255–267. https://doi.org/10.1016/j.ijsolstr.2018.06.018.

[235] X. Li, L. Gao, W. Zhou, Y. Wang, Y. Lu, Novel 2D metamaterials with negative Poisson's ratio and negative thermal expansion, Extrem. Mech. Lett. 30 (2019) 100498. https://doi.org/10.1016/j.eml.2019.100498.

[236] E.M. Parsons, Lightweight cellular metal composites with zero and tunable thermal expansion enabled by ultrasonic additive manufacturing: Modeling, manufacturing, and testing, Compos. Struct. 223 (2019) 110656. https://doi.org/10.1016/j.compstruct.2019.02.031.

[237] E. Boatti, N. Vasios, K. Bertoldi, Origami Metamaterials for Tunable Thermal Expansion, Adv. Mater. 29 (2017) 1700360. https://doi.org/10.1002/adma.201700360.

[238] X. Guo, X. Ni, J. Li, H. Zhang, F. Zhang, H. Yu, J. Wu, Y. Bai, H. Lei, Y. Huang, J.A. Rogers, Y. Zhang, Designing Mechanical Metamaterials with Kirigami-Inspired, Hierarchical Constructions for Giant Positive and Negative Thermal Expansion, Adv. Mater. 33 (2021) 2004919. https://doi.org/10.1002/adma.202004919.

[239] O. Sigmund, S. Torquato, Design of materials with extreme thermal expansion using a three-phase topology optimization method, J. Mech. Phys. Solids. 45 (1997) 1037–1067. https://doi.org/10.1016/S0022-5096(96)00114-7.

[240] A. Takezawa, M. Kobashi, M. Kitamura, Porous composite with negative thermal expansion obtained by photopolymer additive manufacturing, APL Mater. 3 (2015) 76103. https://doi.org/10.1063/1.4926759.

[241] A. Takezawa, M. Kobashi, Design methodology for porous composites with tunable thermal expansion produced by multi-material topology optimization and additive manufacturing, Compos. Part B Eng. 131 (2017) 21–29. https://doi.org/10.1016/j.compositesb.2017.07.054.

[242] Y. Wang, J. Gao, Z. Luo, T. Brown, N. Zhang, Level-set topology optimization for multimaterial and multifunctional mechanical metamaterials, Eng. Optim. 49 (2017) 22–42. https://doi.org/10.1080/0305215X.2016.1164853.

[243] Z. Han, X. Xiao, J. Chen, K. Wei, Z. Wang, X. Yang, D. Fang, Bifunctional Metamaterials Incorporating Unusual Geminations of Poisson's Ratio and Coefficient of Thermal Expansion, ACS Appl. Mater. Interfaces. 14 (2022) 50068–50078. https://doi.org/10.1021/acsami.2c11702.

[244] Y. Wang, L. Geng, Y. Lian, M. Xu, D. Fang, Three-dimensional assembled dual-material lattice with tailorable thermal expansion: Design method, modeling, and testing, Compos. Struct. 293 (2022) 115724. https://doi.org/10.1016/j.compstruct.2022.115724.